Development of a Robotic Positioning and Tracking System for a Research Laboratory

Thesis

Development of a Robotic Positioning and Tracking System for a Research Laboratory

A thesis submitted to the School of Engineering and Innovation for the Degree of ***Doctor of Philosophy***

The Open University

By

Stephen Obiajulu Nneji, B.Eng, M.Sc

February 2017

Abstract

Measurement of residual stress using neutron or synchrotron diffraction relies on the accurate alignment of the sample in relation to the gauge volume of the instrument. Automatic sample alignment can be achieved using kinematic models of the positioning system provided the relevant kinematic parameters are known, or can be determined, to a suitable accuracy.

The main problem addressed in this thesis is improving the repeatability and accuracy of the sample positioning for the strain scanning, through the use of techniques from robotic calibration theory to generate kinematic models of both off-the-shelf and custom-built positioning systems. The approach is illustrated using a positioning system in use on the ENGIN-X instrument at the UK's ISIS pulsed neutron source comprising a traditional XYZΩ table augmented with a triple axis manipulator. Accuracies better than 100microns were achieved for this compound system. Although discussed here in terms of sample positioning systems these methods are entirely applicable to other moving instrument components such as beam shaping jaws and detectors.

Several factors could lead to inaccurate positioning on a neutron or synchrotron diffractometer. It is therefore essential to validate the accuracy of positioning especially during experiments which require a high level of accuracy. In this thesis, a stereo camera system is developed to monitor the sample and other moving parts of the diffractometer. The camera metrology system is designed to measure the positions of retroreflective markers attached to any object that is being monitored. A fully automated camera calibration procedure is developed with an emphasis on accuracy. The potential accuracy of this system is demonstrated and problems that limit accuracy are discussed. It is anticipated that the camera system would be used to correct the positioning system when the error is minimal or notify the user of the error when it is significant.

Acknowledgements

I would like to render a few words of appreciations to the ones who made this project a success:
To Dr Jon James - Thanks a lot for all the guidance, insight, and encouragement which helped to push me in the right direction during the project. Thanks for taking time out of a busy schedule to read all my drafts.

To Dr Saurabh Kabra – Thanks for all the discussions and taking time out to answer my questions on neutron diffraction. Thanks for always lending a hand with my practical work and equipment acquisition.

To Dr Richard Moat - Thanks for all the practical advice always given with a touch of humour.

To Dr Shu Yan Zhang – Thanks for all the support and advice you offered at the start of the project.

To the Staff at ISIS – Joe, I appreciate all the brilliant suggestions and discussions. Genoveva and Winfried, thanks for the friendly discussions and always asking about my progress.

To Tony Millington and Adrian Hooper from the Survey Group at ISIS - Thanks for the support with the laser trackers used in this project.

To the people in the Electronics group at ISIS – Thanks for repairing the equipment necessary for the success of this project and for time invested in installing and debugging the Huber circle.

To Josef Lewis from the mechanical team at ISIS – Thanks for taking time out of your busy schedule to fabricate the pieces required for the camera system.

To Victor – Thanks for being a true friend, and always checking in to find out about my progress.

To all the Friends – who prayed for and encouraged me whilst this project was on-going. I truly appreciate you guys.

To my Family – For all the care, advice, and prayers which I can never fully repay, Thank you all.

To David Nneji – I am really grateful to you, for always supporting my dreams and encouraging me to be the best, thanks so much.

To God Almighty - who gave me life and wisdom to execute this project, I say a big Thank you.

Table of Contents

List of Figures

List of Tables

List of Abbreviations

ADM – Absolute Distance Measurement

AIFM – Absolute Interferometry

CAD – Computer-Aided Design

CCD – Charge-Coupled Device

CMM – Coordinate Measuring Machine

CPA – Circle Point Analysis

CT – Computerised Tomography

IDM – Incremental Distance Measurement

ILL – Institut Laue-Langevin

MRI – Magnetic Resonance Imaging

SMR – Spherically Mounted Retro-reflector

1 Introduction

Residual stresses are those stresses present in an object in the absence of any external load or force. Such stresses can be very detrimental to the performance of a material or the life of a component. Alternatively, beneficial residual stresses can be introduced deliberately [1]. Residual stresses can be introduced by many processes that materials are subjected to during assembly such as welding and bending. Neutron and synchrotron diffraction are non-destructive methods of determining residual stress from measurements of strain within crystalline or polycrystalline materials. Several dedicated instruments are available at synchrotron and neutron facilities worldwide for stress and strain scanning; with new instruments being commissioned on a regular basis. Using such methods a beam of neutrons or X-rays is directed at the sample and the diffracted particles are collected at a detector and used to compute the stresses. Data is collected throughout a small volume of the sample material known as the gauge volume, which is defined by the intersection of the incident and diffracted beams as shown in **Figure 1.1a**. One important aspect of making stress measurement using synchrotron or neutron diffraction is the accurate placement of the desired measurement points (which are inside the sample) into the gauge volume because stresses and strains in a sample are usually position and orientation dependent [2]. The main aim of this thesis is to improve the repeatability and accuracy of sample positioning as it applies to stress measurement, using robot calibration and sample monitoring which were applied to the ENGIN-X instrument described in the next Section. Some of the challenges of sample positioning for stress scanning are detailed in **Section 1.2**, and the motivation for this work is elaborated in **Section 1.3**.

1.1 ENGIN-X – Strain Scanning Neutron Diffractometer

ENGIN-X, which is situated at the ISIS neutron source near Oxford in the UK, is one of a number of instruments worldwide dedicated to measuring stress and strain in engineering components and other structures. The ENGIN-X instrument, on which this work is largely centred, was, in fact, the world's first neutron diffraction instrument designed and built specifically for making measurements of stress for industry [3]. Access to instruments like ENGIN-X is via a peer-review process, the users submit a proposal describing their experiment and the proposal is reviewed, successful applicant are awarded a few days of instrument access (or beam time) typically between 2 – 3 days. Due to the limited beam time, it is essential to optimise the experiment to ensure that the beam is maximised.

ENGIN-X consists of both static and mobile components enclosed in an experiment hutch. The neutron beam enters the instrument hutch through a set of 3 motorized slits known as Jaws. One of

the sets of jaws is fixed at 4m and one at 1.5m upstream of the sample position; the third set can be translated along a single axis towards or away from the sample to account for varying sample dimensions. The jaws are used to modify the horizontal and vertical size of the neutron beam. A pair of collimators are mounted in front of two neutron detectors centred at ±90 degrees to the incident neutron beam. These collimators, which comprise radially arranged neutron absorbing fins, ensure that only the neutrons diffracted from within the desired gauge volume arrive at the detectors; in fact the collimators define the size of gauge volume parallel to the beam. Each detector consists of a 2D array of scintillator detector elements which emit light on contact with a neutron particle [3]. The arrangement of these components is shown in **Figure 1.1**. A positioning table with X, Y, Z, Ω stages is provided to accurately place measurement points within the sample at the centre of the gauge volume. The measurement point needs to be placed with high accuracy in terms of position and orientation; desired accuracies around tens of microns [4] are not uncommon in stress scanning experiments. Sometimes it is necessary to manipulate the orientation of the sample in the beam in a more complex manner and a three axis robotic manipulator is available in such instances. For a more technical description of ENGIN-X, see [3].

The complexity of the shapes and sizes of the samples measured on ENGIN-X and similar instruments varies significantly between experiments. Positioning or aligning samples with simple geometry can be done using simple optical theodolites but as the complexity of the sample geometry increases there is a need for a better way to manipulate the sample. The challenges of positioning samples accurately were recognised from early experiments on the ENGIN instrument [5] (ENGIN was a fore-runner of ENGIN-X). The method of wall scanning was used whereby the position of the sample, in relation to the neutron beam, is established by passing the surface of the sample through the beam at various points and by mathematically fitting the resulting intensity curve to determine the position of the sample [6]. This was a time consuming and potentially error prone process which could unproductively consume a considerable proportion of the time allocated to an experiment. For this reason the ENGIN-X design proposal included development of a software component with the purpose of making this task easier, more accurate, and quicker. The SScanSS software [7] was the outcome of this endeavour. SScanSS was the first application of robotics principles to the simulation and control of general beam-line systems. SScanSS is now regularly used for the measurement of samples with a complex geometry in the areas of engineering and archaeological research [8]. The SScanSS approach belongs to a group of alignment techniques known as model based alignment in which models of the instrument are used to perform the sample alignment. An example of a SScanSS simulation can be seen in **Figure 1.2**.

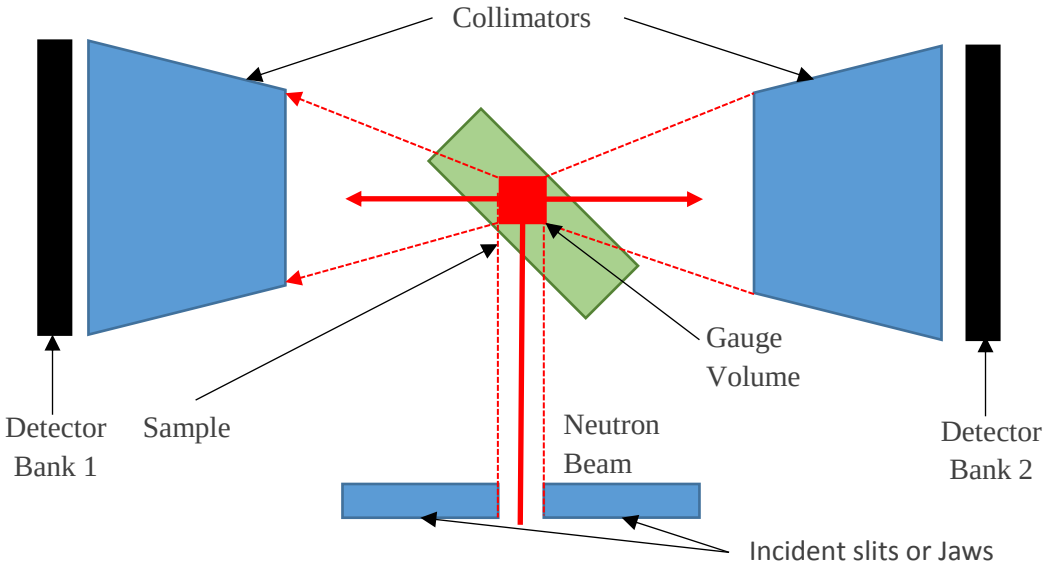

(a)

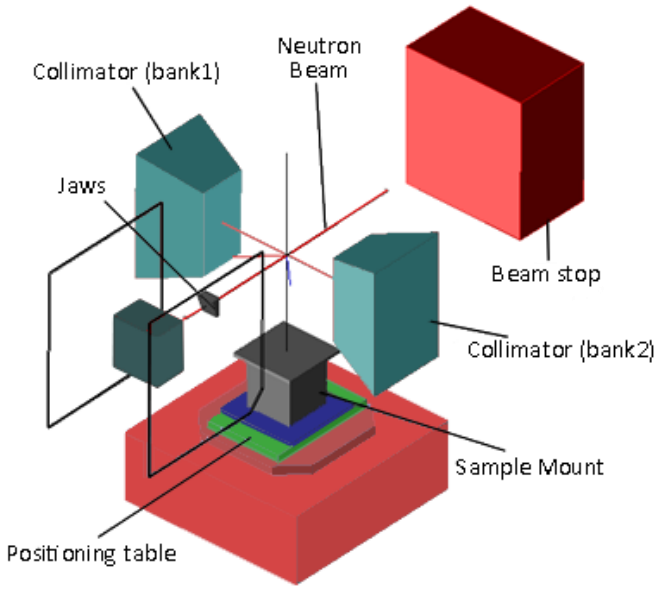

(b)

Figure 1.1: (**a**) Top view schematic diagram of the ENGIN-X instrument showing the gauge volume (**b**) A three-dimensional virtual model of the ENGIN-X instrument.

1.2 Challenges of Sample Alignment

The positioning of samples for stress scanning is a vital part of most experiments but this is not without its problems. Here are a few of the challenges that could arise when performing an experiment. It should be noted that although the challenges below are discussed within the ENGIN-X context, many similar instruments experience the same problems.

1. **Discrepancy between Simulated and Real motion**: The major output from any model based alignment software would be a set of motor positions which inform the positioning system where to move so as to place the measurement points in the gauge volume. The motor positions are computed offline using models of the sample and the instrument, which could have inadequate accuracy; therefore it is important to both minimise any sources of error through, for example better hardware modelling, but also to be able to determine if the sample or gauge volume has, in fact been accurately positioned before measurements commence.
2. **System Failure:** Failure of the positioning system could account for misalignment of the sample and could lead to wasted beam time if the misalignment is discovered or erroneous results if not discovered. For example, during a user cycle at ENGIN-X, it was reported by some users that the ENGIN-X positioning table would rotate the sample when not commanded to do so; such types of failures could slip by a non-observant user and end up as published results. It is therefore necessary to have a method to monitor sample 3D position and in some cases orientation in the absence of a user.
3. **Sample-Instrument Collisions:** Samples colliding with parts of the neutron instrument has always been a concern during sample alignment. With model based alignment, it is possible to check for collisions between the sample, positioning systems and the other instrument component like the collimator or jaws using the available models of these components. But in practice collisions could still be unhandled if models are not accurate enough or they are incomplete, for example, when a complex sample needs to be positioned a jig (example shown in **Figure 1.3**) must be assembled that would properly hold the sample. Each jig is different depending on the geometry of the sample. Typically the jigs are not included with the sample model as shown in **Figure 1.2**, hence these jigs are a potential source of collisions. This implies that collisions have to be checked manually before the experiment can proceed.

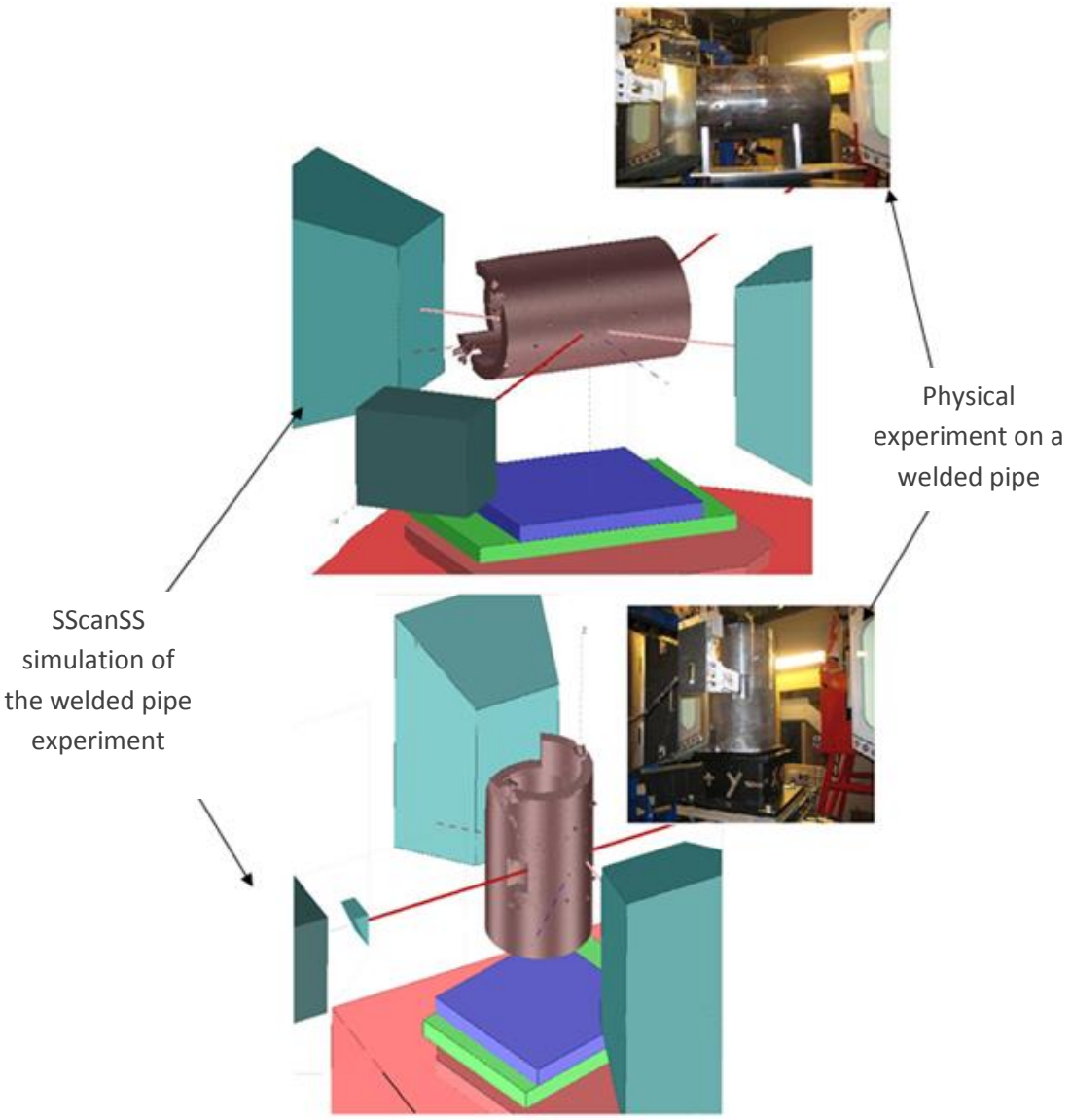

Figure 1.2: Experiment and corresponding SScanSS simulation, showing sample aligned in two different orientations for stress measurements.

4. **Human Error**: Simple experiments that do not require model based alignment still require the researcher to manually align the sample in the gauge volume, for example using a theodolite. Theodolites have been provided in the instrument hutch to check the sample alignment is correct but theodolites need to be handled manually. This could be error prone as motor position could be misread or wrongly recorded leading to wasted beam time. Also during manual alignments, no checks exist to stop the researcher from accidentally running the sample into a collimator or any other instrument part which could be a very costly accident.

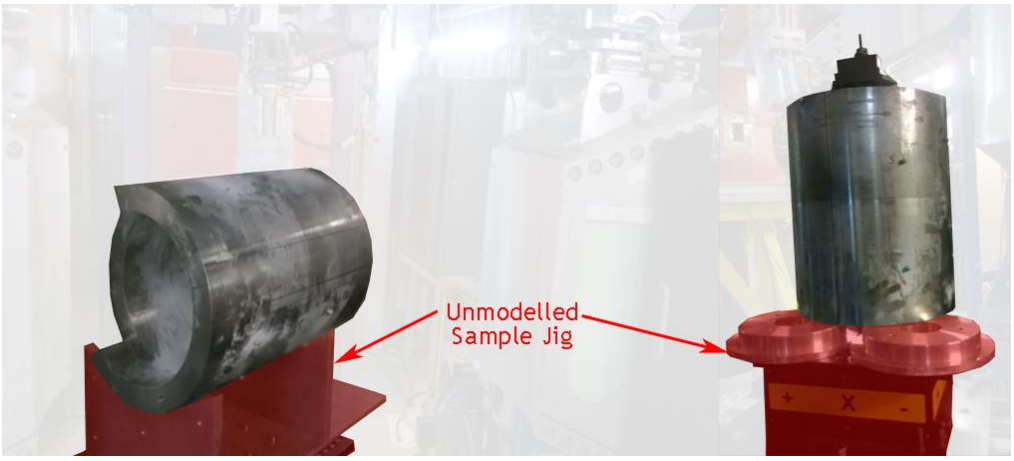

Figure 1.3: Examples of unmodelled Jigs used to hold a welded pipe during experiment.

1.3 Motivation

The aim of this work is to design, build, and assess a laboratory system for the simulation, control, and real time monitoring, of neutron and synchrotron diffraction experiments, as used for measuring strain in engineering components and samples. Although synchrotron X-rays and neutrons have different scattering characteristics, the control and monitoring of sample position and instrument hardware for synchrotron and neutron diffraction experiments are similar; therefore this project will focus on experiment control and monitoring in the case of neutron diffraction without any loss of generality. The project might be considered in two parts:

1. The first part explores the possible extension of model based alignment techniques, such that the simulation is built on accurate models of real, imperfect hardware rather than the currently assumed ideal hardware. This involves the design of a system for characterising and modelling real sample positioning systems, and other items of moving instrument hardware of varying design. The approach that has been taken for this part of the project is to explore the application of methods from the area of robot kinematics and calibration. The underlying requirement, in terms of sample positioning, is that the sample be positioned accurately in relation to the neutron beam. Framing the problem in terms of modelling and controlling hardware, as implied by the use of robotics methods, assumes that the relationship between the hardware and the neutron beam is well understood.

   The approach outlined above may be achievable in principle; however a vital question will be that of accuracy. The robotic methods to be employed are typically applied to the types of industrial robots used on, for example, manufacturing production lines. In such applications accuracy is likely to be measured in millimetres. In contrast accuracies of the order of 100 microns or better will be required if the methods are going to be useful for controlling neutron

diffraction instruments. This will require application of techniques, and the associated metrology hardware, at the limits of their expected accuracies, and will demand a comprehensive assessment and analysis of the achievable accuracy, under a range of relevant experimental conditions.

2. The second part of the project is to enable the progress of experiments to be continually monitored and errors to be reported or automatically corrected. This element of the project, which requires tracking numerous items of instrument hardware, to high accuracy, in an optically complex environment, will build on techniques from the area of computer vision. The work done in the project would potentially mitigate the first two challenges in **Section 1.2** and could address the other challenges with some extensions. The work done in this project is motivated by the following benefits.

1.3.1 Improved Accuracy in Experimental Planning

A major benefit of this work is the improvement of some of the practical aspects of setting up and executing diffraction measurements for strain determination. These practical aspects such as sample alignment are still considered too prominent in the experimental process; simulation software speeds up experimental planning significantly. This work contributes particularly to the accuracy of the models used for the experimental planning by ensuring that the virtual positioning system is as close as possible to the real world counterparts. The need for automation and simulation are also recognised by Wimpory and Boin [9] as a tool to increase throughput and maximize the productive use of beam time. They discussed the possibility of introduction of simulation into the instrument proposal submission and the use of smart positioning techniques all of which would not be possible or accurate enough if the instrument is incorrectly modelled.

1.3.2 Flexibility

There has been recently increased interest in exploring the use of industrial robotic arms as sample positioning systems [10, 11]. The motivation for the interest in robotic arms is the potential improvement in flexibility and the possibility of automation. For example, such systems may enable measurements in multiple orientations (see in **Figure 1.2**) be acquired without manual intervention; something which is not possible using traditional XYZΩ tables. The technique developed in this work allows the kinematic models of such robotic systems to be determined and included in the simulation software. Industrial robotic arms could even allow for sample changing so that many more samples which have been pre-scanned and attached to some holder can be placed near the instrument and picked up when necessary; this work could potentially allow such a system to be

designed. This work could also allow new types of measurement, such as mapping strain components in relation to complex internal or external surfaces, which are currently impractical.

1.3.3 Instrument and Sample Monitoring

The monitoring element of the project has benefits in two areas; from a practical point of view accuracy will be improved and problems such as sample-instrument collisions could be avoided, but equally importantly will be the expected benefits to quality assurance. Neutron diffraction methods are increasingly being used and relied upon by safety critical industries such as aerospace and nuclear power. The continual monitoring and checking of experiments will significantly increase confidence in the techniques as a whole. The data acquired form the monitoring systems could be used to create smart or self-learning simulations (for instance by genetic algorithms) that could constantly suggest ideas to improve the instrument [9].

1.4 Layout of the Dissertation

A literature review of the relevant work to this dissertation is presented in **Chapter 2,** which include reviews of diffraction as applied to stress scanning, robotic techniques for modelling positioning systems and 3D measurement systems.

Chapter 3 details the principles for modelling of the instrument positioning system or other moving hardware. A case study is presented of the ENGIN-X positioning system and the accuracy is tested using 3D measuring devices. **Chapter 4** presents the development of the sample/instrument monitoring system and the evaluation of the accuracy of the system

Chapter 5 presents practical demonstrations of the techniques developed. A texture experiment is presented to demonstrate the flexibility acquired from the technique. A complex stress scanning experiment is also presented to demonstrate the capabilities of the full system. **Chapter 6** concludes the work presented in this thesis and gives possible directions for future work.

2 Background

This chapter begins with a discussion of diffraction and sample alignment then presents a review of some of the relevant robotics terminology that will be used in the rest of the thesis. The chapter then proceeds to discuss the methodology through which robotic positioning systems could be modelled accurately for stress measurements. Subsequently a review of 3D measuring devices is presented since various scanning technologies will be employed for sample capture and/or sample tracking and in characterising hardware kinematics. It is likely that these technologies will be required to work at their limits of accuracy and a good understanding of available technologies and their advantages and limitations is required. Afterward laser tracking systems are discussed. Laser trackers will be vital for the calibration of positioning systems and correlating other elements of the real world laboratory to their virtual models and finally presented is a review of camera modelling and calibration which would be essential for the monitoring part of the project.

2.1 Diffraction

Neutron and X-ray diffraction are methods that are used for extracting the lattices parameters of a crystalline sample. Particles like neutrons and electrons exhibit both particle and wave like properties, this dual behaviour is described by the De Broglie equation below where p is the momentum of the particle, v is the particle speed, λ is the wavelength, m_n is the particle mass and h is Plank's constant.

$$p = m_n v = \frac{h}{\lambda} \qquad 2.1$$

When a beam of such particles with wavelength λ illuminates a crystalline sample, the scattering angle $2\theta_{hkl}$ of the beam is related to the d-spacing d_{hkl} of the diffracting lattice plane. This relationship is known as Bragg's law of diffraction which is given by **Equation 2.2** below and illustrated in **Figure 2.1**

$$\lambda = 2d_{hkl} \sin \theta_{hkl} \qquad 2.2$$

Constructive interference occurs when the difference in path length of the diffracted waves from adjacent planes is equal to the wavelength of the radiation. The constructive interference is typically seen as Bragg peaks in the diffraction spectrum. With knowledge of the wavelength of the radiation and the scattering angle, it is possible to compute the inter-planar spacing, i.e. the lattice spacing of the material.

The radiation used for stress measurement could be neutrons or X-rays. The choice of which to use would depend on the depth of the measurement and attenuation length of the radiation in the material and other instrument specific consideration. Irrespective of the radiation used for the

measurement, the method of extracting stain and stress from the lattice parameters remains the same.

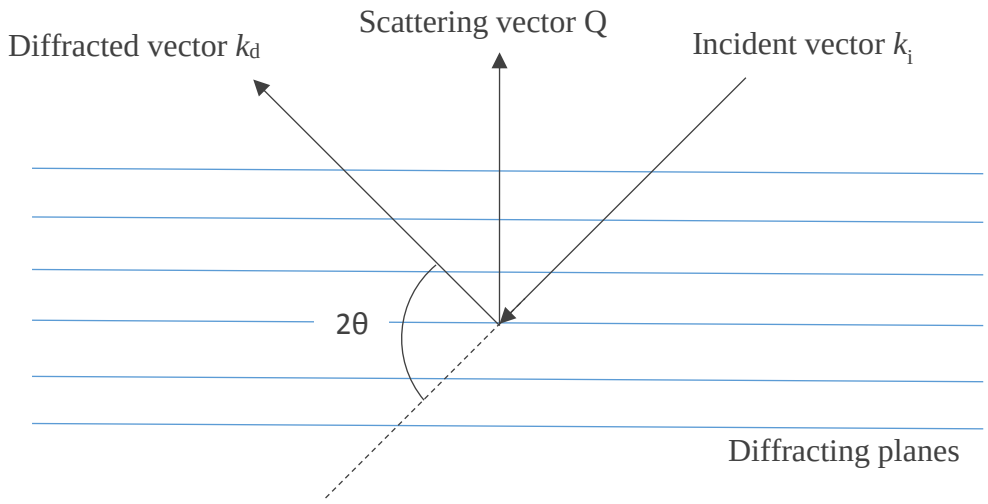

Figure 2.1: Illustration of Bragg scattering showing the incident beam diffracting off the lattice planes of a crystalline sample at 2θ angle.

2.1.1 Strain and Stress Determination

Strain is determined by measuring the change in the d-spacing of the crystalline sample. If the strain-free inter-planar spacing $d_{0,hkl}$ of the sample is known, the stain ε_{hkl} can be computed using **Equation 2.3** where the 'hkl'subscripts are the miller indices by which a particular crystal plane is identified.

$$\varepsilon_{hkl} = \frac{d_{hkl} - d_{0,hkl}}{d_{0,hkl}} = \frac{\Delta d_{hkl}}{d_{0,hkl}} \qquad 2.3$$

Strains and stresses are dependent on the position and orientation of the measurement volume in the sample [12]. As mentioned in **Chapter 1**, sample positioning is typically performed using XYZΩ tables, with additional hardware such as rotation tables or goniometers being added to meet particular requirements.

The stain ε_{ij} at a point in a material can be represented in the tensor notation as $\varepsilon_{ij} = \begin{pmatrix} \varepsilon_{11} & \varepsilon_{12} & \varepsilon_{13} \\ \varepsilon_{21} & \varepsilon_{22} & \varepsilon_{23} \\ \varepsilon_{31} & \varepsilon_{32} & \varepsilon_{33} \end{pmatrix}$ where the diagonal elements represent normal strains in the coordinate directions and the other elements are shear stains. The diagonal components of the strain tensor are known as the principal strain components. Six measurements are typically required to fully characterise the strain at a measurement point but knowledge of the principal strain components of the sample, allows full characterisation with only three measurements. Each of the three measurements is taken with the sample in a different orientation although an instrument could be

designed to measure several components at once[1]. If strains at the three principal directions have been measured, the stress σ_{ij} can be comptuted from the strain using **Equation 2.4** where E is the Young's modulus (modulus of elasticity), v is the Poisson's ratio.

$$\sigma_{ij} = \frac{E}{1+v}[\varepsilon_{ij} + \frac{v}{1-2v}(\varepsilon_{11} + \varepsilon_{22} + \varepsilon_{33})] \quad 2.4$$

The accuracy of residual stress measurement is dependent on the accuracy of alignment of several components of the instrument such as the jaws and the collimators, the accuracy of the peak fitting algorithm used to determine the diffraction peak position and, the amount of noise in the detected data. The following should be considered when determining the sample alignment accuracy required for an experiment:

- The size of the region on the sample in which stress is to be measured should be considered. The positioning should be accurate enough to avoid loss of spatial resolution in the strain maps.
- Stress measurements made near the surface of a sample require high positioning accuracy.
- Typically samples with larger strain gradients would require higher positioning accuracy.

A general rule of thumb within the field of engineering strain scanning is that the sample should be positioned to an accuracy that lies within 10% of the size of the gauge volume. Considering that gauge volumes on ENGINX are typically of the order of 1mm-4mm this indicates a positional uncertainty of 0.1-0.4mm. In the case of X-ray diffraction a typical gauge volume size could be as small as 0.1mm which indicates a positional uncertainty of 0.01mm. However, as indicated above certain measurements may require more accurate positioning than suggested by this rule. Systematic uncertainties in the measured strain are introduced when there is systematic error in the positioning [12].

2.2 Sample Alignment

Aligning an arbitrary sample with respect to the beam is a non-trivial matter and several methods have been proposed for sample alignment. Each of these methods have their associated shortcomings and benefits. A widely accepted method of aligning samples is a method known as wall scanning which can locate the sample using the beam. Another increasingly popular method is the model based alignment where some model of the sample (usually a 3D laser scanned model) is used to align the physical sample. There are also various methods of manual alignment where some measurement device is used to locate the physical sample on the instrument. The next sections discuss these methods in detail.

[1] The design of ENGIN-X allows two orthogonal components to be measured in one orientation therefore the principal components can be measured with the sample rotated to two orientations.

2.2.1 Wall Scanning

In this method, the sample surface is passed through the beam while the scattered intensity is recorded [6]. The position of the sample in relation to the beam is then determined from the intensity profile (see **Figure 2.2**). By repeating this process, using scans through different points on the sample surface, the sample alignment may be determined.

The major benefit of this method is that the sample is aligned with respect to the beam and it is the beam which is used to make measurement. Wall scanning is the only method with this advantage. Wall scanning is implicitly assumed to be the most accurate sample positioning method but this accuracy is dependent on a number of factor including: the geometry of the sample and the repeatability of the positioning table. For example, if the positioning table is repeatable to 100 microns the calculated sample position though found with higher accuracy can only be repeated to about 100 microns. It is popularly argued that wall scans could handle situations where the beam shifts but this would only be so if the beam shifted before alignment, if the beam shifted during the experiment then the wall scan would be as bad as every other method.

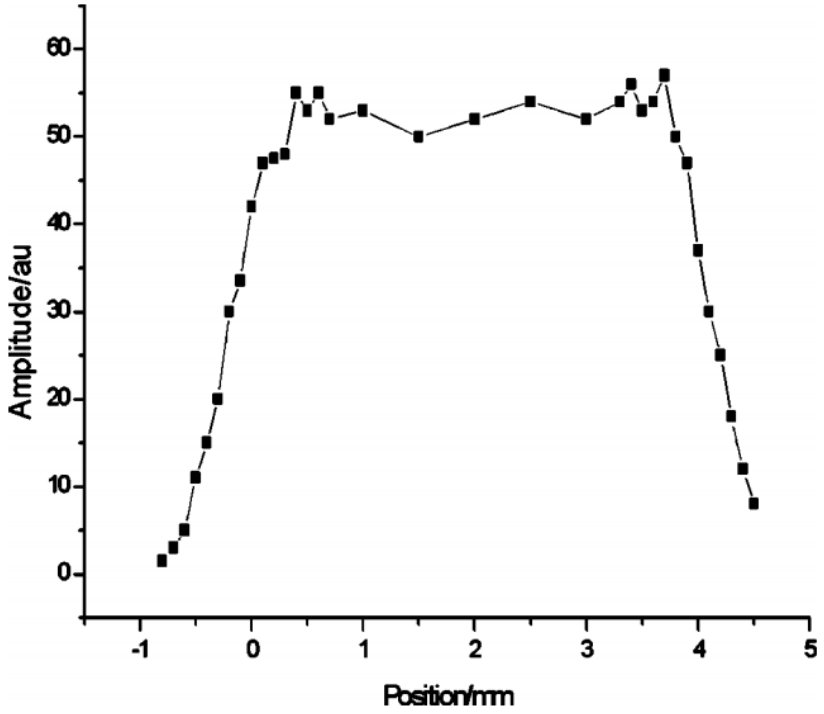

Figure 2.2: Typical wall scan for a relatively thin sample (4mm) [4].

This process of wall scanning can take significant time, particularly with a sample of complex geometry, thereby considerably reducing the time available for making scientifically useful measurements. The method can be affected by large grains (crystals with diameter greater than 50 microns), multiple scattering (when the radiation is diffracted multiple times before reaching the

detector), texture (crystals arranged in a non-random orientation) etc. in the sample. The effect of grain size on the result of a wall scan is illustrated in **Figure 2.3**. The typical assumptions made for a wall scans are that the sample geometry is known (e.g. flat plate, cylinder) and the composition of the material is uniform. These assumptions could fail for a large number of industrial samples.

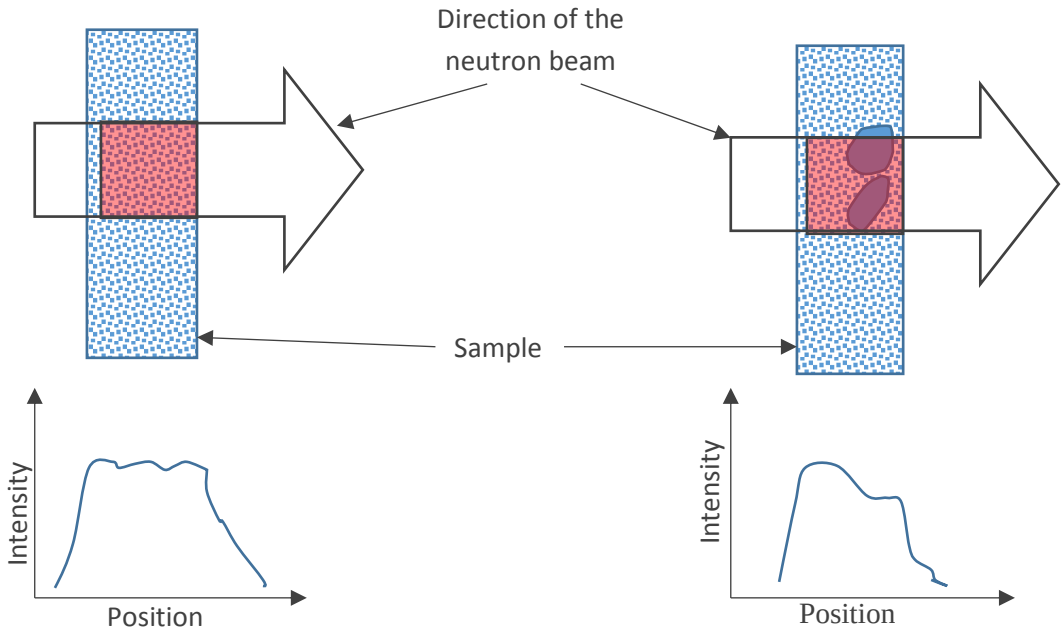

Figure 2.3: Illustration of the results of a wall scan on a sample with uniform grain size (Left) and a sample with large grains (Right). The position of the gauge volume in the sample is shown in red.

2.2.2 Manual Alignment

Manual alignment methods are used exclusively for simple samples. Such methods rely on the premise that an accurate and reliable physical means exist by which the centre of the gauge volume in space can be found. For example, a theodolite could find the centre of rotation of the theta stage and then the gauge volume is adjusted to lie in the same position. The adjustment of the gauge volume is carried out through pin scanning i.e. wall scanning a pin parallel to the beam and then adjusting the position of the collimators and then scanning perpendicular to the beam and adjusting the jaws. The theodolite would then serve as a physical means of locating the gauge volume if its position is kept stable. Manual alignment methods vary from one instrument to another but the common idea is to use a measuring device e.g. theodolites, cameras, lasers etc. to align certain parts of the sample and then used the aligned parts to compute the appropriate offsets for the measurement points. Certain assumptions are typically made about the shape of the sample when computing the measurement points such as assuming a perfectly flat surface or straight edge.

The measuring device used, for example, on ENGIN-X, is a theodolite. The theodolite is mounted at 45° to the beam axis of the instrument. The crosshairs of the theodolite have been pre-set to point to the centre of the gauge volume. As an example, aligning a cylindrical sample could be carried out using the following steps:

- Rotate the positioning table so that the axis of the X stage is perpendicular to the theodolite.
- Find the offsets that bring the each of the sample's edges to the centre of the gauge volume.
- Using those offsets, compute the location of the measurement point on the x axis.
- Repeat the previous steps for the Y stage to determine the (x, y) location of the measurement point.
- Finally the z component of the measurement point is determined by translated the Z stage until the measurement point is perfectly aligned in the crosshairs.

Manual alignment could be tedious and time consuming when multiple samples or a large number of measurement points are involved but has the advantage of simplicity as a result it is commonly used to aligned stain-free samples which have been cut into near perfect shapes and typically have a small number of measurement points.

2.2.3 Model based Alignment

These methods are also based on the premise that a physical means exists by which the centre of the gauge volume in space can be found. Using this physical means, a coordinate system for the instrument is created with the origin centred at the gauge volume and the x-axis would typically be aligned to direction of the beam. The concept of an instrument coordinate frame is essential to model based alignment. A typical model based alignment might consist of the following step:

- Construct a two or three dimensional sample model using, for example, laser scanning, computer aided design (CAD), probed surfaces or tomographic imaging.
- Identify the required measurement points in the sample model.
- If the models were made prior to when the sample was mounted on the instrument, the position and orientation of the sample with respect to the instrument must be determined. This could be done using special mounts that align into the instrument coordinate system and mounting the sample on them before constructing the sample model by, for example, scanning. Alternatively, fiducial markers could be added to the sample before scanning and the sample position on the instrument determined by measuring the position of these markers once the sample is mounted.
- Once the position of the sample model coincides with that of the real sample, it possible to calculate the positioner offset that bring each measurement point to the origin of the

instrument coordinate frame. The complexity and accuracy of such calculation would depend on the positioning system.

Several researchers have proposed model based alignment techniques. Ratel et al [4] proposed doing sample alignment with a modular sample holder, coordinate measurement machine (CMM) and a XYZΩ positioning table. Their sample was mounted on the positioner and digitized with the CMM. Digitizing the sample on the positioner avoids the use of fiducial markers. Measurement points were specified using the model acquired from the CMM and the coordinate frame of the CMM was set as the inverse of the axes of the positioning table, enabling motor positions to be generated by simply inverting the coordinates of the measurement point. The solution proposed by Ratel requires samples to be mounted on sample holders which are then used to align the coordinate systems on the instrument and the CMM. The use of such sample holders may not be convenient in the case of large or geometrically complex samples. The method also assumes that a standard XYZΩ positioning table will be used for sample alignment, which prohibits the use of more flexible positioning options. Altenkirch et al [10] proposed the use of a Stäubli RX90L robotic arm for sample positioning. They rely on the control unit supplied by the manufacturer for robot control but tested the accuracy of the robot using ISO standard testing procedures and found it to be sufficient. They scanned the sample along with the attached sample holder. The scanned samples were used to generate scripts that placed the specified measurement points in the gauge volume of the instrument. Their solution relies on the Stäubli control unit and therefore is not easily extendable to other neutron diffractometers using different positioning systems. A Stäubli RX160 six axis robot was previously installed on the STRESS-SPEC instrument at FRM II, but was deemed to be accurate enough only for texture measurements. This robot has recently been used for stress measurement [13] using a ring of six retro-reflective targets mounted on the robot. Measurements of at least three targets, with a laser tracker, are used to improve positioning accuracy. Ensuring that three reflectors are visible each time is acknowledged as an issue with this approach, which also relies on the manufacturer's control unit for controlling the robot. James et al [7] developed the Strain Scanning Simulation Software (SScanSS) which is currently used on ENGIN-X and at several other neutron facilities. SScanSS is based on a virtual laboratory and incorporates three dimensional models of the sample. SScanSS uses techniques from robot kinematics [14, 8] to model the positioning systems of the instruments as kinematic models. The use of kinematic models allows an arbitrary positioner or combination of positioners to be utilised on an instrument.

The attraction of model based alignment is the ability to quickly align samples with complex geometry. Alignment is based on sample geometry only so there are no problems caused by sample composition. Samples can be scanned in advanced thereby minimizing delay and maximizing the

beam usage. The disadvantage of this method is that the alignment is not done with respect to the beam so it is vulnerable to beam shifts. It could be determined if a beam shift has occurred by monitoring the position of the beam defining components like the jaws or collimator. Another disadvantage is that the alignment is only as good as the models of the sample and instrument. Discrepancy between instrument model and real instrument would lead to errors in alignment.

An important factor that has contributed to the rise of model-based alignment is the observation that many of the positioning systems used by neutron diffractometers can be classified as serial robots [14]. This has allowed a single software, such as SScanSS to be deployed at several facilities, thereby providing a common user interface. This observation is essential for the work done in this thesis therefore the next section introduces some robotic principles and how they can be used to model such positioning systems.

2.3 Robotics Terminology

A robotic positioning system (or manipulator) is composed of a set of links connected together by joints. The joints can either be very simple, such as revolute (rotational) or prismatic (sliding) joints, or they can be more complex, such as spherical or universal joints. The main purpose of a manipulator is to place a given tool (in the case of a neutron diffractometer, the tool is the sample) known as the end effector, at a desired position and/or orientation in a working environment. The reachable position of the end effector is limited by the following factors: number of joints, types of joints, link lengths, joint limits, and joint arrangement. The set of all reachable points in space is called the manipulator's workspace. There are three important properties of a manipulator in terms of the positioning of its end effector; these are accuracy, repeatability, and resolution. Accuracy is the difference between the manipulator's intended position and its actual position. For example, a combination of internal and external sensors might be used by the manipulator to determine its position, but these will only work with finite accuracy. Repeatability describes how much the position of the end effector deviates when it returns to a previously visited position. Resolution is the smallest change that can be measured by the manipulator's sensors, or caused by the actuators, whichever is larger. The achievable accuracy of a manipulator is limited by the repeatability while the achievable repeatability of the manipulator is limited by the resolution.

2.3.1 Serial and Parallel manipulators

Robotic manipulators can be classified into different groups based on the topological arrangement of the links that make up the manipulator. When the links are arranged in a closed loop chain the robot is called a parallel manipulator, a closed loop chain is obtained when a joint has three or more

links connected to it [15], see **Figure 2.4a**. A manipulator whose links are arranged in an open loop chain, having only two links attached to a joint (or one in the case of the base link and end effector) is known as a serial manipulator (**Figure 2.4b)**. A manipulator with both closed loop and open loop chains is called a hybrid manipulator. It should be noted that although not typical of serial manipulators in appearance the standard XYZΩ, sample positioning systems in use on most engineering diffractometers can be accurately classed as serial manipulators.

There are advantages and disadvantages with both sorts of robot. Parallel robots are theoretically more accurate than serial robot [16] but in practice accuracy would depend on good robot design. Parallel robots could provide more accuracy for large or heavy samples due to their better stiffness but typically less accuracies are required for larger samples so it should be determined if such accuracies are necessary. Serial robots, like industrial robotic arms, provide more dexterity than their parallel counterparts. For example, they could allow the measurement of the principal components of stress without manual intervention. Parallel robots typically have smaller workspaces than serial robots with similar size ratio due to the existence of singularities (configurations in which the manipulator is uncontrollable due to loss of one or more degrees of freedom) in the parallel robots. A summary of the advantages and difference of parallel and serial manipulators is presented in **Table 2.1**.

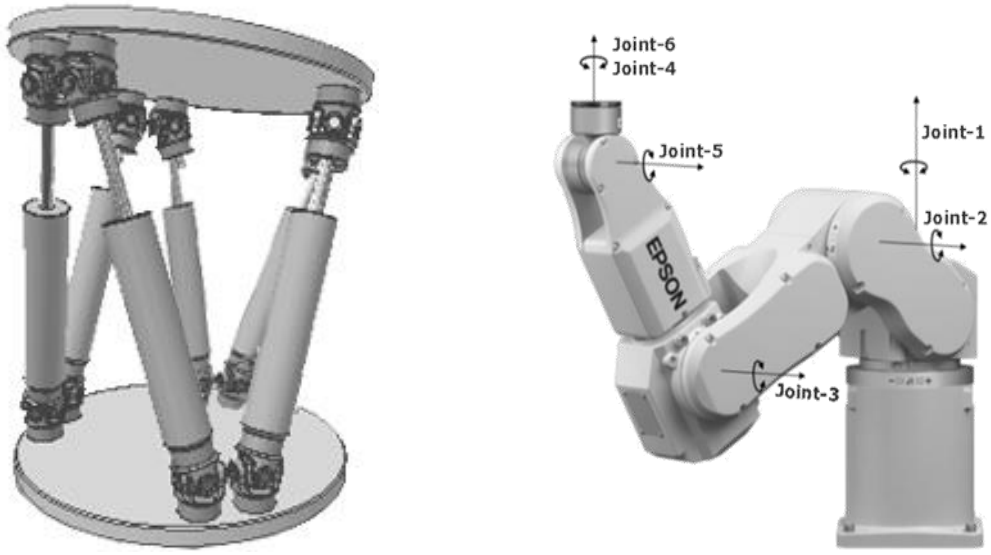

(a) **(b)**

Figure 2.4: Examples of parallel and serial manipulators **(a)** Stewart-Gough Platform or Hexapod [17] **(b)** Epson C4 Revolute manipulator [18].

As pointed out above, most positioning systems used by neutron diffractometers can be classified as serial robots; however one exemption is the SALSA engineering diffractometer located at the

Institute Laue–Langevin (ILL). This instrument uses a type of parallel robot known as a Stewart-Gough platform for sample positioning [19]), however this approach is very much in the minority, and for this reason the focus of this thesis is on serial robots.

2.3.2 Robot Kinematics

The motion (positon, velocity, and acceleration) of a manipulator can be studied under two branches of mechanics called kinematics and dynamics. Kinematics is the study of the motion of a body or a set of bodies (in this case links) without considering the forces causing the motion. Dynamics is the study of the motion of bodies, including the forces causing the motion and other properties of the bodies like mass and inertia. Most model-based alignment techniques proposed in the literature focus on kinematic modelling, due to its simplicity and the fact that it abstracts away information such as sample mass and positioner velocity. The assumption is made that the design of sample positioning systems, i.e. the stiffness of components and the general slow movement speeds, is such that dynamical issues are unimportant. Therefore this thesis is concerned largely with kinematic descriptions and will investigate dynamics when deemed necessary.

	Serial	**Parallel** [15]
Advantages	▪ Simpler Mechanism ▪ Large Workspace ▪ Less floor space required when compared to the parallel	▪ Higher accuracy ▪ Higher load ratio due to higher stiffness
Disadvantages	▪ Lower accuracy ▪ Errors are amplified along the chain	▪ More complex ▪ Limited workspace due to singularities

Table 2.1: Advantages and disadvantages of the serial and parallel manipulators

Forward Kinematics of Serial Manipulators

The forward kinematics of a manipulator is the computation of the position and orientation of the end effector given the joint variables. Assuming each joint has only a single degree of freedom the action of that joint can be described by a single real number which is called the joint variable; the joint variables are the joint angles in the case of a revolute joint or the link offset in the case of a prismatic joint. The forward kinematics of a serial manipulator is given by equation below

$$X = f(q) \tag{2.5}$$

where q is the configuration of the manipulator i.e. a vector of joint variables and X is the transformation that expresses the position and orientation of the end effector. A notation is required to describe the manipulator with respect to the joint variables; this notation will determine the mapping function in the equation above and also the representation of X. Although a number of notations have been proposed in the literature [20, 21], a commonly used notation [22, 23] is the Denavit-Hartenberg notation. For a serial manipulator having n joints and $n+1$ links (see **Figure 2.5**), the joints are labelled from 1 to n and links from 0 to n, so that joint i is connected to links $i-1$ and i. Each link has a coordinate frame assigned to it with the z axis in the direction of the axis of motion; this motion could be rotational in the case of a revolute joint or translational in the case of a prismatic joint. The x axis is placed along the common normal between the z axes of link i and $i-1$. If the z axes of link i and $i-1$ are intersecting, then the x axis is in the direction normal to the plane formed by the z axes. The y axis is selected using the right hand rule. The coordinate frame for link i is usually centred at joint $i+1$ or the centre of the end effector (in case of the last frame). The DH notation defines 4 parameters that are sufficient to describe the relationship between adjacent joints provided that the x_i axis is perpendicular to and also intersects with the z_{i-1} axis [24]. The DH parameters are defined below:

- The Joint angle θ_i, is the rotation around the axis z_i of joint $i+1$. It is variable if the joint is a revolute joint, otherwise it is constant.
- The Link twist α_i, is the rotation about the common normal between z_{i-1} and z_i.
- The Link length r_i, is the distance along the common normal between z_{i-1} and z_i.
- The displacement along the z_i axis is called the Link offset denoted as d_i. This distance is variable; if the joint i is a prismatic joint otherwise it is constant.

Using the DH parameters, a transformation matrix that relates the coordinate frame of link i to the coordinate frame of link $i-1$ is derived as.

$$^{i-1}A_i = Rot_z(\theta_i).Trans_z(d_i).Rot_x(\alpha_i).Trans_x(r_i) \tag{2.6}$$

$$= \begin{bmatrix} \cos\theta_i & -\sin\theta_i\cos\alpha_i & \sin\theta_i\sin\alpha_i & r_i\cos\theta_i \\ \sin\theta_i & \cos\theta_i\cos\alpha_i & -\cos\theta_i\sin\alpha_i & r_i\sin\theta_i \\ 0 & \sin\alpha_i & \cos\alpha_i & d_i \\ 0 & 0 & 0 & 1 \end{bmatrix} \tag{2.7}$$

The homogenous matrix $^{n-1}A_n$ (which combines the translation vector and rotation matrix into a single matrix [23]) would represent the transformation from the end effector link n to the link $n-1$. So to arrive at the transformation from the end effector frame (frame n) to the base frame (frame 0), all the transformation matrices are multiplied as shown below.

$$X = {}^{0}T_n = {}^{0}A_1 {}^{1}A_2 \dots {}^{n-1}A_n \quad 2.8$$

A number of variants to the Denavit-Hartenberg notation (hereafter called the DH notation) have been proposed [25]. One of the popular variants is also known as Craig's convention [20], this convention uses similar parameters to the standard DH notation; it differs in the way coordinate frames are assigned which results in a slightly different transformation matrix.

$$^{i-1}A_i = Rot_x(\alpha_i).Trans_x(r_i).Rot_z(\theta_i).Trans_z(d_i) \quad 2.9$$

$$= \begin{bmatrix} \cos\theta_i & -\sin\theta_i & 0 & r_{i-1} \\ \sin\theta_i \cos\alpha_{i-1} & \cos\theta_i \cos\alpha_{i-1} & -\sin\alpha_{i-1} & -d_i \sin\alpha_{i-1} \\ \sin\theta_i \sin\alpha_{i-1} & \cos\theta_i \sin\alpha_{i-1} & \cos\alpha_{i-1} & d_i \cos\alpha_{i-1} \\ 0 & 0 & 0 & 1 \end{bmatrix} \quad 2.10$$

This notation does not seem to provide a computational advantage over the standard version but has some notational advantages over the original according to the comparison in [25].

There are disadvantages associated with the DH notation. A 3D transformation has six degrees of freedom therefore six parameters are required to fully specify an arbitrary transformation; hence the DH notation cannot represent any arbitrary manipulator because it uses only four parameters. Also choosing arbitrary zero configurations (when all of the joint variables are zero) is not possible in the DH notation without the addition of constant joint offsets because the DH notation constrains the manner in which the coordinate frames of the links are assigned. This is undesirable because the default zero configuration could place the manipulator in an unnatural or unsafe posture. These disadvantages make it worth considering notations that avoid these challenges; one such notation is the Quaternion Modelling Convention. This notation uses a quaternion/vector pair as an alternative to the use of homogenous matrix. In [21], Funda et al show that this notation has certain advantages over the homogenous matrix based conventions in terms of computational efficiency and storage reduction - reducing numbers stored from 16 numbers (in a homogenous matrix) to 7 numbers (4 in a quaternion and 3 in a vector). This notation uses a single reference coordinate frame, which is typically assigned at the base of the manipulator. The other joints are represented with respect to this frame. A quaternion consists of a scalar and a vector as shown below.

$$q = \left(\cos\left(\frac{\theta}{2}\right), \ \sin\left(\frac{\theta}{2}\right)\langle k_x, k_y, k_z\rangle\right) \quad 2.11$$

The quaternion/vector pair for joint i is defined as $Q_i = [q_i, p_i]$ where p_i is a position vector $\langle p_x, p_y, p_z\rangle$ showing the position of joint $i+1$ relative to joint i and q_i is the quaternion representing the direction and angle of rotation of joint i. In this representation, the forward kinematics is derived by multiplying all the quaternion/vector pairs for all the joints.

$$Q_n = Q_1 Q_2 \dots \dots Q_{n-1} \quad 2.12$$

The multiplication of a quaternion/vector pairs is defined in **Equation 2.13**

$$Q_{i-1}Q_i = [q_{i-1}, p_{i-1}][q_i, p_i] = [q_{i-1} * q_i,\ \ q_{i-1} * p_i * q_{i-1}^{-1} + p_{i-1}] \quad 2.13$$

The asterisk symbols * represent quaternion multiplication. Q_n gives the position and orientation of the end effector in terms of the reference frame. A list of other notations that have been proposed can be seen in [26].

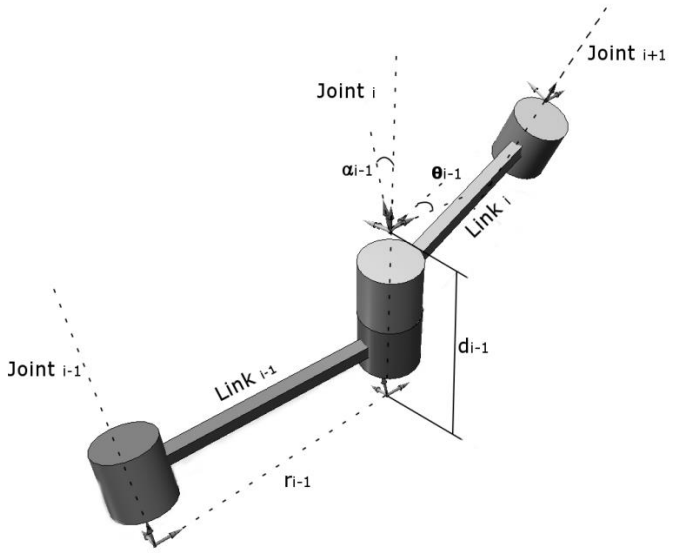

Figure 2.5: A simple two link system showing the standard DH parameters

Inverse Kinematics of Serial Manipulators

The inverse kinematics of a serial manipulator can be expressed as the reverse of the forward kinematic function. Given the desired end effector transformation X, the inverse kinematic function would be the function that returns the set of joint variables q required to achieve X.

$$q = f^{-1}(X) \quad 2.14$$

The solution to the inverse kinematic problem may not be unique; it is possible to have from one to an infinite number of arm configurations that coincide with the desired end effector position and orientation. It is also possible that a solution might not exist (if the desired position or orientation is unreachable). The inverse kinematics of a serial manipulator can be determined by analytical and/or numerical means.

Analytical Solution: The analytical solution is a closed-form solution and is the faster and more desirable method for applications that require quick computation of the inverse kinematics [27]. Joint angle constraints, number of joints, joint arrangement and other factors affect the number of

possible inverse kinematics solutions. The upper bounds on the number of inverse kinematic solutions for different types of manipulators are given in [27]. One manipulator type for which an analytical solution can be determined is a XYZΩ positioning table. The X, Y, Z stages of the positioning table would only change the position of the sample but not the orientation, this information allows the inverse kinematic problem to be separated into two problems: the inverse position and inverse orientation problems; this is known as kinematic decoupling [24]. If homogenous matrices are used to represent the transformation of the end effector; it will be in the form of **Equation 2.15**, where R is the rotation matrix and t is the translation vector.

$$H = \begin{bmatrix} R & t \\ 0 & 1 \end{bmatrix} \qquad 2.15$$

The translation vector is contributed to by all joints in a positioning table whereas the rotation matrix is only contributed to by the rotation stage. This allows the joint angle for the rotation stage to be solved first, and then the angle can be used to solve inverse kinematics of the remainder of the manipulator.

Numerical Solutions: These are approximations and they tend to be slower than the analytical solutions and will usually return only one of the possible solutions to the inverse problem. They attempt to move the end effector closer to the target point using iterative algorithms. Although analytical solutions are preferable to the numerical ones; the former is derived from the geometry of the robot therefore cannot be applied to another robot of a different geometry. This implies that analytical solutions cannot provide a general inverse kinematic solution for all types of robots which could be a problem when several manipulators are modelled. Also it becomes very difficult to get a closed form solution for manipulators with greater than 6 degrees of freedom, so a numerical solution or a mixed analytical and numerical scheme is usually used [28]. In [29], numerical methods that have been applied to the inverse kinematic problem were surveyed. These methods include the Jacobian Inverse methods (Jacobian Inverse, Pseudo-Inverse, Transpose), Newton methods, Heuristics (Cyclic Coordinate Descent, Triangulation) and others; the disadvantages and advantages of a number of these techniques were discussed.

As mentioned in **Chapter 1**, accurate knowledge of kinematic model parameters is necessary for high accuracy sample alignment, but these parameters are typically either unknown or inaccurately known. In the field of robotics, calibration techniques are used to determine the kinematic parameters of robotic manipulators.

2.3.3 Calibrating the Robotic Positioning System

Robot Calibration is the process of improving the accuracy of a robot by modifying its control software [30]. It is an attempt to determine a functional relationship between the joint sensors and

the actual pose of the manipulator, and hence to alter the robot positioning software to reflect this relationship [31]. The pose of a manipulator is defined as the orientation and position of the robot's end effector or tool. This is usually written as a vector of six parameters (3 translational and 3 orientation parameters) with orientation represented using Euler angles. Calibration could require the full pose of the robot (all six parameters) or a partial pose (less than six parameters).

$$X = [x \quad y \quad z \quad \theta_x \quad \theta_y \quad \theta_z \ ]^T \tag{2.16}$$

The main assumption in robot calibration is that the robot has good repeatability but low accuracy. This implies that whenever the robot is moved to a pose A, that the robot would actually be in a different pose B (low accuracy); but that every time the robot is moved to A, it always goes to B or within a reasonable distance to B (good repeatability). This assumption which is said to be true for industrial robots [30] means that improving the manipulator accuracy is analogous to finding the function that maps the pose B to the pose A. This function could then be used to correct the robot pose back to A.

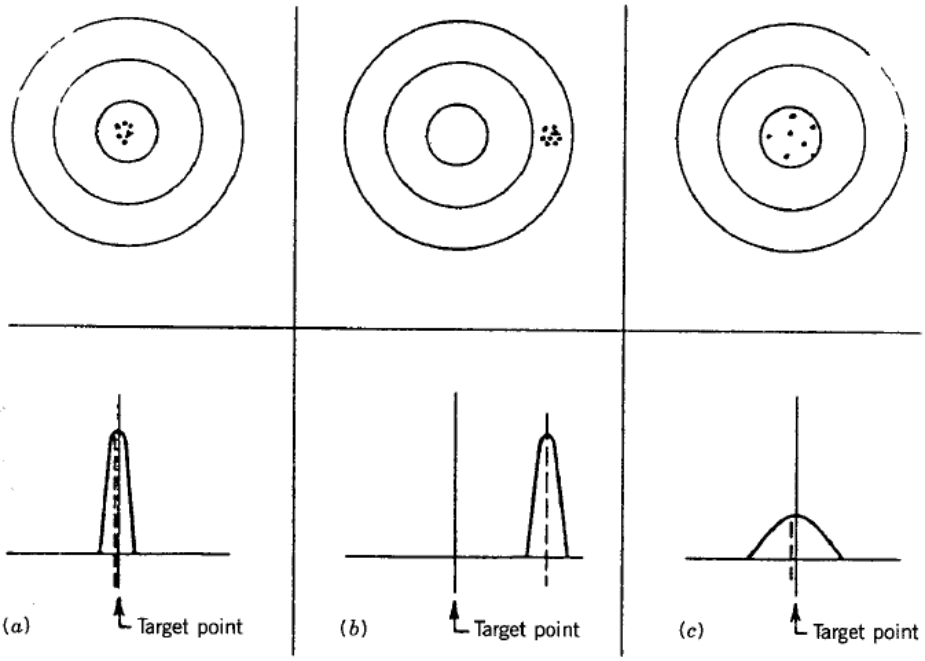

Figure 2.6: Illustration of Repeatability and Accuracy [30]. Column **(a)** shows a system with good accuracy and good repeatability, column **(b)** shows a system with poor accuracy and good repeatability, and column **(c)** shows a system with good accuracy and poor repeatability.

To further illustrate the concept of accuracy and repeatability as they relate to manipulators; consider a manipulator that is commanded to move to a random position and then moved to a target point. The actual position is then measured and this is repeated multiple times with a

different random starting point each time. **Figure 2.6** above illustrates three possible results from those measurements; it is possible that the measurements are

- close together and close to the target point,
- close together but far from the target point, and
- far from each other but close to the target point

These possibilities are illustrated in the upper row of **Figure 2.6**. The bottom row shows the same data as the upper row using a bell curve which shows the mean and standard deviation of the measured tool positions. The horizontal difference between the centre of the bell curve and the target point line can be interpreted as the accuracy of the manipulator where a smaller difference implies a higher accuracy while the spread of the bell curve gives the repeatability. The flatter the curve (or the larger the standard deviation), the lower the repeatability. With the aforementioned information, it can be seen that the first column (a) illustrates a manipulator with high repeatability and high accuracy. The second column (b) illustrates a manipulator with high repeatability and low accuracy. The last column (c) illustrates a manipulator with low repeatability and high accuracy. Real world robots would typically behave like manipulator b.

The accuracy that can be achieved from a calibrated manipulator depends on the manipulator's repeatability. Because repeatability error is normally distributed, the manipulator might achieve good accuracy in some instances but not in others. For this reason, a large number of measurements should be made to determine the repeatability of the manipulator before calibration, so that the limitation on the expected accuracy of calibrated manipulator is understood. A manipulator's repeatability is likely to vary depending on where in the workspace the measurement was made, the speed at which the tool is moving, the load on the end effector and the number of directions used for the repeatability test [32, 33]. Robot manufacturers typically specify a single value for repeatability which may therefore be misleading as the repeatability varies in the workspace. It would be best to attempt to determine the average and worst case repeatability of the manipulator [32].

Many factors may contribute to the low accuracy of a robotic manipulator, including construction inaccuracies, gear backlash, compliance (when joints or links flex under load), friction, and joint clearance (when joints wobble in-place). Some factors are irregular and not easily modelled which makes finding a mapping function that corrects for all factors a very difficult problem.

Roth et al [31] defined three levels of robot calibration; the levels are, in order of increasing complexity;

- **Joint level (Level-1) calibration**: At this stage, the aim is to determine the relationship between joint sensor signal and the actual motion. Level-1 calibration is typically done during construction of the robot and might be repeated if a joint is being replaced.

- **Kinematic (Level-2) calibration**: This is also known as geometric calibration. The assumption of Level-2 calibration is that differences exist between nominal kinematic parameters and actual kinematic parameters. Nominal kinematic parameters are the original parameters specified by the robot engineers, insufficient construction tolerances would lead to differences between the nominal and actual robot and consequently increase in the absolute position error. The goal of level-2 calibration is to improve accuracy of the kinematic model of the manipulator as well as the relationship between joint sensors and joint motion therefore level-2 calibration also comprises the level-1 calibration [31].
- **Non kinematic (Level-3) calibration**: This also known as non-geometric calibration. Non kinematic calibration is necessary if the robot is being controlled using a dynamic model rather than a kinematic model and also if the Level-2 calibration is deemed insufficient for the task [31]. Level-3 calibration aims to correct for factors such as friction, joint compliance or flexing, gear backlash. Modelling of these factors is non-trivial, requiring complex models [31].

2.4 Steps of Robotic Calibration

Calibration at any level would typically consist of four steps [31]

1. Modelling
2. Measurement
3. Identification of modelling parameters
4. Implementation

In this thesis, these steps are discussed for kinematic calibration only. The first step, modelling, is where a notation is chosen to represent the manipulator. In the second step, measurements of the manipulator's end effector position and orientation are taken. The third step is the determination of the actual, as opposed to the nominal kinematic parameters and in the final step; the identified kinematic parameters are implemented into the manipulator control software or the instrument's simulation software. In the next sections, each of these steps is discussed in more detail.

2.4.1 Modelling

Everett et al [34] proposed three criteria that should be met by any kinematic notation selected for calibration. The criteria are

- **Completeness**: The notation must have a sufficient number of parameters to represent the motion of the manipulator. In addition to being able to represent the uncalibrated manipulator, the notation should be able to represent any possible variation that could occur in the kinematic structure of the manipulator [35]. The number of independent parameters N that a complete model should have is given by the equation below

$$N = 4R + 2P + 6 \quad (2.17)$$

  Where R is the number of revolute joints and P is the number of prismatic joints in the manipulator. Revolute joints require a total of four constraints; two constraints to specify the orientation of the axis of rotation and another two constraints to position the joint on the axis of rotation. Prismatic joints require only two constraints which specify the axis of translation. Six constraints are needed to represent the tool coordinate frame arbitrarily with respect to the last joint frame.
- **Proportionality**: implies that small changes in the kinematic model should lead to small changes in the robot structure. Proportionality is essential because many researchers pose the calibration problem as an error minimization problem; hence the problem is ill conditioned if small changes in input lead to large changes in output.
- **Equivalence**: This is the ability to convert one model to another. Any two complete models should be equivalent, since both models have the same number of independent variables. Equivalence implies that one complete model cannot produce more accurate results than another complete model.

The DH notation [36], which is the most common kinematic representation when calibrating manipulators, fails the proportionality and completeness criteria. Hayati and Mirmirani [37] have shown that using the DH notation discontinuities (situations where small changes in DH parameters would lead to large changes in robot structure) exist at consecutive parallel or near parallel joint axes, if the joints are misaligned. Perfectly parallel consecutive joints as shown in **Figure 2.7** would have the following DH parameters $\alpha = 0,\ d = 0,\ \theta = 0,\ r = L.$

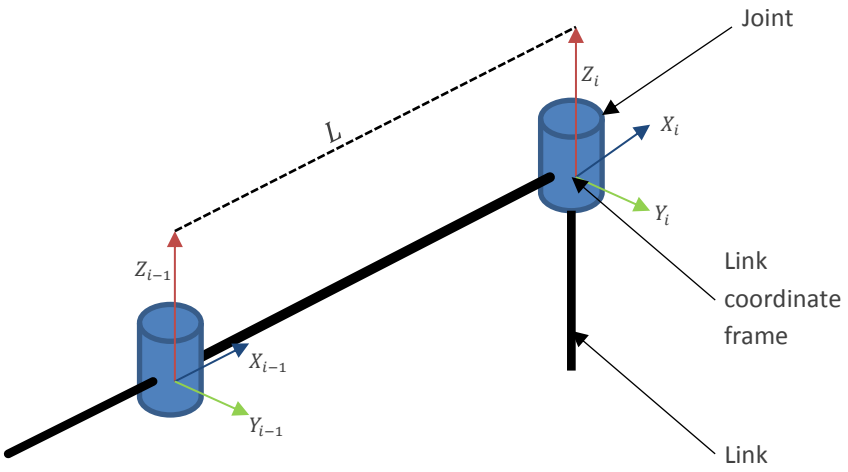

Figure 2.7: Schematic diagram showing the DH parameters of two perfectly parallel joints.

But when the axes are misaligned by a rotation about the y-axis, as shown in **Figure 2.8**, the z-axis of both joints would intersect at a distance f and the DH parameters become $\alpha = -\beta,\ d = -f,\ \theta = -90°,\ r = 0$. A small rotation in the y-axis leads to large changes in the DH parameters of the parallel joints, this simply shows that the DH notation is not proportional. This led Hayati and Mirmirani [37] to propose a modification to the DH notion, which replaced the joint offset parameter d_i of parallel joints with an angle parameter β_i. Hayati's modification rectifies the proportionality issue but not the completeness. Mooring et al [30] include constant joint offsets to each joint variable of the DH parameters hence making the model complete. Joint offsets are also used by Newman et al [38]. Hayati's modified DH notation has been used several times in the literature. Quaternion-vector pairs (see **Section 2.3.2**) [39], s-model [40], zero-reference model [30] have also been used as models in calibration literature. Some researchers used the four DH parameters and the Hayati angle making five parameters altogether [41, 42]. It should be noted that not all models proposed in literature achieve the three criteria previously stated and that although they publish their calibration results; these models would fail if they cannot represent the deviations in the actual manipulators. Everret and Hsu [35] show that the s-model proposed in [40] fails the completeness criteria.

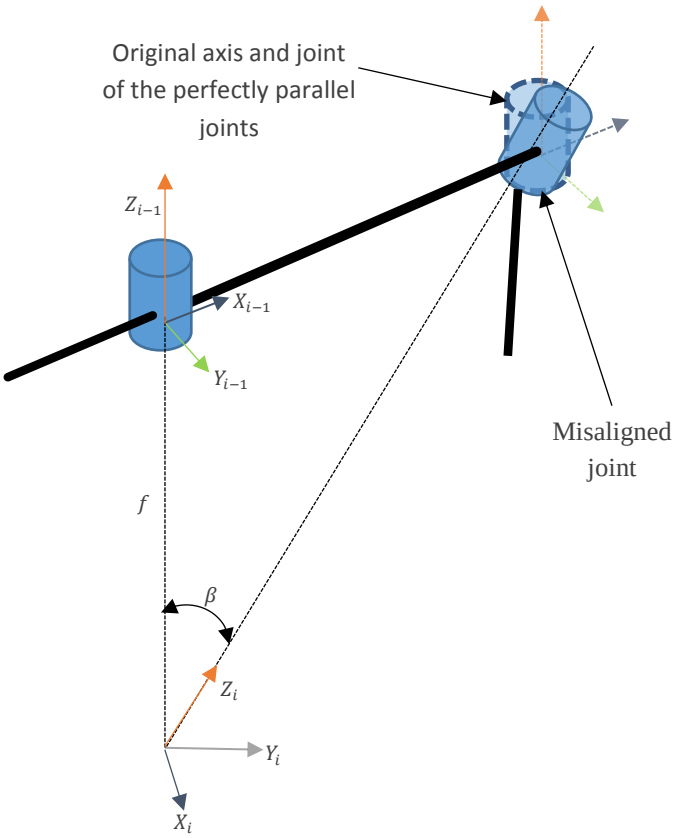

Figure 2.8: Schematic showing the DH parameters of two intended parallel axes, having one joint misaligned by β° around the Y-Axis.

2.4.2 Measurement

The measurement stage could vary depending on the method selected for kinematic parameter identification. The aim of the measurement stage is to acquire the actual end effector pose. The ultimate result from this stage would be a set of robot configurations and the measured poses. As previously stated it is possible to collect the full pose of the robot or a subset of the pose. The orientation part of the pose of the robot can be determined by measuring at least three non-collinear points on the end effector; the distances between the points should be known. Most measuring devices are incapable of covering the full workspace of the robot because they require line of sight to the target which might require the researcher to constrain the robot to a part of its workspace. A short survey of measurement strategies is provided below:

Chen and Chao [43] used three theodolites to triangulate the centre of a ball tip probe attached to the end link of the robot. The theodolites were operated manually but the data was read by a computer. Judd and Knasinski [44] used two theodolites to calibrate an Automatix AID-900

manipulator. They mentioned that the most time-consuming part of the experiment was the theodolite data collection. Driels and Pathre [45] developed an automatic theodolite for robot calibration which required no operator intervention. They used a camera, rotation stages, and computer vision algorithms to determine the line of sight to a spherical illuminated target. Švaco et al [46] used a stereo vision rig attached to the end effector of a KUKA Kr 6 R900 industrial robot. They used the stereo vision system to locate the centre points of calibration spheres placed at known positions and orientations, and then record the joint variables.

Mooring et al [30] used a coordinate measurement machine (CMM) to determine the end effector pose of a Puma 560. They attached a five tooling ball fixture shown in **Figure 2.9** to the end effector of the robot, and then moved the tool into a desired pose in the CMM's workspace. The desired pose is specified so that at least three balls on the tool are accessible to the CMM. The CMM is used to determine the centre of the balls by measuring a number of points on the surface of each ball. The end effector pose is computed using the measured centre points. This method is also time-consuming as the CMM was moved manually to the robot tool and the researcher must indicate what ball is to be measured beforehand, for every single pose.

Newman et al [38], use a laser tracker for their measurements. They manually rotate the target during the measurement so as to acquire the full angular range of the joint, but mention that manual reorientation could add further measurement error. Santolaria et al [41] also use a laser tracker but attempt to reduce measurement error by using an active target (this is a motorized target that automatically reorients itself to hold the laser tracker beam).

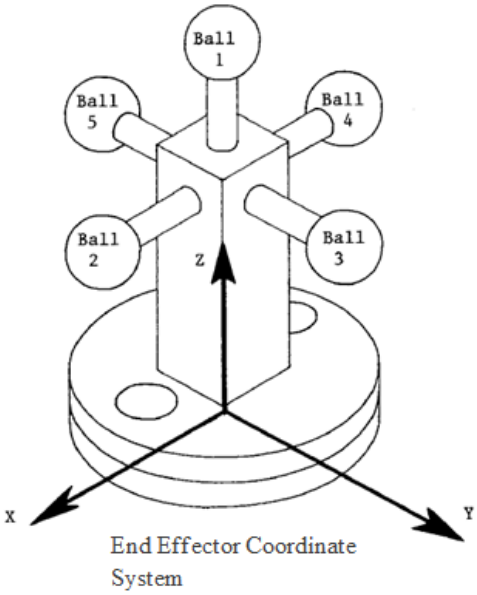

Figure 2.9: Five tooling ball fixture used by [30] to extract the full robot pose

A tri-axial accelerometer was used by Canepa et al [47] to measure the 3-axis acceleration of the end effector. Accelerometers have the advantage that they are less expensive that other 3D measuring devices like the CMM and not limited by line of sight issues but accelerometers tend to be affected by environmental noise and they output the acceleration of the end effector so the position data still needs to be estimated. Stone et al [40] used an ultrasonic range sensor to calibrate a Puma 560 robot.

Passive measurement schemes make use of a fixture to close the loop between the end effector and the base of the robot. The joint encoder readings from the new closed loop robot will provide enough information for calibration [48, 49]. The major challenge with this method is the cost and skill required to design the highly calibrated fixtures.

The selection of a measurement scheme for calibration is typically a trade-off between cost and desired accuracy [30], typically the more expensive measurement devices provide the higher accuracy. The structure of the robot being calibrated and also the ease of automating the taking of the measurements should also be considered when choosing a measurement scheme as automation may allow more measurements and hence better statistics.

2.4.3 Kinematic Parameter Identification

The goal of parameter identification is to estimate the model parameters of a robot A using measurements taken from robot A where robot A is the actual robot whose kinematic parameters deviate from those of the nominal robot, which would be denoted as robot B, for reasons previously explained. There are several approaches for estimating the model parameters of robot A, some approaches rely on the availability of the model parameters for robot B in addition to measurements from robot A while others directly estimate the parameters of robot A using measurements only. The approaches used to acquire the kinematic parameters of robot A can be classified into parametric and geometric methods.

Parametric Methods

These methods frame parameter identification as a minimization problem. Given a number of measurements within the workspace of a manipulator, these methods attempt to find the model parameters that reduce the error between the measured poses of robot A and the computed (predicted) poses of robot B. As with many minimization problems, convergence is not guaranteed and good accuracy depends on the initial guess of the kinematic parameters. The nominal kinematic parameters are typically used as the initial guess. In the measurement stage, sufficient measurements must be taken from the workspace of the actual robot or a desired subset of the

workspace. The poses to be measured should be selected so that there is significant variation in all the readings for each joint [43]. The selection of robot poses and the number of poses required for calibration is known as the observation strategy. Driels and Pathre [50], showed, using simulation, that the measurement noise and uncertainties will be transferred into the identified kinematic parameters, but that selection of an optimal observation strategy can minimize this effect. The selection of an optimal observation strategy is typically posed as a constrained optimization, or a search problem, with the objective of finding the set of poses that maximize an observation index. Several observation indices have been proposed that serve as a measure of goodness of a pose set [51].

In [52], parametric methods are broken up into open and closed loop methods. Open loop methods are methods that require an external measuring system to measure the pose of the manipulator whereas in closed loop methods, the manipulator is formed into a mobile closed loop chain. As discussed in **Section 2.4.2**, using the closed loop method the joint angle readings are sufficient to perform the calibration of the manipulator [49]. Although the closed loop methods do not require an external measuring device if the robot is unable to form a closed loop with itself due to insufficient degrees of freedom or the base being out of reach, a fixture must be added to complete the loop before joint readings can be taken, see **Figure 2.10**. Hollerbach and Wampler [52] explain that in open loop methods, the measuring system could be considered as a joint that closes the loop between the end effector and the base therefore the open loop methods could be considered as closed loop methods. In both open and closed loop methods, the parameters can be determined using a variety of numerical methods. In [30], Least squares, Kalman filters and other numerical methods are discussed with regard to how they can be applied to the parameter identification problem.

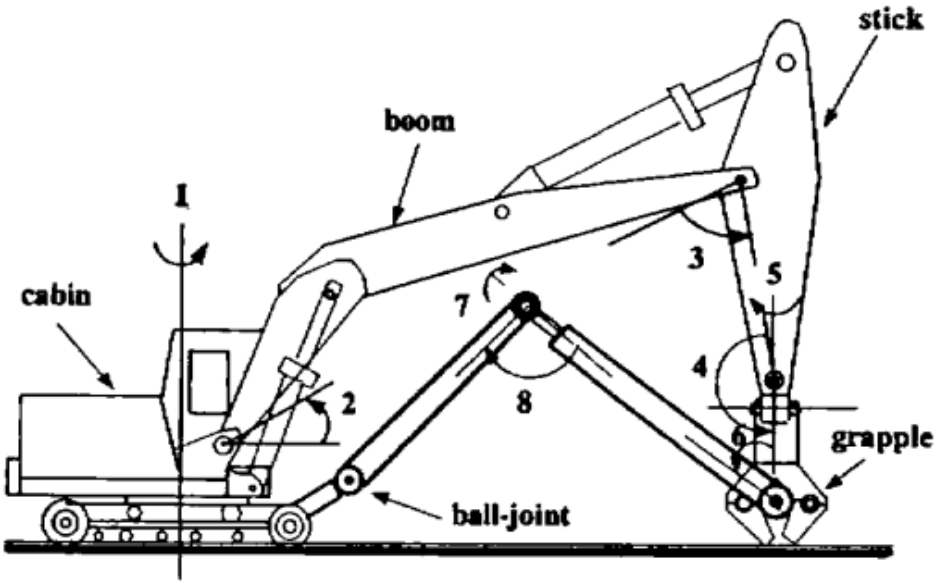

Figure 2.10: Closed loop calibration of an excavator. [52]

The assumption made in both open and closed loop parametric methods is that the nominal kinematic parameters are available and that they are close to the actual parameters [49].

Geometric methods: Circle Point Analysis

The other category of parameter identification techniques identified above are the geometric methods (or screw axis measurement methods). In these methods, the actual joint axes in the manipulator are identified and the kinematic parameters are analytically determined. The geometric methods include the Jacobian measurement method (discussed in the next section) and circle point analysis (CPA). These methods require no nominal model and can be used even when the positioning errors are relatively large. In CPA, all joints are kept stationary except one; points are measured from the path created by the motion of the single actuated joint. A revolute joint would create a circular path while a prismatic joint will plot a linear path. The CPA algorithm depends on the following being true of the manipulator:

- Rotating a revolute joint i will cause any attached rigid body to move in a circular path.
- The points p_{ij} measured along the circular path would lie on a plane t_i, where $j = 1,2,3, \dots, n$ for n different positions.
- The axis of rotation a_i is perpendicular to the plane t_i.
- The axis of rotation passes through the centre of the circular path formed by the joint motion.

The axis of rotation and the centre of rotation for each of the revolute joints form the identified joint axes for those joints. In the case of a prismatic joint, the measured points would have their principal

axis as the axis of translation and the mean of the points could be used as the centre of the joint. Other kinematic parameters can be extracted from the identified axes and joint centres.

In the measurement stage, it is essential that other joints are not moving so that they do not contribute noise to the measurements. It might be necessary to use joint stops or brakes, if the motion from the other joints is significant. The manipulator would typically be placed in the zero or initial position although the manipulator could be placed in any position that simplifies the measurements. After each measurement, the measured joint should be returned to its default position, before the next joint's path is measured. For a manipulator with N joints the measurements could be carried out as follows: The measurements could begin at joint 1, with joints $2,\ 3, \dots N$ kept at their default positions. The motion path for joint i is measured by placing a target point on link $i+1$ or on a tool attached firmly to the link or at the end effector. After measurement at joint i is done, the joint should be restored to the default position then proceed to joint $i+1$. This should be repeated until the last joint has been reached. It is also possible to begin at joint N and move to joint $N-1$, then $N-2$ until joint 1 is reached.

When measuring at joint i, the joint is moved sequentially to n different positions; these positions should be uniformly spaced to reduce the regression errors of the fitted model [30]. The joint positions can be calculated using **Equation 2.18**.

$$q_{ij} = q_{i,min} + (j-1)\Delta q,\ \ j = 1, 2, \dots, n \qquad 2.18$$

where $q_{i,min}$ is the smallest joint position and Δq is a constant joint offset. The offset Δq should be computed such that $q_{i,j}$ goes from $q_{i,min}$ to $q_{j,max}$, also taking into consideration the minimum resolution of every joint. A separate offset maybe required for prismatic and revolute joints.

It should be noted that CPA only determines the joint axes so extra measurements may be required to get the base transformation (transformation from the first joint to the base) and the transformation from the last joint to the tool. In a case where the 3D measurement systems is unable to cover the full path of any circular joint, it is recommended that at least half of the circle be measured [30]. After the measurement stage has been completed, the joint axes can be identified using the CPA algorithm. The CPA algorithm is as follows:

For each joint $\boldsymbol{i}$ *do the following:*

If the joint is revolute

Calculate the best-fit plane to the measured data using the method of least squares.

Project the measured points onto the determined plane.

Determine the normal to the best-fit plane.

Fit a circular arc to the measured data points and determine its centre.

If joint is prismatic

Fit a line to the measured data points

Find the centre of the joint. This is usually done by taking the mean of the points

Algorithm 2.1: Circle point analysis

After executing the CPA algorithm above, the output would be a set of best fit lines in the point-axis form. For revolute joints, the point is the centre of the rotation. For prismatic joints the point is the mean of the measured points. The next step is to extract the kinematic parameters from the identified joint axes. Several approaches have been proposed in the literature to extract kinematic parameter using the identified joint axes [40, 53].

Geometric methods: Jacobian Measurement Method

A moving body would have a linear velocity v and an angular velocity ω. For some applications, it is vital to determine the velocity for the joint actuators that would give a desired end effector linear and angular velocity. This is done using the manipulator Jacobian which is a $6 \times n$ matrix that linearly relates the joint velocities to the end effector velocities.

$$J = \begin{bmatrix} J_{v_1}, \dots, J_{v_n} \\ J_{\omega_1}, \dots, J_{\omega_n} \end{bmatrix} \quad 2.19$$

The Jacobian consists of two parts (**Equation 2.19**), the upper part J_{v_i} relates the velocity of joint i to the linear velocity of the end effector and the lower part J_{ω_i} relates the velocity of joint i to the angular velocity of the end effector. Both J_{v_i} and J_{ω_i} are 3 dimensional vectors that can be computed for each joint using **Equation 2.20** and **Equation 2.21** where z_{i-1} is the z axis of the $i-1^{th}$ coordinate frame, O_{i-1} is the origin of the $i-1^{th}$ coordinate frame, and O_n is the origin of the n^{th} coordinate frame. For derivation of the manipulator Jacobian the reader is directed to [24].

$$J_{v_i} = \begin{cases} z_{i-1} \times (O_n - O_{i-1}) & \text{for revolute joint } i \\ z_{i-1} & \text{for prismatic joint } i \end{cases} \quad 2.20$$

$$J_{\omega_i} = \begin{cases} z_{i-1} & \text{for revolute joint } i \\ 0 & \text{for prismatic joint } i \end{cases} \quad 2.21$$

The Jacobian measurement method was first proposed in [54]. The method relies on the estimation of the manipulator Jacobian via measurements. From the equations above, it can be seen that the Jacobian matrix contains the z-axes of all coordinate frames in the manipulator. Estimating the Jacobian is akin to measuring the z-axes of the joints in the manipulator and therefore similar methods used in CPA could be employed to determine the kinematic parameters. The Jacobian measurement method allows for flexibility in the measurement stage because the Jacobian matrix can be estimated using its relationship with joint velocities and end effector velocities or using the

joint torque to end effector force relationship. So the measurement stage could take one of these two approaches.

1. **Force and Torque approach:** In this approach, the manipulator needs a joint torque sensor for each joint and a 6-dof force/torque (also called wrench) sensor in the end effector. The effector is attached rigidly in the workspace in the selected measurement pose. A joint torque τ_i is applied via joint i and resulting end effector wrench w_i is measured. **Equation 2.22** shows the relationship between the end effector wrench and the torques of each joint.

$$\tau_i = J^T w_i + g \qquad 2.22$$

In the equation above, g is a vector of constant joint torques that is present in the measurements due to gravity, sensor biases, and friction/hysteresis. These constant joint torques are unknown but can be eliminated in the following ways:

- Select reference torques for each joint τ_i^o, then measure the reference wrench ω_i^o. **Equation 2.23** arises from the subtraction of the actual measurement torques and wrenches from the reference where $\Delta\tau = \tau_i - \tau_i^o$ and $\Delta w = \omega_i - \omega_i^o$. It is assumed that g is always constant irrespective of the reference [54].

$$\Delta\tau_i = J^T \Delta w \qquad 2.23$$

- Hollerbach et al [55], proposed that for each joint a positive torque τ_i, and a negative torque $-\tau_i$ should be applied and the corresponding wrenches measured. Subtracting the torques and the wrenches would lead to **Equation 2.24** and eliminate the constant torque.

$$2\tau_i = J^T \Delta w_i \qquad 2.24$$

Torques are measured one joint at a time for all the n joints in the manipulator. In **Equation 2.22**, τ_i is a $n \times 1$ column vector with all the entries set to zero except that value at i. The wrench w_i is a 6×1 column vector. Let $\boldsymbol{T} = (\tau_1, \dots, \tau_n)$ and $\boldsymbol{W} = (w_1, \dots, w_n)$, $\boldsymbol{T}$ would be a $n \times n$ matrix while $\boldsymbol{W}$ is a $6 \times n$ matrix. The Jacobian can then be extracted using **Equation 2.25**. If $\boldsymbol{W}$ is not invertible, the pseudoinverse should be used. Special consideration must also be given to redundant[2] manipulators ([55].

$$J = (\boldsymbol{T}\boldsymbol{W}^{-1})^T \qquad 2.25$$

[2] A redundant manipulator is any manipulator with more degrees of freedom than is necessary for the task, for example, when performing a 3 DOF task such as positioning an object on a plane, a manipulator with 4 DOF or more is considered redundant.

2. **Velocity based approach:** For this approach, sensors are required to simultaneously measure the end effector angular ω and linear velocity v and the joint velocities. Using the relationship in the equation below to estimate the manipulator Jacobian.

$$J\dot{\theta}_\iota = \begin{bmatrix} v_i \\ \omega_i \end{bmatrix} = t_i \qquad 2.26$$

The vector of effector velocities is also known as a twist. Similar to the previous approach, let $\boldsymbol{T} = (t_1, \dots, t_n)$ and $\dot{\boldsymbol{\Theta}} = (\dot{\theta}_1, \dots, \dot{\theta}_n)$, $\boldsymbol{T}$ would be a $6 \times n$ matrix while $\dot{\boldsymbol{\Theta}}$ is a $n \times n$ matrix.

$$J = \boldsymbol{T}\dot{\boldsymbol{\Theta}}^{-1} \qquad 2.27$$

Hollerbach et al [55] present the results of the force/torque Jacobian measurement method used to calibrate a Sarcos dexterous arm and compare the result with parametric and CPA methods. The Jacobian measurement method performed better than the CPA method although they mention that they used a very cheap measurement device for the CPA measurements.

The Jacobian measurement method is similar to CPA in that it only requires that a single joint be moved at a time. There are not many reports of the use of the Jacobian measurement method in the literature. This is probably due to the difficultly of accurately measuring the required joint torques or end effector velocities. In the literature, the method is applied on rotational joints only but could easily be apply to prismatic joints.

2.4.4 Implementation

The implementation stage (also known as compensation) is where the kinematic parameters determined via calibration are integrated into the manipulator's control software. The result of the preceding stage of calibration is the correction of the forward kinematics of the manipulator so that for each joint configuration the correct pose is returned. However robots are not usually controlled using forward kinematics alone, but using the inverse kinematics, therefore it is necessary to correct the inverse kinematics of the calibrated robot. Robots are designed so that the inverse kinematics can be easily solved. One design that simplifies the inverse kinematic problem is the inclusion of a spherical wrist; this allows the designer to separate the position and orientation inverse kinematic problems of a 6-DOF manipulator. Calibration could invalidate the original design and hence require that a new inverse kinematic solution be found. Several methods have been proposed that attempt to use the analytical solution of the uncalibrated manipulator to find the solution to the calibrated one [30, 31]. In addition to determining the correct inverse kinematics, if the manipulator is mobile with respect to its working environment, it may also be necessary to determine the position of the

base of the manipulator in relation to this environment; this calculation can also be included in the implementation stage.

Accurate measurement devices are essential to ensuring that virtual instrument models correspond to their physical counterparts. Therefore the next section of this chapter provides a review of 3D measurement or scanning techniques which will be useful, for this project.

2.5 3D Measuring Devices

A 3D scanner is a device that collects the 3D coordinates of a given region of an object or the whole object [56]. The region concerned could be a point, surface, or volume. A 3D scanner collects position data and in some instances colour information. 3D scanners will typically output a point or a set of points known as a point cloud. For some scanners the output is a set of slices (a slice is an image whose pixels represents the scan of a certain thickness or volume [57]).

Data output from a scanner can often be further processed; for example, it is possible to extract features from images and point clouds can be connected to form meshes, texture and colour may also be added. Some of these procedures may be done using on-board software in the scanner or in separate CAD software. It is important to clarify a few scanner related terms before proceeding:

- **Accuracy**: This is the difference between the scanned objects and the actual object. It can be computed by comparing known geometric features from the actual object like radius, height, or thickness with the same features from the scanned model.
- **Scan density**: This is the number of scanned points collected per unit area. The scan density is akin to the sampling rate in audio, i.e. the higher the sampling rate the closer the digital audio is to the original continuous signal. Likewise higher scan densities will lead to 3D models that are closer to the original objects assuming there is sufficient accuracy.
- **Resolution**: When discussing 3D scanners, the term “resolution” - may be used in a number of different ways. In some instances resolution is defined in a way similar to scan density, i.e. as the number of points per unit area, while in other cases it is defined as the smallest increment that the scanner can resolve or, in other words, the smallest possible distance between scanned points [58]. In this latter case the resolution of a scanner determines the minimum size of the features that can be reproduced by the scanner, for example, scanning a flat rectangular surface with a length of 0.2mm and width of 0.3mm would require that scanned points be less than 0.2mm apart so as to measure three or more points within the surface.

It should be noted that scanning an object is the same as measuring the position of points on that object, the exact position of the points on the object may or may not be known; therefore the words scanning and measuring could be used interchangeably.

2.5.1 Classification of 3D Measuring Devices

There are several criteria, under which 3D scanners can be classified; Várady, et al, [59] presents a hierarchical classification of scanning methods. Pavlidis, et al [60] categorize scanners based on the size of the object being scanned. Blais [61] gives a review of 20 years of range scanning technology. Sniderman [62] presents a classification based on the scan density of the scanners. In this thesis, scanners are discussed under the following criteria:

- usage proximity
- active/passive behaviour
- medium of interaction
- scan output
- principle of operation

Classification by Usage Proximity

The most common criterion used to classify scanners is the allowable distance between the scanner and the object been scanned. A scanner could therefore be categorized as contact or non-contact. The non-contact scanners can be further divided into short, mid and long range scanners. Contact scanners are scanners that need to be touching the desired point on the object's surface before returning the position coordinate of the point. A popular example of a contact scanner is a coordinate measuring machine (CMM). A CMM is typically a Cartesian robot (similar to a positioning table) but more recently articulated robot arms have also been used to create more portable CMMs (see **Figure 2.11**). Typically a CMM has a touch probe that determines when the CMM is touching an object, the position coordinate of the touched point can be acquired by reading the joint variables of the CMM and computing the forward kinematics of the robot. It can also be argued that a scanner such as a laser tracker (a laser tracker is a device that uses a laser to track the position of a target in free space) can also be classified as a contact scanner because the user of the tracker must place a target on the object being measured making it impossible to measure the coordinates of points that cannot be reached by the user (Laser Trackers will be discussed more fully in **Section 2.5.2**).

Non-contact scanners typically emit some type of energy that interacts with the object to be measured so that they can then extract the position information from the reflected energy. The range of a non-contact scanner can be affected by a number of factors which will be specific to the characteristics of the energy being emitted and detected.

Figure 2.11: Traditional Gantry CMM [63] (Left). Articulated robot arm CMM [64] (Right)

One problem with contact scanners is that the size of the touch probe determines the size of the feature that can be measured; also the degrees of freedom of the CMM will limit its ability to reach around the object and if you cannot reach the point to be measured you cannot scan it. Except in the instance of a computer controlled CMM, it is also strenuous to do a full scan of an object as the user must move the probe all over the object manually.

Classification into Active or Passive

3D scanners can be classified into active and passive scanners. An active scanner is one that emits some energy which interacts with the object being scanned, whereas a passive scanner does not emit any energy and instead relies on ambient forms of energy, such as ambient light. Both the active and the passive scanner types require a detector to detect energy coming from the object. An example of an active scanner is a laser scanner. All laser scanners fall into the active scanner category because they emit laser light which is reflected from the object being measured. An example of a passive scanner is an optical camera. A camera basically absorbs ambient light from a scene using a sensor, from which it forms a 2D image of the scene. Various algorithms and techniques have been developed within the research fields of computer vision and photogrammetry which enable 3D information to be extracted from 2D images [65].

Active scanners are more susceptible to interference and variations in environmental conditions, but tend to be more reliable when in optimal working conditions. Passive scanners have the advantage that they don't need an extra energy source as they do not emit any energy therefore making passive scanners an excellent choice for a mobile scanner [66]. Passive scanners typically have lower range and resolution than their active counterparts [60].

Classification by Medium of Interaction

A scanner's medium of interaction is the type of energy it emits/detects. This energy, prior to detection, must have interacted with the object being measured and therefore will contain information that can be used to generate a 3D model. The most common medium is electromagnetic radiation which includes X-ray, visible light, and laser light. Scanners that rely on electromagnetic radiation as media include laser scanners, camera-based scanners, and also CT scanners which use X-rays. These scanners have to deal with the possibility of interference from the sun or other radiation sources around.

Another possible medium is a magnetic field and an example of a scanner that uses a magnetic field as its medium of interaction is a Magnetic Resonance Imaging (MRI) scanner. MRI utilises the principle of magnetic resonance to generate an image of the internal structure of an object. This technique is commonly used in the medical field but has also been used in geology for 3D analysis of porous media structure and internal flow [67]. A magnetic scanner is limited because it cannot scan materials that are attracted or repelled by the magnetic field, although this would depend on the strength of the magnetic field been used by the scanner.

Sound waves have also been used as a medium for collecting 3D measurement data. In SONAR, they are used for scanning underwater objects [68] and to acquire 3D measurements for robot navigation [69]. They are also used in Ultrasonography, which is used extensively in the medical field to generate 3D views of the inside of the human body [70]. A very serious challenge to sound based scanners is the presence of environmental interference which could cancel out the emitted sound.

It is possible to combine the result of scans from multiple media to get more robust measurements. This is a common method in the robotics community where it is referred to as sensor fusion.

Another technique is where one type of energy is emitted and another type detected. For example in Thermo-acoustic tomography [71] where an electromagnetic signal is directed at a biological object with the intention of generating a thermo-acoustic response in the object which would lead to the emission of an ultrasound signal.

Classification by Principle of Operation

Scanners can also be grouped based on the techniques through which the 3D coordinates are computed. Depending on the medium of interaction used by the scanner any number of these techniques could be used to compute the 3D structure of an object. In [61, 56], an extensive discussion of scanners based on this criterion is presented. The techniques are as follows:

- **Triangulation**: Triangulation is the process of determining the position of an unknown object given its relationship (angle or distance) to objects whose position is known. Triangulation

scanners would typically observe a point(s) from multiple views (cameras or detectors) and utilize the known position and orientation of the observers to determine the position of the target point in space. Some laser triangulation scanners physically separate the laser source from the detector by a known distance and compute the location of the target point by solving the triangle formed by the laser source, the detector, and the point. Some laser triangulation scanners utilise two or more detectors to determine the position of the laser point. A dual camera laser scanner is illustrated in **Figure 2.12**. Triangulation is also the major principle behind stereoscopic and photogrammetric techniques. Stereoscopic techniques are computer vision techniques that use two or more cameras to extract 3D information from the world. When an object is viewed from two cameras (left and right) separated by a known distance, the left and right images would contain some similar points from the object. For each point in the left image the corresponding point in the right image is found. This is known as the correspondence problem, this problem is very difficult because points located in homogenous intensity regions would match with many other points in the same region. One way to solve the correspondence problem is to find and match unique features only. Once a correspondence is made the points can be triangulated to determine the distance.

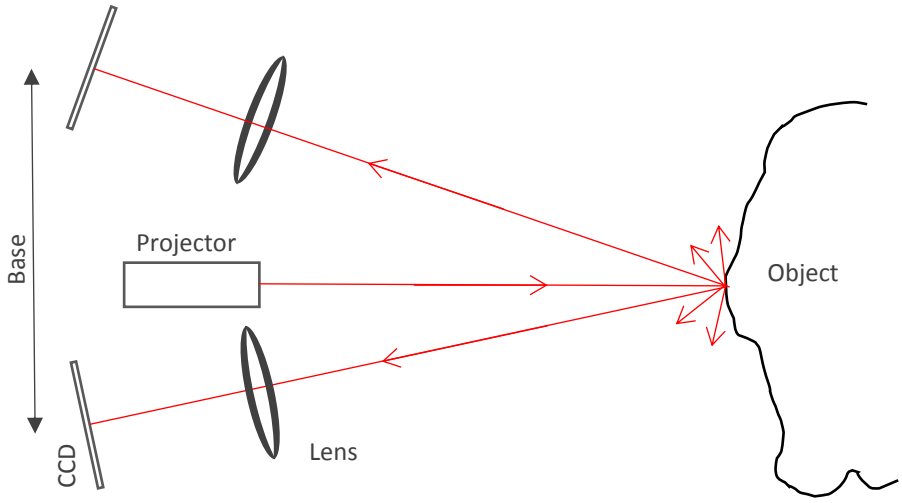

Figure 2.12: Laser triangulation using dual cameras. Two cameras (CCD and Lens of the cameras are shown) separated by a known distance (Base) are used to measure the position of a laser point projected on an object. Redrawn from [56]

Most scanners based on the shape-from-*x* methods (where *X* could be motion, shading, or video) use the principle of triangulation; they simply capture images of the object from multiple views and attempt to match a point or region from one image to the same points in the other images. The known or computed position of the cameras is then used to compute the position of that point or region. While some shape-from-*x* techniques utilize multiple cameras, others use one

camera and move the camera along a defined motion path or rotate the object; others shape-from-*x* techniques rely on a property of the camera (e.g. focus) or a property of the environment (e.g. lighting) to extract depth information [65].

- **Tomography**: Tomography refers to the cross-sectional imaging of an object from either transmission or reflection data collected by illuminating the object from many different directions [72]. In Computed Tomography (CT) [73, 57], X-rays are passed through an object from various directions in a plane or slice. When the rays leave the object they are detected and the attenuation of the X-rays from the different directions are used to form a set of projection images. Using tomographic reconstruction algorithms, the projections are combined into a single image. By acquiring a number of slices the technique is able to return the 3D structure of the object scanned. CT which was originally developed for use in the medical field has also found its way into industry. The benefit of tomography scanners is that they result in a 3D image of the object that includes internal features. One drawback is that the system must generate sufficiently strong energy that would pass through the object and still be detectable; the resulting effect of this is that the size of the objects and types of materials that can be scanned is limited [57]. Other forms of tomography [72] include Emission Computed Tomography, Ultrasonic Computed Tomography, and MRI.
- **Time of flight**: This is the simplest method of computing distance using the known speed of the medium of interaction; the time it takes the emitted energy to get to the target point and back is measured and the distance is computed. Although a very simple technique, lots of challenges can limit the use of this technique. The medium of interaction could be so fast that the timer circuitry is not able to give a reasonable time. The speed of various types of energy is affected by environmental conditions like temperature, and humidity. Time of flight is used in many lasers and sound based systems.
- **Interferometry or Pattern Projection**: This type of scanner operates by projecting a pattern on the object been scanned. A detector, usually a camera, is used to capture the resulting pattern from which the deformation of the projected pattern is determined. The projected pattern could be generated using laser interference, visible light, or infrared light. Pattern projection systems are affected by specular reflection, translucency and transparency in the object been scanned [74] and by any other surface type that makes it difficult to interpret the projected patterns. It excels in its ability to handle smooth surfaces which would pose a problem for many passive scanners. This technique could also be considered as a stereo-vision (triangulation) technique with one camera replaced by a projector. The correspondence (matching of points) problem is simplified by the introduction of codes into the projected pattern (see **Figure 2.13**)

- **Phase comparison**: The phase between the outgoing and incoming signals' waveform is compared to determine the difference. The position of the target is computed using the phase difference, the known speed and the frequency of the signal. Since this technique relies on the speed of the signal, it would also be affected by environmental conditions, as are the time of flight scanners.

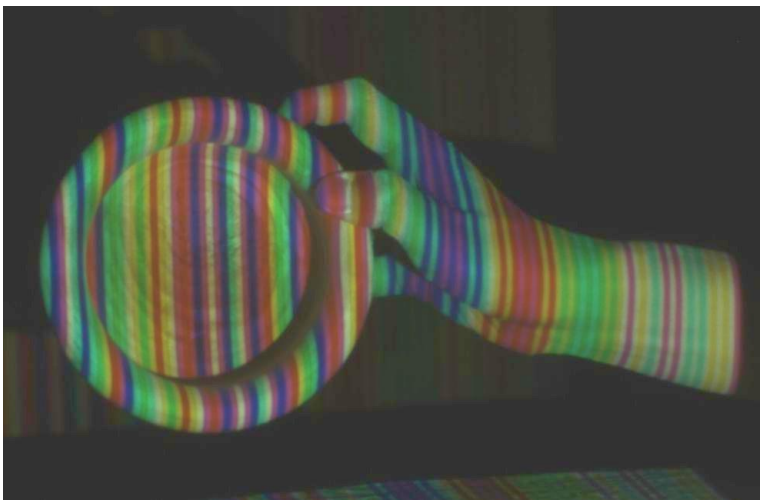

Figure 2.13: Coded structured light projected on a hand holding an object [75]

Classification by Scan Output

Another scheme is to classify scanners based on the output from the scan. The scanner could output a point, a surface, or a volumetric model. Point Scanners are able to return the position of a point on an object. Laser trackers and CMMs are examples of point scanners. Surface scanners are those that return the positions of a number of points on the surface of the object. Laser based scanners typically acquire a point (some a line) but the speed of the laser allows the system to acquire multiple points in a few seconds or minutes depending on the object size or equipment. Image-based scanners acquire the image of a surface and then extract the feature points that form the surface. Volumetric scanners such as MRI, CT, and micro CT scanners return a 3D model of the object including its internal structure, typically they output a sequence of cross-sectional slices that can be pieced together to form a volumetric model. Table 3.1, below summarises these various categorisations for some common scanning technologies.

It has been stated in the literature [56, 66, 60] that no single scanner exists that can handle all tasks in every application domain, and that the scanner needs to be selected to suit the task at hand. The accuracies of the different scanners are not easily comparable due to the large number of application domains, for example, a highly accurate MRI system used in the medical field could produce less accurate results, if applied to rock analysis. Boehler, et al [76] advocate that the consumer test the scanner to ensure that they are sufficiently accurate for their task. They also

designed tests to examine the range accuracy, angular accuracy, and resolution of Laser scanners and also examined the scanners' robustness to edge effects and surface reflectivity. Their results showed that even within the restricted class of lasers scanners, the accuracies and robustness to edge effect and surface reflectivity varied from one manufacturer to another. The next section now focuses on one of the scanning technologies of most immediate relevance to this project.

Technology	Proximity	Active or Passive	Medium	How it works	Output
Coordinate Measuring Machine	Contact	Passive	Touch	Reading joint variables from encoders and compute position of touch probe	Point
Laser tracker	Contact	Active	Laser	Time of flight/Phase comparison/Interferometry	Point
Laser scanner Triangulation	Non-Contact	Active	Laser	Triangulation	surface
Stereo-vision	Non-Contact	Passive	Visible Light	Triangulation of a single point or feature in multiple images	Surface
Photogrammetry	Non-Contact	Passive	Visible Light	Triangulation of a single point or feature in multiple images	surface
CT	Non-Contact	Active	X-ray, electron, neutron, Visible Light	Tomographic reconstruction using particle attenuation	Slices/ Volume
MRI	Non-Contact	Active	Magnetism & radio waves	Tomographic reconstruction using magnetic spin of atoms	Slices/ Volume
Ultrasonography	Non-Contact	Active	Sound	Uses time of flight of sound wave to determine 3D structure	Slices/ Volume

Table 2.2: Summary of the classification of scanners.

2.5.2 The Laser Tracker

Laser tracking systems can follow and determine the 3D position of a retro-reflective target. A retro-reflective target is an object that reflects the laser back in the same direction from which it came i.e. back to the laser tracker, from which it follows that laser trackers require a direct line of sight to the target. The target has a limited angle of acceptance; that is the angle of the incidence from which the laser would be reflected back to the tracker. Acceptance angles are typically around 30° to 120° depending on the system. The limited angle of acceptance means that there may often be a need to rotate the target when making measurements. Standard laser tracker retroreflectors, as shown in **Figure 2.14** are typically made of three reflective surfaces arranged in a mutually perpendicular configuration, with the vertex of these intersecting surfaces very accurately centred. Further information on retroreflectors can be found in [77].

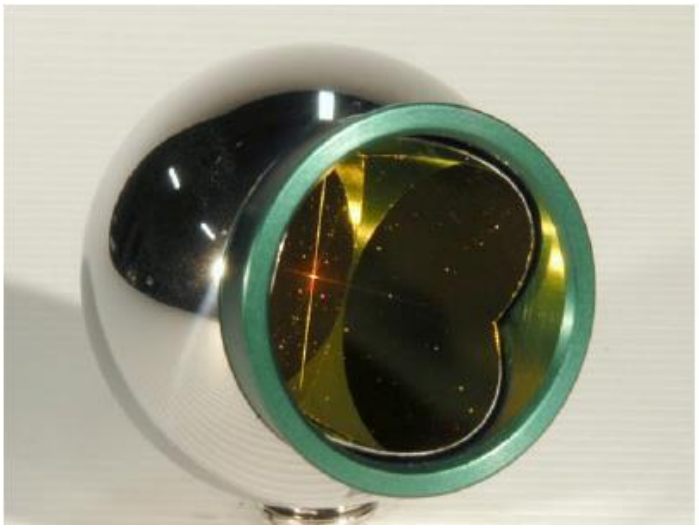

Figure 2.14: A spherically mounted retroreflective (SMR) target with gold-plated reflective surface.

The laser tracker is a spherical coordinate measurement instrument, this implies that, the laser tracker measures two angles (known as the azimuth and zenith angles) and a distance, as illustrated in **Figure 2.15**. The angular measurements are made using very accurate motor encoders in the tracker head and the distance to the target is measured using the laser beam. There are two dominant methods for computing the distance [78] as discussed below:

Incremental distance measurement (IDM): In this technique, an interferometer and a frequency-stabilised, helium-neon laser are used to monitor the change in distance from a baseline position. The laser beam is split in to two separate beams; one beam is sent towards the target and the other is kept within the tracker. The first beam is reflected off the target back into the tracker where the phase difference between both beams will generate an interference pattern. As the target moves closer or farther from the tracker by a fraction of the wavelength of the laser, a change

occurs in the interference pattern, see **Figure 2.16**. Counting the number of changes or fringe counts allows the tracker to determine the distance travelled by the target [79].

IDM does not provide a direct method of measuring the absolute distance travelled by the beam of light but rather measures the relative distance travelled. Another limitation of IDM is that the tracker loses count when the beam is broken so to ensure correct measurement the user must move the target back to the baseline position and then restart the measurement.

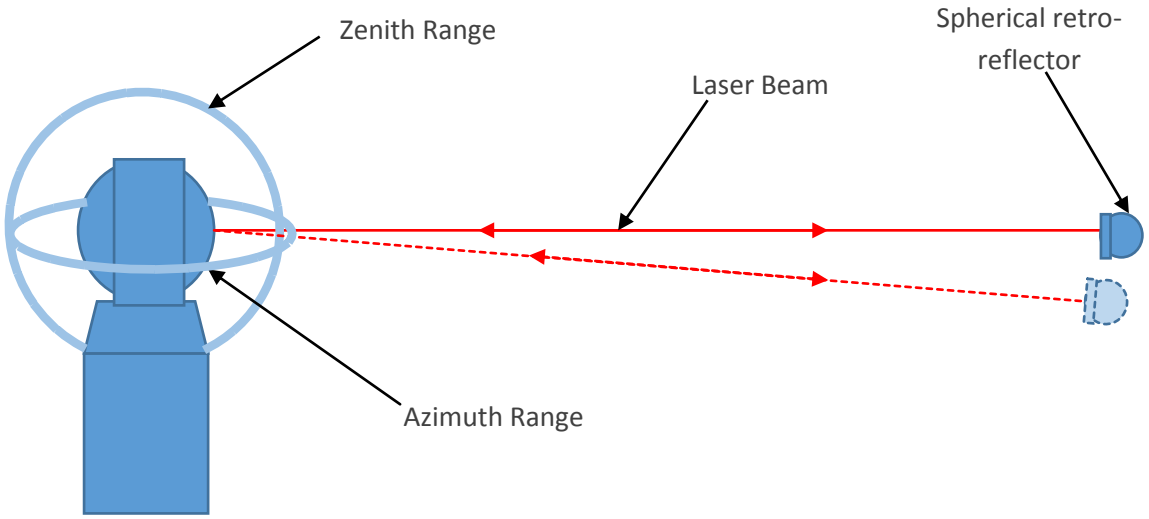

Figure 2.15: Illustration of the operation of a laser tracker**.** Two motors follow the target in the vertical (zenith) and horizontal (azimuth) direction and a laser beam is used to measure distance to the target. Cartesian coordinates are calculated using the zenith angle, azimuth angle, and distance.

Absolute distance measurement (ADM): ADM is a more direct measurement of the actual distance the beam has travelled in the atmosphere. ADM trackers use either time of flight or phase comparison to determine the actual distance travelled by the beam, as discussed in **Section 2.5.1**.

When ADM was first used in trackers, those trackers were slow and less accurate than the IDM trackers [79] but advancements have seen ADM trackers catch up with the IDM in terms of accuracy. ADM trackers have a longer integration time (the time required to determine the target's position) than the IDM technique because in IDM, as soon as the user stops moving the target, the count is already available but in ADM when the user stops some time is required to acquire a stable reading. To acquire the convenience of ADM (not restarting when the beam is broken) and the speed of IDM; researchers have come up with various methods to merge these techniques some of which are already being applied on commercial laser trackers [80]. These techniques are known as Absolute Interferometry (AIFM) [81].

Laser trackers as explained above lie on the border between contact and non-contact scanners and therefore inherit some of the merits of the contact and non-contact scanners but also suffer from some of the demerits of both groups.

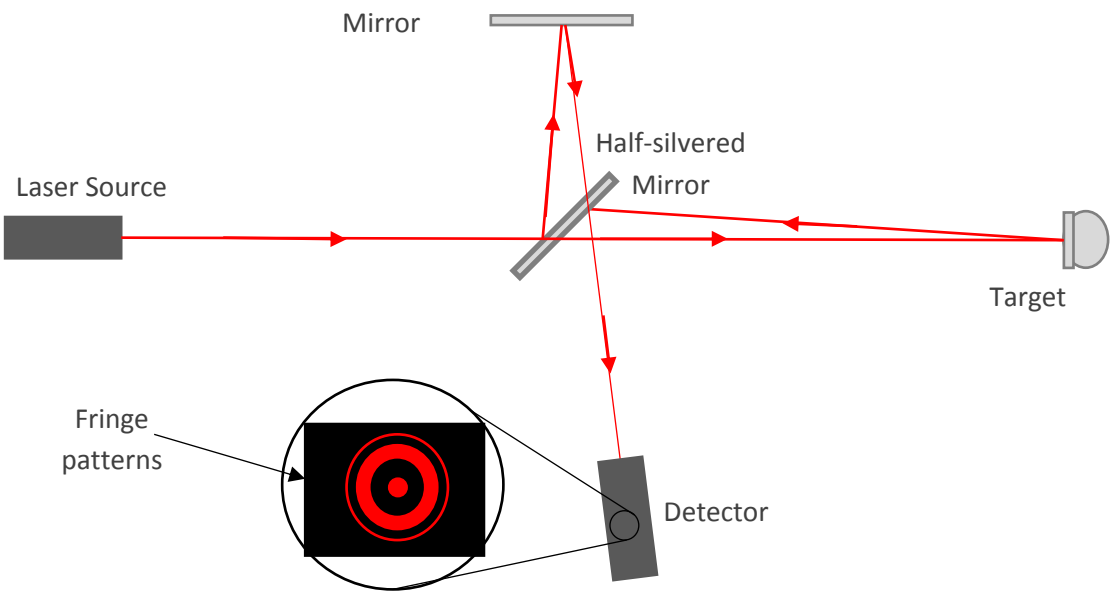

Figure 2.16: Illustration of a Michaelson interferometer showing the fringe patterns in the detector, caused by interference between the path length difference of the reflected and non-reflected light. As the target moves this difference in path length will change causing corresponding changes in the interference pattern.

2.6 Camera Systems

In this section, the fundamental theory underpinning camera based metrology is presented as camera based scanning technologies will be crucial for the solutions proposed in this thesis. The next sections discuss camera models and how they can be applied to 3D metrology.

2.6.1 Camera Model

The pinhole model is a simple and well understood camera model [82]. The pinhole model assumes that all optical rays pass through a single point known as the optical centre. Other models like the two plane model [83] exist in which the optical ray is not constrained to pass through a single point. The pinhole is the most used camera model in practical application and academic research which makes it attractive for this work as its high accuracy potential has already been demonstrated [84]. Given an arbitrary coordinate frame known as the world frame (X_w, Y_w, Z_w), the pinhole model represents the perspective projection[3] of a world point into a 2D image point as illustrated in **Figure 2.17**. This perspective projection is described mathematically in the equation below

[3] Perspective projection is a type of 3D to 2D projection model in which 3D points are projected onto the image plane by dividing them by their Z component.

$$\vartheta \underbrace{\begin{bmatrix} u \\ v \\ 1 \end{bmatrix}}_{m} = \underbrace{\begin{bmatrix} \boldsymbol{P_{11}} & \boldsymbol{P_{12}} & \boldsymbol{P_{13}} & \boldsymbol{P_{14}} \\ \boldsymbol{P_{21}} & \boldsymbol{P_{22}} & \boldsymbol{P_{23}} & \boldsymbol{P_{24}} \\ \boldsymbol{P_{31}} & \boldsymbol{P_{32}} & \boldsymbol{P_{33}} & \boldsymbol{P_{34}} \end{bmatrix}}_{P} \underbrace{\begin{bmatrix} X \\ Y \\ Z \\ 1 \end{bmatrix}}_{M} \quad 2.28$$

where $\boldsymbol{P}$ is the $3\,x\,4$ projective transformation matrix, M is the world point in homogenous coordinates[4], m is the image point in homogenous coordinates, and ϑ is a non-zero scale factor. The projective transformation matrix can be decomposed into two matrices $\boldsymbol{K}$ and $[\boldsymbol{R} \mid \boldsymbol{t}]$ such that $\boldsymbol{P} = \boldsymbol{K}[\boldsymbol{R} \mid \boldsymbol{t}]$. $\boldsymbol{K}$ is a 3 by 3 upper triangular matrix known as the intrinsic camera matrix which performs a mapping from the camera coordinate frame to the pixel coordinates. $\boldsymbol{K}$ consists of five parameters as shown below:

$$\boldsymbol{K} = \begin{bmatrix} sf & \gamma & u_0 \\ 0 & f & v_0 \\ 0 & 0 & 1 \end{bmatrix} \quad 2.29$$

where f is the focal length of the camera, s is a scaling factor used to account for non-square pixels, (u_0, v_0) is the image centre, also known as the principal point and γ is the skew between the sensor axis and the camera axis, in modern cameras the skew is typically zero.

$[\boldsymbol{R} \mid \boldsymbol{t}]$ is known as the extrinsic camera matrix and consists of a rotation matrix and translation vector. $[\boldsymbol{R} \mid \boldsymbol{t}]$ transforms a world point from the world coordinate frame to the camera coordinate frame. Since a rotation matrix can be represented as three parameters, the extrinsic parameters comprise six degrees of freedom. The projection of a point can be seen as two stage process, in the first stage the world point (X, Y, Z) is transformed into points in camera coordinate (X^c, Y^c, Z^c) using the extrinsic parameters. Then those points are transformed into image coordinates point $(\vartheta u, \vartheta v, \vartheta)$ using the intrinsic parameters. The 2D location (u, v) of the 3D point M in the camera image is then determined by dividing the image point by the scale factor ϑ. It is sometimes convenient to normalise the points in the camera coordinate frame before converting into image coordinates before performing the division; $(x, y, 1) = (\frac{X^c}{Z^c}, \frac{Y^c}{Z^c}, \frac{Z^c}{Z^c})$. Normalised camera coordinates are useful when computing lens distortion as discussed in the following section.

[4] In homogeneous coordinates, an extra dimension is appended to the vector e.g. $({}^{x}/_{w}, {}^{y}/_{w})$ becomes (x, y, w). This allows several transformation like rotation and translation be performed on a vector using a single matrix.

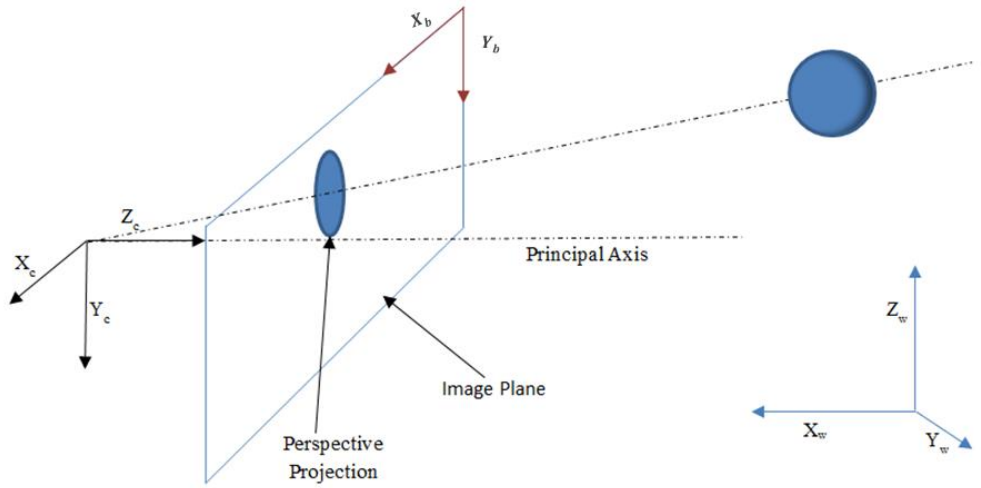

Figure 2.17: The perspective projection of a sphere. (X_W, Y_W, Z_W) is the world coordinate frame, (X_C, Y_C, Z_C) is the camera coordinate frame and (X_b, Y_b) is the image coordinate frame.

2.6.2 Geometric Lens Distortion

In the modern camera, the pinhole is replaced with lenses which are designed to collect more light while performing similar perspective projection. These lenses introduce several optical aberrations due to different flaws in the lens construction. One category of these optical aberrations is the geometric lens distortions which affect the shape of the projection. Geometric lens distortion will cause the world point to be projected to the wrong position and will affect the accuracy of any camera based metrology system. It is therefore important to correct for geometric lens distortion. The three types of distortion discussed in camera calibration literature are radial, tangential and thin prism distortions. The problem of modelling lens distortion can be stated mathematically as finding a function that maps a point (x, y) in the normalised camera coordinate frame to its corresponding distorted point (x_d, y_d) or vice versa.

1. **Radial distortion**: a distortion due to the fact that rays of light are bent more at the edges of the lens than at the centre of the lens. Radial distortion is typically classified into barrel distortion which is the negative distortion and pincushion distortion which is the positive distortion (although more complicated distortion patterns exist). Both barrel and pincushion distortion are illustrated in **Figure 2.18**. Several methods have been proposed to model radial lens distortion [85]. The most commonly used method is the polynomial model given in the equation below.

$$\delta_r = \begin{pmatrix} \delta x_r \\ \delta y_r \end{pmatrix} = \begin{pmatrix} x(k_1 r^2 + k_2 r^4 + k_3 r^6) \\ y(k_1 r^2 + k_2 r^4 + k_3 r^6) \end{pmatrix} \quad 2.30$$

$$r^2 = x^2 + y^2$$

Commonly, the undistorted point is used to compute the distorted point as shown in the equation above even though it is more suitable to compute the undistorted point using the distorted point because the distorted points are directly observable from the image whereas the undistorted points are not [86]. A lens subject to radial distortion can be calibrated independently (without other intrinsic or extrinsic parameters) using several methods

- The Plumb-line method: These method use the principle that straight lines in the world should correspond to straight lines in the image, but lens distortion causes lines in the world to map to curves in the image [87].
- Cross-ratio invariance: The cross ratio of the set of colinear points in the real world is the same as the cross ratio of projected points in the image [85], where, A, B, C, D are four distinct points, then their cross ratio is defined to be $\frac{AC}{CB} / \frac{AD}{DB}$.
- Multiple view geometry: Some authors attempt to exploit multiple view geometry in the determination of radial distortion of a camera. Fitzgibbon [88] proposed a linear method that estimated both the fundamental matrix (discussed in **Section 2.6.4**) and the radial lens distortion. The author proposed a new model to represent the radial distortion. The method assumes that the radial distortion from both cameras are the same which may not be the case in a stereo camera system[5].

2. **Tangential (Decentring) distortion**: a distortion caused by improper alignment of the optical centre of the lens and the principal point of the camera (see **Figure 2.18b)**. It is modelled using the equation below which consists of a radial and non-radial component. It is commonly assumed to be negligible for many applications [89].

$$\delta_d = \begin{pmatrix} \delta u_d \\ \delta v_d \end{pmatrix} = \begin{pmatrix} 2p_1xy + p_2(r^2 + 2x^2) \\ p_1(r^2 + 2y^2) + 2p_2xy \end{pmatrix} \quad 2.31$$

3. **Thin prism distortion**: a distortion also caused by improper alignment, in particular when the camera sensor is not orthogonal to the lens assembly. This situation could arise due to imperfections in the lens design and manufacturing or in the camera assembly [86]. It is modelled using the equation below.

$$\delta_t = \begin{pmatrix} \delta u_t \\ \delta v_t \end{pmatrix} = \begin{pmatrix} s_1(x^2 + y^2) \\ s_2(x^2 + y^2) \end{pmatrix} \quad 2.32$$

The total lens distortion is the sum of all the types of distortion (**Equation 2.33**). Determining lens distortion accurately is a non-trivial problem since both thin-prism and tangential distortion could contribute to the radial error [86]. Many camera calibration techniques determine the total lens

[5] It should be noted that a multi-view system could be built by moving a single camera to multiple positions or by using multiple cameras.

distortion by finding the distortion parameters $(k_1, k_2, k_3, p_1, p_2, s_1, s_2)$ that minimize a selected calibration error function. The distorted image point $(u_d, v_d, 1)$ is determined by multiplying the distorted normalised camera point $(x_d, y_d, 1)^T$ by the intrinsic camera matrix as detailed above.

$$\begin{pmatrix} x_d \\ y_d \end{pmatrix} = \begin{pmatrix} x \\ y \end{pmatrix} + \delta_r + \delta_d + \delta_t \qquad 2.33$$

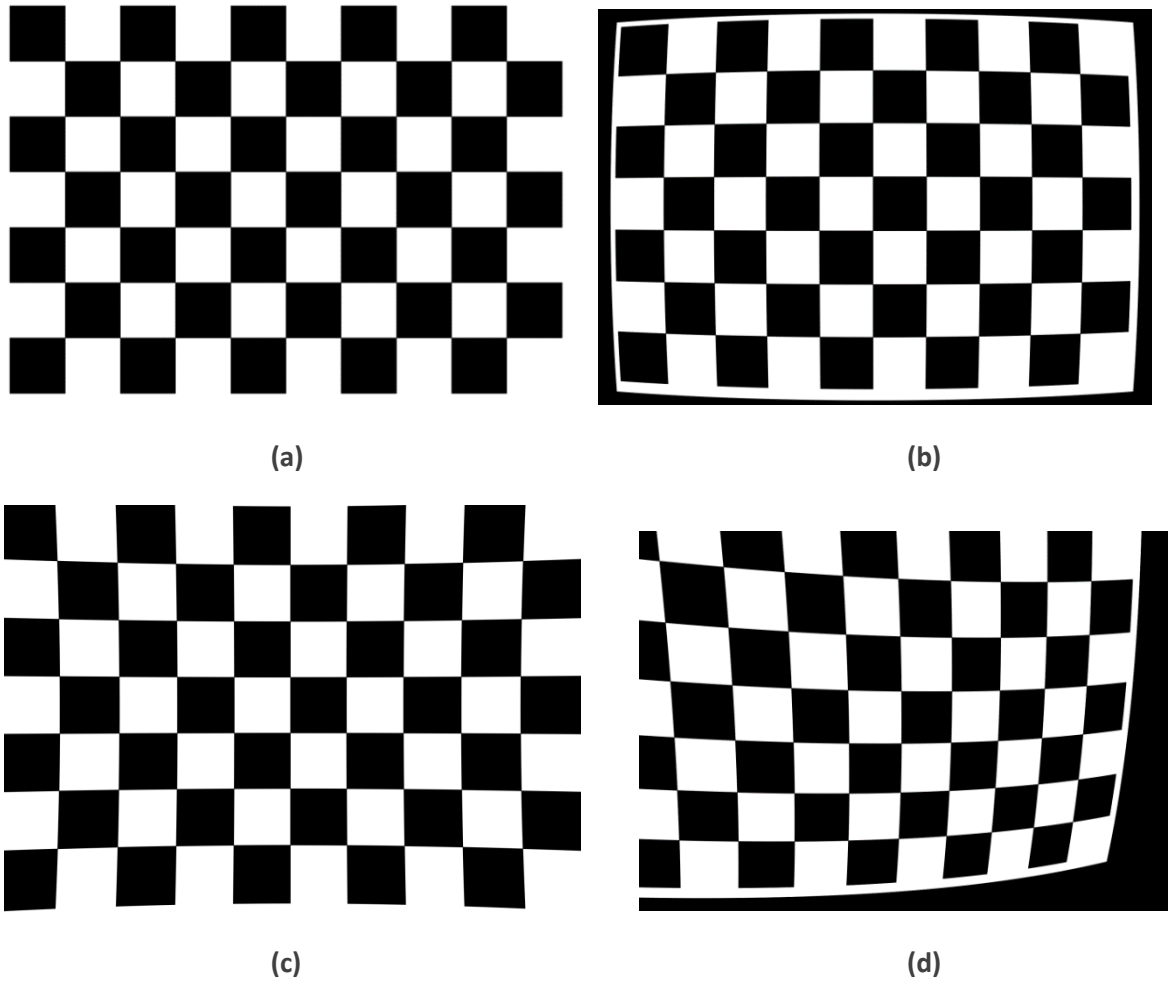

Figure 2.18: Illustration of a checkerboard with **(a)** No distortion **(b)** Barrel distortion **(c)** Pincushion distortion **(d)** Tangential distortion

2.6.3 Camera Calibration

Camera calibration attempts to find the intrinsic and extrinsic parameters (typically 5 intrinsic and 6 extrinsic) for a camera. If lens distortion is modelled, those parameters must also be determined. Most cameras will contain some distortion therefore to achieve high accuracy; lens distortion should be accounted for. Some assumptions are typically made to reduce the number of parameters to be found. One such assumption is that the pixels on the sensor are perfectly square or that the principal point is in the middle of the image. It is also common to assume that the skew is zero. Camera

calibration typically involves using a calibration apparatus containing known points, such apparatus could be 1D, 2D or 3D. Other methods utilise some knowledge of camera motion or scene knowledge like the presence of vanishing points. It is recommended to use a calibration apparatus to achieve the highest accuracy [82].

Three dimensional grid

Calibration may be performed using a three dimensional object with known geometry i.e. the Euclidean distance between points on the object is known. It is also possible to use a planar object which is translated very accurately to give a 3D set of points. Hall et al [90] proposed a method that assumes no radial distortion is present. They attempt to directly estimate the entries of the camera projection matrix with a linear least squares formulation. Tsai [91] proposed a two stage calibration method using the Radial Alignment Constraint. The principal point of the camera is assumed to be known and only radial distortion is modelled. Several improvements to the original technique have been proposed [92]. Weng et al [86] proposed a method which also used a different distortion model that included tangential and thin prism distortion alongside radial distortion.

Two dimensional grid

Using this approach, a planar grid containing calibration points is used for calibration. The appeal of two dimensional calibration objects arises from their easy setup. It is possible to print such objects using a desktop printer as opposed to the more complicated manufacture required by a 3D target however the achievable accuracy could be limited by the print quality. The printed grid should be attached to a rigid, flat surface. Many techniques require the 2D pattern be shown to the camera at multiple orientations and positions, while others estimate the camera parameters from a single image of the grid. Any two images of the same planar surface are related by a 3 by 3 matrix known as a homography. Homographies can be estimated when the same points in one image are visible in the second image; a minimum of four points are required for this estimation. Zhang [82] proposed a technique that recovers homographies of the planar grid which has been shown to the camera at different positions and orientations. The camera parameters are later recovered from the homographies.

One dimensional grid

Calibration may be performed using a calibration object consisting of a set of collinear points with known distances between them. This is also known as wand calibration [93] and is commonly used by the motion capture community to calibrate their systems. The benefit of wand calibration arises when calibrating multiple cameras as the wand minimizes the possibility of occlusion of the

calibration points. Zhang [82] proposed a closed form technique for calibration using a 1D object with a minimum of three points of known distance. He proved, using the number of equations and the number of unknowns, that it is impossible to calibrate with a freely moving 1D object but it is possible when one end of the object is fixed and when at least three points are present. Mitchelson and Adrian [93] proposed a technique that uses a 1D object with two points of known distance. Their technique requires the use of a multi camera setup therefore cannot be used to calibrate a single camera. They used non-linear minimization to obtain the camera parameters. The initial guess for the focal length of the cameras are extracted using the fundamental matrix (discussed in the next section) and image centre and scaling factor of the cameras are assumed to be known.

Vanishing point or Known Motion

These techniques assume some understanding of the scene or the motion of the camera. They could be less accurate than the previous methods if the vanishing points are not correctly extracted from the image or the camera motion deviates from the planned trajectory. This method is not discussed in more details but the reader is referred to [94].

Self-calibration

Self-calibration attempts to calibrate the camera with no calibration apparatus. It is also known as auto-calibration. Self-calibration attempts to estimate a large number of parameters with no calibration apparatus which leads to a harder mathematical problem. Self-calibration methods are therefore less accurate than the techniques using calibration objects [82].

2.6.4 Epipolar Geometry

In perspective projection, the distance of a 3D point from the camera (also known as the depth) is lost and cannot be recovered without some extra information. It is possible to reconstruct the three dimensional position of a point by triangulation from two or more calibrated camera views. As mentioned in **Section 2.5.1**, a non-trivial problem that needs to be solved in triangulation systems is the correspondence problem. The correspondence problem refers to the problem of determining which point of one image corresponds to a point in another image. A common method of finding correspondence is by exploiting the geometry of the multi-camera setup, this geometry is typically called epipolar geometry.

Suppose a world point $\boldsymbol{X}$ is viewed from two cameras as shown in **Figure 2.19** or by a single camera moved to two distinct positions. The image plane π_i of each view would contain a projection of the world point denoted as $\boldsymbol{x_1}$ and $\boldsymbol{x_2}$ for the first and second camera respectively. The plane formed by $\boldsymbol{X}$ and the camera centres O_1 and O_2 is known as the epipolar plane and the vector between the two

camera centres (i.e. the origin of the camera coordinate frame) is known as the baseline. The projections $\boldsymbol{x_1}$ and $\boldsymbol{x_2}$ of point $\boldsymbol{X}$ would also lie on the epipolar plane. With this information, the search for a corresponding point could be constrained to a single line (the epipolar line) which is the intersection between the epipolar plane and the respective image plane. This constraint, known as the epipolar constraint, is mathematically represented by the fundamental matrix.

The Fundamental Matrix

The Fundamental matrix [95] is a 3 by 3 matrix that can be derived using the extrinsic and intrinsic parameters of both cameras as shown in **Equation 2.34**. Given the extrinsic parameters of the two cameras in homogeneous matrix form ($\boldsymbol{C_1}, \boldsymbol{C_2}$) the fundamental matrix $\boldsymbol{F}$ can be computed using the equation below.

$$\begin{aligned} \boldsymbol{C_2}.(\boldsymbol{C_1})^{-1} &= {}^{2}\boldsymbol{C_1} = [\boldsymbol{R}|\boldsymbol{t}] \\ \boldsymbol{E} &= [\boldsymbol{t}]_x\boldsymbol{R} \\ \boldsymbol{F} &= \boldsymbol{K_2^{-T}EK_1^{-1}} \end{aligned} \qquad 2.34$$

where $[\boldsymbol{R}|\boldsymbol{t}]$ is the rigid transformation from the first camera frame to the second camera frame with rotation component $\boldsymbol{R}$ and translation component $\boldsymbol{t}$ as shown in **Figure 2.19**, $[\boldsymbol{t}]_x$ is a skew symmetric matrix created using the translation vector $\boldsymbol{t}$, $\boldsymbol{E}$ is typically known as the Essential Matrix [96] and $\boldsymbol{K_1}, \boldsymbol{K_2}$ are the intrinsic camera matrices for the first and second cameras respectively.

Although the fundamental matrix can be computed using the camera parameters, in the absence of these several methods also exist to estimate the fundamental matrix using point correspondences only. The reader is directed to [97] for more details on such methods. Using the fundamental matrix, the Epipolar constraint between the corresponding image points $\boldsymbol{x_1}$ and $\boldsymbol{x_2}$ is given by **Equation 2.35**. Any pair of corresponding points must satisfy the equation below but the presence of noise and distortion would invalidate the relationship.

$$\boldsymbol{x_2 F x_1^T} = 0 \qquad 2.35$$

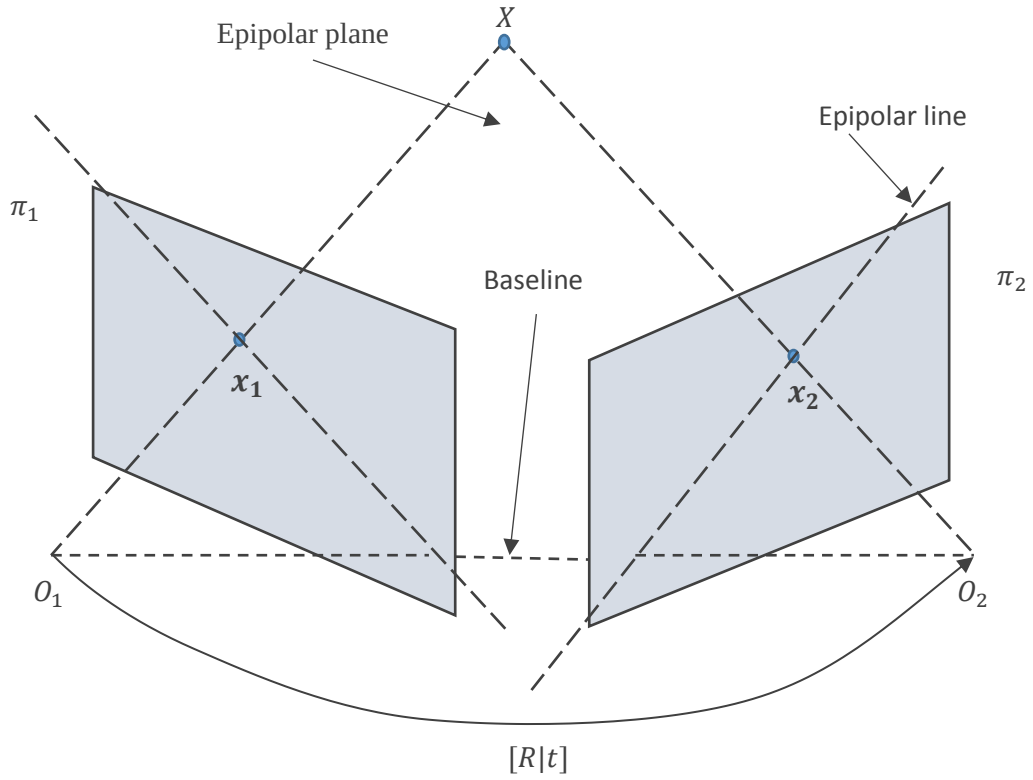

Figure 2.19: Epipolar geometry between two cameras with image planes (π_1, π_2) and camera centres (O_1, O_2). The 3D Point X projects onto the respective cameras as image points(x_1, x_2). The 3D point and camera centres form the Epipolar plane and the intersection between the Epipolar plane and the image plane determines the Epipolar Line.

2.6.5 3D Triangulation

Theoretically, triangulation should be as easy as finding the intersection between the back-projected rays from two or more images (such as in **Figure 2.19**) but in practice the rays from these cameras do not intersect, as shown in **Figure 2.20**, due to camera calibration error and quantization error (error due to sampling from continuous light signal). Several methods have been proposed to account for the non-intersecting rays such as the midpoint algorithm which proposed to find the shortest line between the two rays and return the midpoint of the line as the results from the triangulation but this method has been demonstrated to give poor result [98].

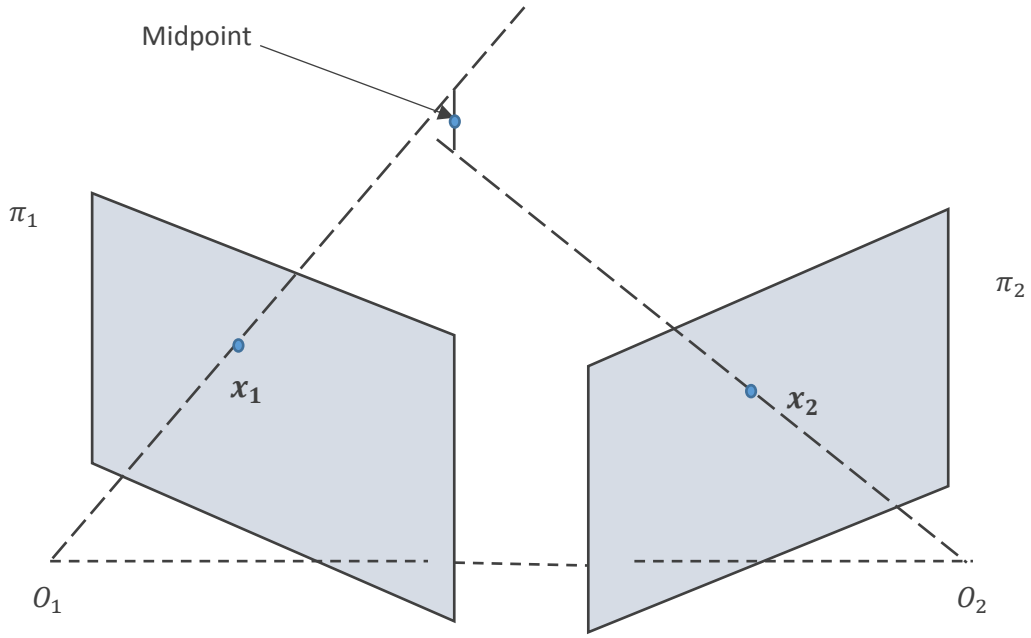

Figure 2.20: Triangulation from two image views showing non intersecting camera rays and the midpoint method.

A commonly used method in computer vision is the linear least square method [98] which finds the 3D point that minimises the projection error in the two images. Given a 2D point $\boldsymbol{x_1} = (u_1, v_1, 1)$ from one camera and its corresponding point $\boldsymbol{x_2} = (u_2, v_2, 1)$ in the second camera and the projection matrices for both cameras (P_1, P_2), the linear least square method finds the 3D point $\boldsymbol{X}$ that satisfies the projection equations for both cameras i.e. $\boldsymbol{x_1} = P_1\boldsymbol{X}$, $\boldsymbol{x_2} = P_2\boldsymbol{X}$**.** The projection equations for both cameras can be rearranged into an equation of the form $A\boldsymbol{X} = 0$ as shown in **Equation 2.36** where $(P_1)_i$ is the i^{th} row of P_1. This equation can be solved using singular value decomposition.

$$\underbrace{\begin{bmatrix} \boldsymbol{u_1}(P_1)_3 - (P_1)_1 \\ \boldsymbol{v_1}(P_1)_3 - (P_1)_2 \\ \boldsymbol{u_2}(P_2)_3 - (P_2)_1 \\ \boldsymbol{v_2}(P_2)_3 - (P_2)_2 \end{bmatrix}}_{A} \boldsymbol{X} = \boldsymbol{0} \qquad 2.36$$

3 Modelling of Positioning Systems

As discussed in **Section 2.2.3**, model based alignment techniques have several benefits that make them very appealing especially when complex samples are involved. Model based alignment solutions such as the SScanSS package work to the extent that the virtual laboratory on which they are based corresponds, in terms of sample position, coordinate systems and characteristics of moving components, (such as the sample positioning system), to the real laboratory. Although neutron beam-line instruments are designed and built to very high specifications there are circumstances where this correspondence may not be adequate. At the most basic level, moving components, such as jaws, collimators and most importantly sample positioning systems, often, over time, develop accuracy issues, that may cause a divergence between the real behaviour and the ideal kinematics assumed in the modelled system. The effect of using inaccurate kinematic parameters can be very significant, particularly in relation to more complex positioning systems such as the 3 or 6 axis revolute manipulators which are of increasing interest as sample positioning systems [3, 9].

The question addressed in this chapter is how to acquire more accurate models of imperfect or complex systems, be they sample positioning systems, jaws or detectors.

3.1 Methodology

All the model based alignment techniques reviewed in **Section 2.2.3** used kinematic models for their planning. Kinematic models are popular because they require no knowledge of the forces causing the motion, for example using a dynamic model could require the user to know the mass of the sample and the velocities applied to the joints of the positioning system. Practically, it would be non-trivial and in some neutron diffractometers impossible for dynamic models to be used. This could also defeat one of the major benefits of the model based alignment which is ability of the user to plan their experiment in advance. Hence in this work, we continue to use the kinematic models for representing the moving systems. The kinematic model parameters used to design a positioning system would typically be provided by the manufacturer[6] but insufficient construction tolerance typically leads to the real kinematic parameters of the manipulator being different from the manufacturer's design parameters

In this chapter, the use of kinematic calibration techniques (**Section 2.4**) from the field of robotics to determine the kinematic parameters of both off-the-shelf and custom built positioning systems is proposed. Using a measuring device, these kinematic parameters can be estimated from

[6] In the case of simple positioning systems, idealized kinematic parameters are typically assumed

measurements taken from the positioning system and then be used for more accurate instrument control or simulation. The pipeline for the proposed solution shown in **Figure 3.1**, follows the standard robot calibration steps of modelling, measurement, parameter identification, and implementation which were reviewed in **Chapter 2**. The proposed solution is discussed in more details in the next section. Experimental evaluation of the proposed method requires particular functionalities such as a numeric inverse kinematic solver [14] and graphical rendering which, due to time constraints, cannot be built from scratch for this project so a pre-existing package- SScanSS is used to demonstrate the performance of the methods. However the methods developed in this thesis are generally applicable. The functionality already provided by the SScanSS package is not addressed in this work. The approach is illustrated using positioning systems on the ENGIN-X instrument at the UK's ISIS pulsed neutron source, but again the methods could be applied to other neutron and synchrotron instrument hardware

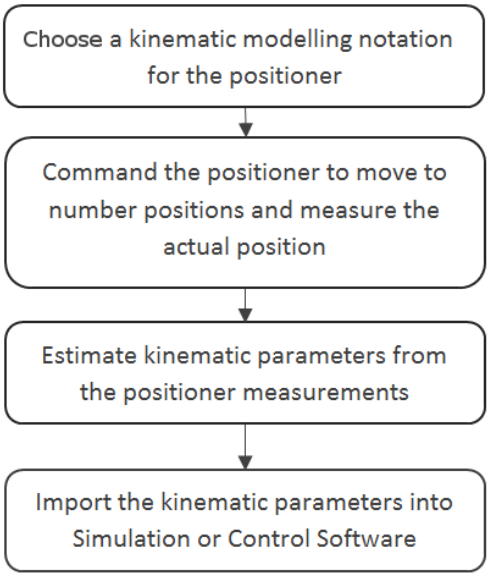

Figure 3.1: The pipeline for the proposed solution

It should be noted that earlier results from the work presented in this chapter have already been published [99] but that several measurements have been repeated since that publication. Any significant differences will be pointed out in the text.

3.2 Calibration for Diffractometers

This section discusses some of the important considerations for applying calibration techniques to diffractometers in general but some of the considerations are particular to the SSCANSS/ENGIN-X combination which is used to illustrate the methods.

3.2.1 Kinematic Modelling Notation

Other than the three selection criteria in **Section 2.4.1** of completeness, proportionality, and equivalence, which should be a priority, the selection of a modelling notation would depend on the modelling convention of the simulation or control software where the kinematic parameters would be used. SScanSS originally employed a modified version of the four parameter DH notation (**Section 2.3.2**) which is an incomplete notation (i.e. a notation that is unable to represent all possible variation that could occur in the kinematic structure of the manipulator). With the DH notation, a serial manipulator with n joints requires $\mathrm{n}+1$ coordinate frames and $4 \times \mathrm{n}$ parameters for its representation. Since six numbers are required to specify the position and orientation of an arbitrary coordinate frame in space, the DH notation requires the additional constraints that i) the $\mathrm{x_n}$ axis intersects both $\mathrm{z_{n-1}}$ and $\mathrm{z_n}$ axes and ii) that the $\mathrm{x_n}$ axis is perpendicular to both the $\mathrm{z_{n-1}}$ and $\mathrm{z_n}$ axes. Industrial robots are typically designed to respect these constraints, but calibration can reveal that such constraints are broken [37]. Generally, beam line positioning systems are not designed with conscious reference to these constraints so that the standard DH parameters may typically not be sufficient to represent these systems. To solve this problem, the modified DH notation of Hayati and Mirmirani [37] is used instead. In this modified DH notation, an extra parameter β_i, is used to represent the rotation around the axis y_i of joint $i+1$. Under this system $5 \times \mathrm{n}$ parameters describe a manipulator with n joints.

The transformation from coordinate frame $i-1$ to i is now computed by multiplying rotation and translation matrices formed using the five parameters as shown below

$$^{i-1}A_{\,i} = Rot_z(\theta_i).Trans_z(d_i).Rot_x(\alpha_i).Trans_x(r_i).Rot_y(\beta_i) \tag{3.1}$$

$$^{i-1}A_{\,i} = \begin{bmatrix} \cos\beta_i \cos\theta_i - \sin\alpha_i \sin\beta_i \sin\theta_i & -\sin\theta_i \cos\alpha_i & \sin\beta_i \cos\theta_i + \sin\alpha_i \cos\beta_i \sin\theta_i & r_i \cos\theta_i \\ \cos\beta_i \sin\theta_i + \sin\alpha_i \sin\beta_i \cos\theta_i & \cos\theta_i \cos\alpha_i & \sin\beta_i \sin\theta_i - \sin\alpha_i \cos\beta_i \cos\theta_i & r_i \sin\theta_i \\ -z \cos\alpha_i \sin\beta_i & \sin\alpha_i & \cos\alpha_i \cos\beta_i & d_i \\ 0 & 0 & 0 & 1 \end{bmatrix} \tag{3.2}$$

Where $Rot_k()$ is a homogeneous transformation matrix where the rotation component is a rotation about the k axis and $Trans_k()$ is a homogenous matrix which contains a translation along the k axis. The homogenous matrix $^{i-1}A_i$ represents the transformation from the $i-1^{th}$ coordinate frame to the i^{th} coordinate frame. The transformation from the frame placed at the base of the robot to the frame placed at the end point of the robot (the forward kinematics) remains the same as the normal DH Notation.

It should be noted that the choice of the modified DH notation is to allow for compatibility with the selected simulation software and that the methods developed in this thesis are not constrained to

any model. The proposed method was, in fact, initially developed using the Quaternion-Vector model discussed in **Section 2.3.2** and later changed to utilize the DH notation. Due to the equivalence property, it is known that the choice of model should not affect the accuracy of the calibration.

3.2.2 Pose Measurements

Accuracy is the priority for neutron diffractometer sample positioning therefore the most accurate measurement device available at the instrument should be used for the calibration. The selected measurement device should be able to measure to the desired accuracy in the workspace of the manipulator. Essentially the measurement device should be more repeatable and accurate than the positioning system being calibrated. If this is not the case the measurement device would limit the accuracy achieved by the calibration process. A variety of measurement devices have been used in the calibration research (**Section 2.4.2**) but the calibration of any arbitrary manipulator would require at least a 3D measuring device. The measurement device available for this project was a FARO Vantage laser tracker whose accuracy is discussed in the next section.

Laser Tracker Accuracy

The laser tracker used was sent to the manufacturer for calibration and was reported to be within the manufacturer specification[7] after servicing. Before using the tracker, the accuracy of the laser tracker was tested, using the manufacturer designed tests, and was found to be typically around 20 microns under stable temperature conditions. The tracker is an absolute distance measurement (ADM) tracker which requires the target to be stable before taking a measurement. The tracker is equipped with a weather (temperature, pressure, humidity) sensor to measure environmental variation so as to compensate for their effects on the laser beam. Although the tracker can utilize up to four weather sensors; only a single sensor was available. This sensor would typically be mounted close to the tracker. This implies the tracker would not compensate for environmental variations at a distance from the tracker. All necessary measures were taken to ensure the environmental variations were minimal during all measurement, for example, all room heating and cooling equipment were switched off during calibration.

The accuracy of a laser tracking system depends on the accuracy of its subsystems, which consists of a distance measurement system (using the laser) and two motor encoders (azimuth and zenith). The accuracy of the laser system could be improved by limiting the error from any one of these subsystems. A method of minimizing the total error from the laser tracker is to reduce the distance

[7] Maximum permissible error for measuring a 2.3m horizontal scale bar at a range of 2m is 44 microns but error is typically 22 microns.

travelled by the laser beam hence the laser tracker was positioned as close as possible to the manipulator being calibrated to minimize the accuracy loss due to distance. The 2m range was rarely exceeded so expected accuracy should be similar to the stated specification. Another method of minimizing the error from the laser tracker is to disable the azimuth and zenith motors and make measurements with the laser beam only. This method might not be possible in every scenario; an alternative would be to reduce the angular range within which the measurements are made because small angular errors are typically magnified by distance.

The SMR used with the laser tracker was a 1.5 inch Standard Accuracy Break Resistant SMR also from FARO. The break resistant target features a single element retroreflector with a gold coating. The vertex of the single element reflector is centred within ± 0.0076mm. Other manufacturer recommended best practices were followed to ensure the best accuracy [100].

Automation of the Calibration Measurements

In addition to accuracy of the measurements, another very important consideration is the automation of the measurement process as this can have the following benefits:

- The complete automation of the measurements process is necessary in order to minimise human error as a large number of measurements are required to be made.
- Automation would also to allow the measurement be repeated as many times as required with minimal variation due to differing human operators in each run.
- Automation of the calibration process is essential if the calibration process is to be carried out by non-experts.
- A one click calibration process would be essential to avoid unnoticed errors from being inputted into the simulation software.

Therefore, when possible the measurements were automated in this project. A system architecture that enables the automation of measurements is presented in **Section 3.3.1**.

3.2.3 Numerical or Geometrical Calibration?

The different methods for parameter identification were presented in **Section 2.4.3**. Here we re-examine these methods with specific reference to neutron diffractometers. The accuracy required for sample alignment in a stress measurement experiment is typically taken to be a function of the size of the gauge volume used. A general rule of thumb cited within the neutron diffraction community is that the positioning system should be capable of positioning the sample within an accuracy of 10% of the smallest dimension of the gauge volume of the instrument [12]. The smallest

gauge volume routinely used for experiments is $1 \times 1 \times 1mm^3$, suggesting a positioning accuracy of approximately 0.1mm[8].

It is desirable to select a calibration method that gives the most accuracy and parametric methods are typically more accurate than circle-point-analysis (CPA) because they can find kinematic parameters that account for some of the non-geometric errors in the measurements whereas CPA would account for geometric errors only. In reality however, non-geometric error typically account for only a small percentage of the total positioning error therefore modelling non-geometric errors might not be necessary.

Other broader considerations need to be taken into account, for example CPA has the advantages of being easily implemented and validated since no minimization or Jacobians are required by the technique. This could allow personnel to make intuitive decisions when calibrating a new system. For example, if space restriction prevents personnel from measuring a full circle it is possible to omit some points and still fit a reasonable circle, but with the parametric method it is less intuitively obvious how to handle such a situation. CPA also has the advantage of requiring no knowledge of the existing kinematic parameters of the manipulator, which makes it suitable for custom-built positioning systems whose kinematic parameters are unknown; as is the case with many positioning systems at neutron diffractometers.

It should be noted that robot calibration techniques in general are not guaranteed to generate models that look like the physical robot which might be a problem if such models are also used for training, visual orientation or collision detection as well as for control (see **Figure 3.12**). One possible solution to this problem would be to maintain two separate models, the calibrated model which would be used for sample alignment and a CAD model used for the collision detection. This problem could arise in both parametric methods and CPA but it could be managed in the parametric methods by setting some constrains in the minimization problem.

Because neutron diffractometers mostly utilise custom-built positioning systems and in the light of the practical operational issues discussed above, it was decided to choose the CPA method over a parametric method. When further accuracy is deemed to be necessary the non-geometric errors could be modelled separately. This is the approach taken in this thesis.

3.2.4 Implementation

As part of the implementation stage, the extracted kinematic parameters would be included into SScanSS to evaluate the performance of the calibrated model experimentally. The experimental

[8] In the case of X-ray diffraction a typical gauge volume size could be as small as 0.1mm which indicates a positional accuracy of 0.01mm. This accuracy can be achieved in calibration by using a measuring device with sufficient accuracy.

evaluation of the system is presented in **Chapter 5**. In the next section, an example of the CPA method applied to a removable three axis manipulator and a XYZΩ positioning table as used on the ENGIN-X instrument is presented.

3.3 Case Study I: ENGIN-X Instrument

The standard positioning system used on the ENGIN-X instrument is a positioning table but when necessary the positioning table can be augmented with supplementary systems such as a revolute manipulator. The ENGIN-X positioning table is a custom-built manipulator with four stages[9] arranged in order, (bottom to top) of Z, Ω, Y, and X. The maximum payload that can be lifted is specified as 1000Kg. The ENGIN-X Revolute manipulator shown in **Figure 3.2** is a portable, custom-built, robotic manipulator designed by Cybaman Technologies with 3 revolute joints[10]; all having a range of -180° to 180°. The maximum payload that can be lifted is specified as 25Kg. The end effector is a breadboard mounting plate to which samples are attached. At ENGIN-X, the joints of the revolute manipulator are labelled from top to bottom using alphabetic characters; so the topmost joint is Joint A and the base Joint is Joint C. This convention is also used in this thesis. A typical setup of table and revolute manipulator is shown in **Figure 3.2**. The operational advantage of using the revolute manipulator, in conjunction with the positioning table, is that it allows greater flexibility in terms of sample orientation and, in particular, allows the automated measurement of three orthogonal strain components without requiring the sample to be removed, manually rotated and re-mounted.

Given that, in common with much similar ancillary equipment in use on beam-lines, the revolute manipulator is not used for all experiments; the table and revolute manipulator were calibrated separately, and a method for combining them into a single manipulator model was developed.

3.3.1 System Architecture

The system architecture illustrated in **Figure 3.3** was proposed and implemented for taking the measurements at ENGIN-X to ensure the minimal errors and good repeatability of the measurements. A measurement server was created which communicates with the laser tracker system installed on ENGIN-X. The server software which was written using the C++ programming language communicated with the metrology device via the software development kits (SDK) provided by the equipment manufacturer. The server abstracts away the complexity of using the laser tracker and make it as simple as sending a TCP request to the server.

[9] Each stage uses encoders for motion feedback and limit switches to prevent the stage from exceeding the physical or desired travel limits for the axis.

[10] Due to a damaged motor driver, results published in [100], were for two joints only but the driver has since been repaired so all three joints are reported here.

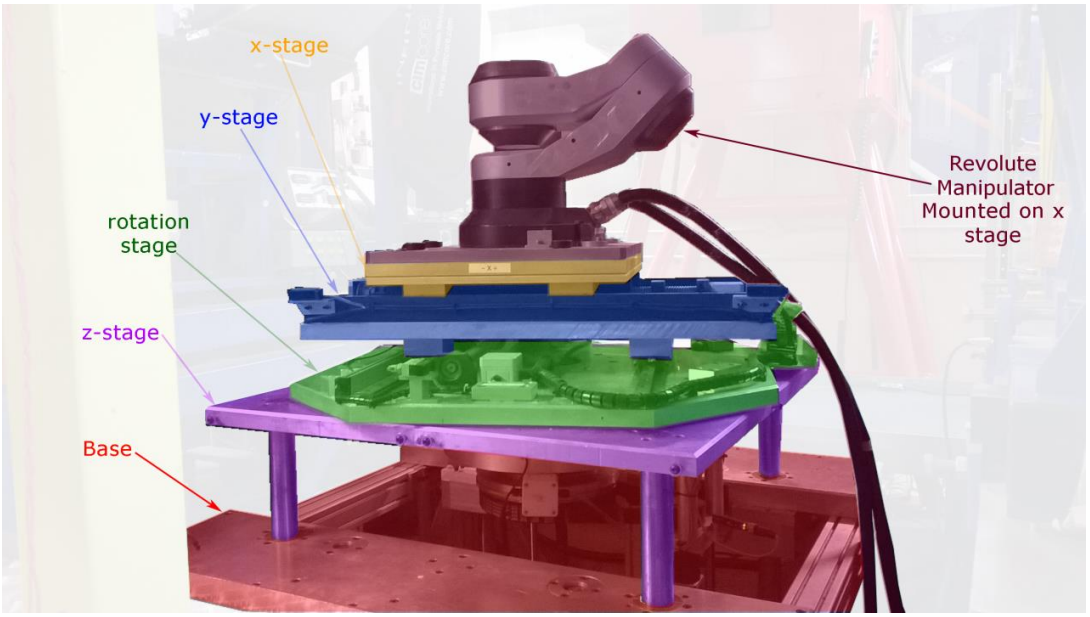

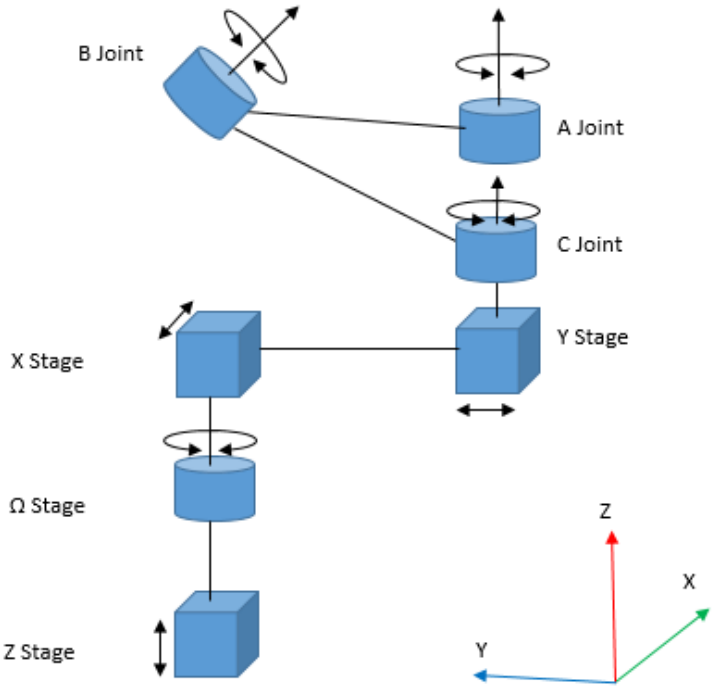

Figure 3.2: The XYZΩ stage and the revolute manipulator of the ENGIN-X Instrument (Top) and, a schematic diagram of the combined XYZΩ and revolute manipulators showing all the revolute joints as cylinders and the prismatic joints as cubes with arrows to indicate direction of translation or rotation (below).

The ENGIN-X instrument can be controlled via Open Genie scripting [101]. The script allows granular control of the positioner and other ancillary devices with a few lines of code. For example, the X axis

of the positioning table could be commanded to move to the 100mm position with 0.1mm accuracy using a single line of code like **CHECK_POS /X 100 0.1**. The procedure doesn't return until the X axis arrives at the desired position within the requested tolerance. Although the instrument control scripts would be written in Open Genie, when necessary the script sends the appropriate command via TCP to the measurement server. A simple TCP request sent to the measurement server could be used to measure the position of an SMR attached to the moving axis or the server could be configured to take several measurements and output the measured points to a file or the console.

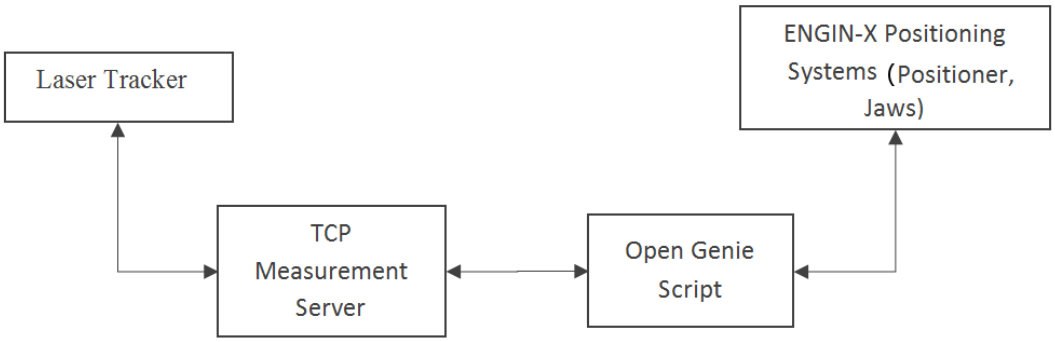

Figure 3.3: The system architecture developed for taking measurements on the ENGIN-X instrument.

This architecture allowed the automation of several of the calibration and evaluation measurements presented in this chapter. One major limitation to complete automation of the entire measurements is the requirement that the SMR continues to face the laser tracker all through the measurement process. Therefore measuring a very large translation or rotation would require manual rotation of the SMR to keep the beam. Complete automation could be achieved by using a motorised SMR [41] that moves to maintain the laser beam.

3.3.2 Repeatability Analysis

As discussed in **Section 2.3.3**, it is not possible to achieve accuracies higher than the repeatability of the manipulator, therefore understanding the repeatability of the positioning system is vital to understand the limits on the achievable accuracy. This section presents the results of repeatability tests performed on the ENGIN-X positioning system (table and revolute manipulator). Before carrying out the tests, it was important to determine the joint limits of the positioning table. The knowledge of the joint limits is required for selecting the configurations for the tests. The limits were found by manually jogging the positioners and recording the sensor positions at which the positioner stopped at the limit switch. The joint limits and calculated travel for each joint are shown in **Appendix A**.

Procedure for Determining Repeatability

The repeatability tests were performed for three poses (sets of joint configurations). These configurations are denoted as configurations A to C. In each configuration, thirty one measurements were made to determine the repeatability of the positioner in that pose. The initial configurations were selected in a systematic way in order to sample the workspace. The repeatability tests were performed using the laser tracker and the 1.5 inch SMR in the ENGIN-X instrument hutch. The SMR was attached rigidly on the revolute manipulator (which was mounted on the positioner). It should be noted that the repeatability of both positioners are characterised independently i.e. the revolute manipulator was not commanded to move while the repeatability of the positioning table was characterised and vice versa. The entire tests used for the evaluation of repeatability were fully automated using the system architecture described in **Section 3.3.1** therefore no human intervention was required after the initial setup. For a single test, thirty new configurations were generated by adding random offsets[11] to the initial configuration. An Open Genie script was written to perform the following

1. Command the positioner to move to the initial configuration and measure the initial position of the SMR.
2. Set variable $i = 1$.
3. Command the positioner to move to the i^{th} configuration.
4. Command the positioner to return to the initial configuration and wait for a few seconds for stability after the move is completed.
5. Command the laser tracker to measure the position of the SMR.
6. Set $i = i + 1$
7. Repeat steps 3-6 until all configurations have been reached.

Every time the positioner reached the initial configuration, a measurement was taken which gave a total of thirty one measurements. These thirty one measurements were taken at a single configuration and constituted a single test. All tests were repeated a minimum of three times at each configuration to reduce the bias that could arise from any laser tracker issues. Minimization of random errors from the laser tracker was necessary to get the best results; this was done by keeping the laser beam stationary at the initial configuration and disabling the azimuth and zenith motors hence ensuring that the repeatability of the measurements depended largely on the repeatability of the laser distance measurement system and that the only moving object in these tests was the positioner being tested. For this measurement technique to work, an assumption was made that the

[11] These random offsets were generated using a random number generator and scaled to ensure the positioning system did not run into the limit switch.

repeatability of the positioners were good enough to ensure that the SMR was returned back to within its angle of acceptance so the beam is never lost when the target is returned to the initial configuration. The assumption was found to be valid for all the ENGIN-X positioning systems tested.

Repeatability can be classified into unidirectional and bidirectional repeatability. If the positions on the individual joints are always approached from the same direction, this is known as unidirectional repeatability. Bidirectional repeatability is when a joint position is approached from both directions. Unidirectional repeatability values are typically better than that of bidirectional repeatability tests [33] due to the presence of backlash and other dynamic errors when direction of a moving joint is reversed. Only bidirectional tests were conducted and the results from these tests are discussed in next section.

Repeatability Results for the Positioning Table

The selection of configurations for repeatability is considered something of a black art in the field of robotics as no approved systematic method exists for the selection. Mooring and Pack [32] proposed the method in which a Jacobian (see **Section 2.4.3**) based joint index is used to select the configurations for the repeatability tests. They suggest that the repeatability measurements be made at the configuration with the worst and average joint index. They proved mathematically that the worst joint index for a particular joint should be achieved when the end effector is farthest from that joint, hence that joint would contribute more to the repeatability errors. This seems reasonable; for example, considering the manipulator in **Figure 3.4**, small angular errors in the base joint should make larger contribution to the repeatability error for the pose shown in **Figure 3.4b** than that in **Figure 3.4a** because of the increased radius. Their method requires the knowledge of the kinematic parameters of the manipulator in advance which may not be available and also the method would not work for prismatic joints because, in the Jacobian matrix, a unit displacement of a prismatic joint always leads to a unit displacement of the end effector. The joint index method was deemed unsuitable for this project because of the challenges above.

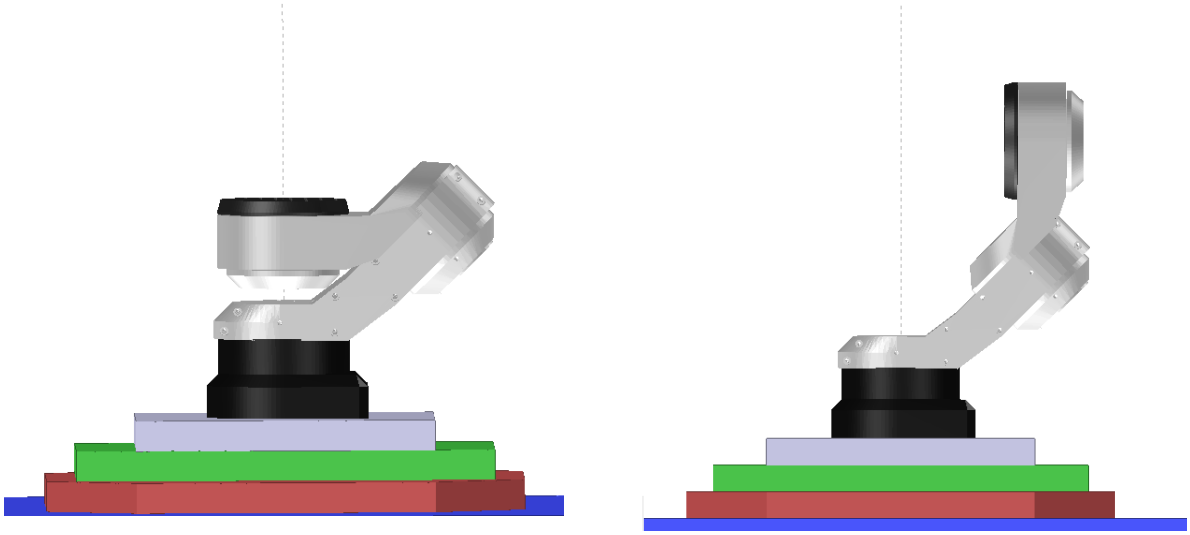

(a) **(b)**

Figure 3.4: Illustration of a manipulator in two different configurations. Configuration **(a)** is the zero configuration of the manipulator and configuration **(b)** has one of the joints rotated by 180 degrees.

The configurations used for the ENGIN-X manipulators were selected using a combination of kinematic intuition (such as the one demonstrated above) and knowledge of the manipulator design specification. For example it was mention by one of the instrument scientists that in the specification of the positioning table the edges of the table were allowed to have less tolerance than the centre of the table therefore some configurations were selected near the joint limits to validate this claim. The configurations used to assess the repeatability of the positioning table are presented in **Table 3.1**. Configuration A was selected to be at the zero point of all joints which is located near the centre of travel for each joint. Configurations B and C were selected to be close to the upper and lower joint limits respectively**.**

	X (mm)	**Y (mm)**	**Z (mm)**	**Ω (deg)**
A	0.000	0.000	0.000	0.000
B	200.000	200.000	200.000	165.000
C	-200.000	-200.000	-200.000	-165.000

Table 3.1: The joint configurations used for the repeatability tests on the ENGIN-X positioner.

From the results in the **Table 3.2**, it is clear that the repeatability of the ENGIN-X positioning table as is common with many other manipulators, varies over the workspace. These tests were done using multi-axis control (all joints were commanded to move together to the desired position). The Euclidean distance from the measured point to the origin of the laser tracker's coordinate frame was

computed, then the standard deviation and maximum deviation from the average are used to analyse the repeatability of the positioning table.

	1st Attempt	2nd Attempt	3rd Attempt
Configuration A			
Std. dev.	0.00926	0.00905	0.00412
Maximum	0.04430	0.03292	0.03209
Configuration B			
Std. dev.	0.01082	0.00783	0.00827
Maximum	0.06566	0.06096	0.05739
Configuration C			
Std. dev.	0.01316	0.01310	0.01406
Maximum	0.03721	0.03574	0.03683

Table 3.2: The results from the multi-axis repeatability tests on the ENGIN-X positioner. The standard deviation and the largest deviation from the average (in mm) are presented for all the configurations.

The best repeatability is obtained at the centre of travel of all joints which is configuration A and degraded slightly as the manipulator approached the joint limits represented by configuration B and C. Assuming a normal distribution of the errors, the deviation of the manipulator from a commanded position would be below the standard deviation for 68.3% of the observations and below three multiplied by the standard deviation (according to the 3-sigma rule [102]) for 99.7% of the observations. Therefore at configuration C (Attempt 3), deviations are expected to fall under 0.04218 mm (3 x 0.01406 mm) 997 times out of 1000 and under 0.01406 mm 683 times. To confirm whether the 3-sigma rule is applicable, each set of measurements were evaluated using the Shapiro-Wilk normality test [103] and a q-q plot [104]. These evaluations revealed that the measurements from configuration A were normally distributed with a long tail which implies that the repeatability of the positioning table at configuration A would have more outliers than the 3-sigma rule predicts. Towards the joint limits (i.e. configuration B and C), the measurements start to deviate from normality. A closer look at the measurements (**Figure 3.5a**) at configuration C shows that all three attempts are strongly correlated which would suggest that the source of the variations is non-random. For comparison, the measurements[12] for configuration A are shown in **Figure 3.5b**.

[12] Configuration A and B measurements show similar random behaviour therefore only Configuration A is shown.

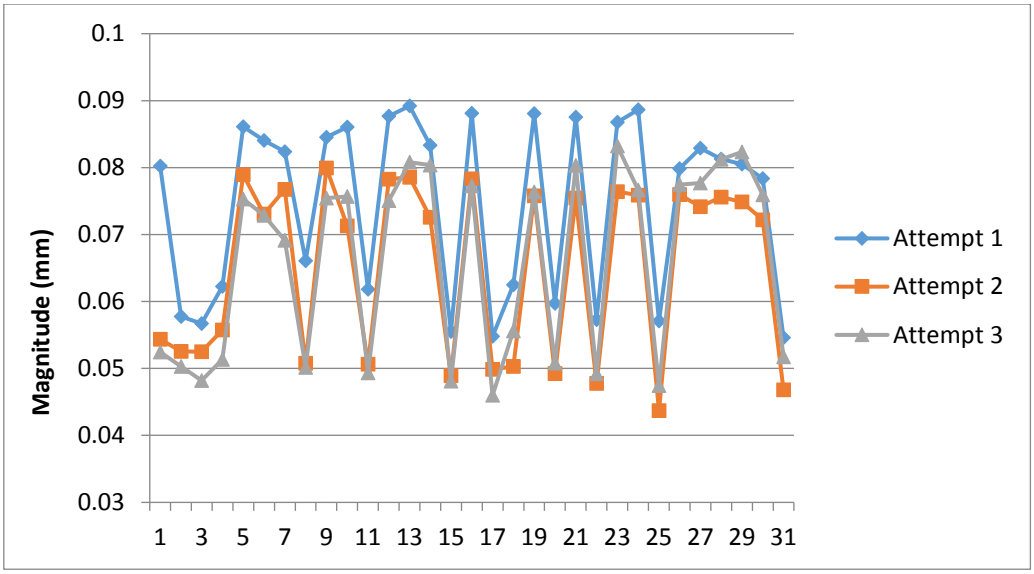

(a)

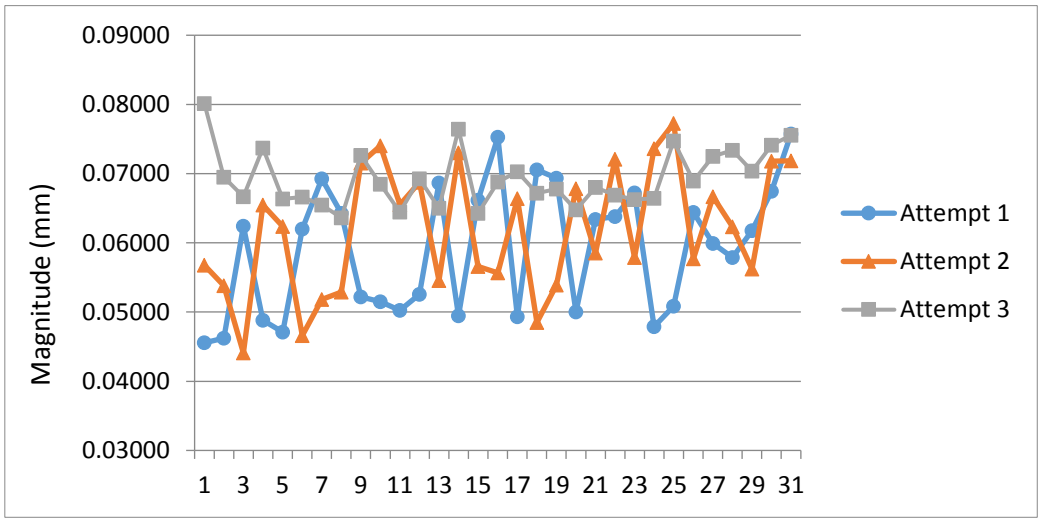

(b)

Figure 3.5: A plot of the 31 measurements used to access the repeatability in **Table 3.2**, **(a)** data from configuration C[13] **(b)** data from configuration A.

Non-random error would indicate the presence of a repeatable error source that can be fixed but due to the small size of the error, this was not investigated. It is typically expected that the repeatability of single-axis control (a single axis is actuated at a time) should be better than the multi-axis control mainly because keeping the other joints fixed should reduce cross-coupling error (when the movement of one stage causes another stage to move). Hence the repeatability tests were repeated (with the same 30 configurations used for the multi-axis tests) on the positioning

[13] The magnitude axis of the plot for configuration C is adjusted to allow easy comparison with the plot for configuration A.

table using the single-axis control to evaluate if this assumption holds for the positioning table. The results from those tests are presented in the table below

	1st Attempt	2nd Attempt	3rd Attempt
Configuration A			
Std. dev.	0.00750	0.00932	0.00961
Maximum	0.02249	0.02795	0.02882
Configuration B			
Std. dev.	0.00669	0.01299	0.00999
Maximum	0.02008	0.03898	0.02996
Configuration C			
Std. dev.	0.01547	0.01395	0.01607
Maximum	0.04640	0.04185	0.04821

Table 3.3: The results from the single-axis repeatability tests on the ENGIN-X positioner. The standard deviation and the largest deviation from the average (in mm) are presented for all the configurations.

On first impression **Table 3.3**, suggest that the repeatability of the single axis control tests does not vary significantly from the multi-axis control results. But a closer look at the maximum deviations for configurations A and B, indicates that the single-axis control consistently resulted in less outliers than the multi-axis control, even though the standard deviations are similar. The results remained normally distributed with a long tail but the tail is shorter than for the previous test, which could indicate that the single-axis control is more reliable than the multi-axis control. The main exception was Configuration C which like the multi-axis control was found to not be normally distributed. The measurements for configuration C had the same profile as shown in **Figure 3.5a.**

From the evaluation above, the repeatability of the positioning table would be stated to be below 0.050mm (which is the manufacturer specified value) at the centre and deteriorates towards the extremes with the assumption that there is no extreme variation in between the selected configurations.

Repeatability Results for the Revolute Manipulator

The configurations used to assess the repeatability of the revolute manipulator are presented in **Table 3.4**. Configuration A was selected to be at the zero point of all joints. Configuration B was selected to be close to the joint limits for all joints except joint C while configuration C is selected to be near the midpoint between the zero point and the joint limits for all joints except joint C**.** The

values used for joint C were intentionally kept below 40° to ensure line of sight visibility to the laser tracker.

Configuration	Joint A (deg)	Joint B (deg)	Joint C (deg)
A	0.00	0.00	0.00
B	165.00	-165.00	-30.00
C	-75.00	90.00	35.00

Table 3.4: The joint configurations used for the repeatability tests on the revolute manipulator.

The repeatability tests on the revolute manipulator were performed using single axis control. The Euclidean distance from the measured point to the origin of the laser tracker's coordinate frame was computed, and the standard deviation and maximum deviation from the average were then calculated. Results are presented in **Table 3.5**, from which it appears that the repeatability of the revolute manipulator varies minimally over its workspace. The measurements from all configurations were determined to be normally distributed using the same tests mentioned above. Therefore the bidirectional repeatability of this revolute manipulator could be stated to be around 0.016mm (3–sigma of the maximum in **Table 3.5**) when unloaded also with the assumption that there is no extreme variation in between the selected configurations.

	1st Attempt	2nd Attempt	3rd Attempt
Configuration A			
Std. dev.	0.00505	0.00427	0.00298
Maximum	0.01151	0.00890	0.00701
Configuration B			
Std. dev.	0.00319	0.00479	0.00221
Maximum	0.00619	0.00864	0.00648
Configuration C			
Std. dev.	0.00378	0.00518	0.00295
Maximum	0.00759	0.00973	0.00630

Table 3.5: The results from the single-axis repeatability tests on the revolute manipulator. The standard deviation and the largest deviation from the average (in mm) are presented for all the configurations.

It should be noted that the repeatability of a positioning system typically varies with both the speed and acceleration of the positioning hardware, but since these values are fixed by the ISIS motion control team, the effect of changing these parameters is not evaluated. Theoretically increasing

these variables should degrade the repeatability (because of higher possibility of overshooting the selected joint position) while decreasing the value should improve the repeatability.

3.3.3 Description of Calibration

A custom tool, shown in **Figure 3.6**, was mounted at the end effector of the manipulator. The tool has a magnetic end to allow attachment of the target (SMR). The SMR on the end of the tool was manually tilted or rotated to maintain it facing the tracker beam. The tool was mounted with an offset from the relevant centres of rotation so that the rotation of the revolute joints resulted in the SMR following a circular path, the minimum size of the offset would depend on the behaviour of the circle fitting algorithm selected. All Joints on the manipulator being calibrated were set to the zero position (0° or 0mm). Beginning from the topmost joint the manipulator was then moved, throughout its range, in fixed increments and the position of the SMR measured at each step. The joint was then returned to its zero position and the same procedure repeated for the next joint in the chain, until the base (or bottom) joint was reached so all joints were moved during the measurement process. The measured points were passed into an IDL [105] function implementing the CPA algorithm (**Algorithm 2.1**). The output from the CPA algorithm is the identified joint axes and centre points; these were passed to another function written in IDL that utilized vector algebra and Euler angle analysis to extract the 5 modified DH parameters.

Figure 3.6: The custom tool used for the calibration experiment with the 1.5'' SMR.

3.3.4 Conversion from Axis/Point to DH notation

In this section, a new method to convert from identified joint axes and centre points to the modified DH notation is presented. A few techniques have been proposed to extract modelling parameters from measured joint axes and centres. Barker [106] used vector algebra to extract standard DH parameters from identified axes and points. He developed equations for the cases where the consecutive joint axes were skewed, parallel, or intersecting. Sklar [53] used an equation which he termed the 'mutual moment equation' to determine if a pair of joint axes was intersecting, skew or parallel. He derived a set of equations for determining the DH parameters for each category. Rajeevlochana et al [107] used line geometry, Plücker coordinate and dual vector algebra to determine if two consecutive joint axes are skewed, parallel, or intersecting then used that knowledge to compute the standard DH parameters of the serial manipulator. Stone [40] proposed a method in which coordinate frames are assigned to each link using the measurements and then used to derive the parameters for his modelling notation known as the S-model. The S-model parameters could then be converted into standard DH parameters. Here a method similar to Stone's method is proposed but the modified DH parameters are derived directly instead of via S-model parameters. Similar to Stone's method, the proposed method begins by assigning a coordinate frame, but in this case a coordinate frame is assigned only to the first link in the manipulator. This coordinate frame could be the same as the measuring system, a known instrument coordinate frame or any arbitrary frame. All the measured joint axes and centres must be placed in this coordinate frame. Given two joint axes, it is trivial to calculate the rotation matrix M that aligns the first axis with the second. When M is computed, it can be decoupled into four rotation matrices as shown in **Equation 3.3** where θ_i, α_i, β_i are the same as in **Equation 3.1** and γ_{i+1} is a joint offset for the next link which is included to deal with the arbitrary assignment of coordinate frames. It can be seen from **Equation 3.3** that if θ_i is removed from M, the other parameter can be determined by solving for X-Y-Z euler angles. The proposed algorithm relies on these concepts to decouple the DH parameters from the rotation matrix. The basic algorithm for the method is given below.

$$M = Rot_z(\theta_i).\underbrace{Rot_x(\alpha_i).Rot_y(\beta_i).Rot_z(\gamma_{i+1})}_{xyz\ Euler\ Angles} \tag{3.3}$$

Given a set of measured joint axes $\boldsymbol{J}$ and joint centres $\boldsymbol{C}$ which have been placed in the assigned first link coordinate frame, the DH parameters would be denoted as in equation above where i is the link index. Let $i = 0$, $\gamma_i = 0.0$ and M_i be a 3 x 3 identity matrix.

1. Calculate a vector from the centre of joint i to joint $i + 1$ as shown below

$$V_i = \boldsymbol{C_{i+1}} - \boldsymbol{C_i}$$

When $i+1$ exceeds the number of joints, the end effector position should be used to compute the vector.

2. Rotate the vector into the coordinate frame of the first link

$$\widehat{V}_i = {M_i}^T \ . \ V_i$$

3. Calculate the link length r_i and the link offset d_i of link i using $\widehat{V}_i$. The components of $\widehat{V}_i$ is denoted as $[V_x \quad V_y \quad V_z]$. The link length is the magnitude of the x and y component of $\widehat{V}_i$ while the link offset is the z component.

$$r_i = \sqrt{{V_x}^2 + {V_y}^2}$$

$$d_i = V_z$$

4. Calculate the joint offset θ_i for link i

$$\theta_i = atan2\left(\frac{V_y}{V_x}\right)$$

5. Create a rotation matrix R_z using the calculated θ_i value.

$$R_z = \begin{bmatrix} \cos(\theta_i) & -\sin(\theta_i) & 0 \\ \sin(\theta_i) & \cos(\theta_i) & 0 \\ 0 & 0 & 1 \end{bmatrix}$$

6. Determine the rotation matrix M_{i+1} that rotates the first joint axis J_0 to joint axis J_{i+1}. This can be done using the shortest arc quaternion algorithm [108].

7. Decouple the joint offset θ_i from M_i which as explained above would give a matrix $\widehat{M}$ which can easily be decomposed into X-Y-Z Euler angle.

$$\widehat{M} = (M_i \, . R_z)^T \ . \ M_{i+1}$$

8. Update the joint offset θ_i

$$`\theta_i = \ \theta_i + \ \gamma_i$$

9. Decompose the matrix $\widehat{M}$ into xyz Euler angles $(\alpha_i \quad \beta_i \quad \gamma_{i+1})$ where α_i is the joint twist, β_i is the Hayati parameter and γ_{i+1} is the joint offset for link $i+1$. One shortcoming of using Euler angles is that when β_i is 90°, the joint twist and the joint offset for the next link becomes inseparable. In such a situation, the derived DH parameters would still be mathematically correct but they might not agree with the nominal DH parameters (if known).

$$\alpha_i = atan2\left(\frac{-\widehat{M}_{12}}{\widehat{M}_{22}}\right)$$

$$\beta_i = \ tan2\left(\frac{-\widehat{M}_{02}}{\sqrt{{\widehat{M}_{12}}^2 + \ {\widehat{M}_{22}}^2}}\right)$$

$$\gamma_{i+1} = atan2\left(\frac{-\widehat{M}_{01}}{\widehat{M}_{00}}\right)$$

10. Set $i = i + 1$ and repeat steps 1 to 9 for the remaining links.

The resulting DH parameters from the algorithm above can now be applied directly into the simulation software of choice. After extracting the DH parameters from the measured data, it is vital to validate the accuracy of the DH parameters (how closely the model corresponds to the physical system). The accuracy analysis is presented in the next section.

3.3.5 Accuracy Evaluation of Kinematic parameters

The accuracy of the calibration was measured using metrics proposed in the ANSI/RIA R15.05-1-1992 (R1999) standard [109]. A set of N joint configurations were randomly generated for both manipulators. The physical manipulator was commanded to move to each configuration and the end effector position P_A was measured using the laser tracker and SMR. The calibrated kinematic model was then used to calculate the model end effector position P_C for the same joint configurations. The difference between P_{C_i} and P_{A_i} gives the error between the calibrated model and the actual manipulator for the i^{th} joint configuration. The overall accuracy is simply the mean of the magnitude of each of the errors for the N configurations, as shown in **Equation 3.4** below. The ANSI standard recommends that $N \geq 50$ configurations are used and the resulting mean is called the Static Position Accuracy (SPA).

$$SPA = \frac{1}{N}\sum_{i=1}^{N}\left\|P_{A_i} - P_{C_i}\right\| \qquad 3.4$$

Both manipulators were tested using 100 (instead of the minimum 50 used in [99]) randomly generated joint configurations and the end effector positions were measured. It may be noted that because residual stress measurements are made with the measurement point positioned over the centre of rotation of the XYZΩ table, errors in the rotation table do not produce corresponding displacement errors in the sample (only small orientation errors), hence all the Ω values in the test configurations for the positioning table were set to zero.

After the test measurements were made, each manipulator was calibrated three times to assess the repeatability of the calibration procedure. In the first and second attempt the calibration measurements were made in a similar direction (the joints were moved from the lower limit to the upper limit) whereas in the last calibration attempt the measurements were reversed (the joints were moved from the upper limit to the lower limit). All three attempts used the same number of

calibration points (eleven per joint). The SPA and the standard deviation for both manipulators, following calibration, are shown below.

Manipulator		1st Attempt	2nd Attempt	3rd Attempt
Revolute manipulator	**SPA (mm)**	0.06951	0.06472	0.06784
	Std. dev. (mm)	0.02767	0.02835	0.02854
	Maximum (mm)	0.13949	0.13022	0.13665
XYZΩ Table (No rotation)	**SPA (mm)**	0.11777	0.11643	0.11820
	Std. dev. (mm)	0.05363	0.05195	0.05261
	Maximum (mm)	0.23178	0.23601	0.25132

Table 3.6: Accuracy of the revolute manipulator and positioning table kinematic models

It should also be noted that although the measurement for the positioning table were completely automated; the measurements from the revolute manipulator could not be automated due the requirement that the SMR is rotated to face the laser tracker. The rotation of the SMR was done manually which, it is considered, would introduce some additional error in some of the measured points.

3.3.6 Correcting Other Error Sources

The accuracies of both models, as shown in **Table 3.6,** are less than the previously measured repeatabilities of the manipulators. Because all three calibration attempts correlate, it can be deduced that other systematic error sources existed within the manipulators. Such additional errors could be modelled, potentially allowing further improvement to the model accuracy. An important requirement for any error source to be modelled is repeatability of the error. While CPA will determine the geometric arrangement of the joints it also makes particular assumptions, including i) perfect rotation or translation, ii) a completely rigid system and iii) a flawless motor control. These assumptions are never fully met. For example imperfections in the circularity of a joint or straightness of translation of a stage, will show up as errors in the model, unless they are also explicitly modelled. In this section three additional error sources revealed by the CPA measurements are discussed and methods for modelling two of them described.

CPA Eccentricity Errors

The back projection error is the difference between the measured positions and those calculated using the calibrated model of the manipulator. The back projection error will typically contain some measurement error, the size of which depends on the measuring device. If the back projection errors are less than the estimated accuracy of the measuring device they should be ignored. When the back projection error is computed for the second joint of the revolute manipulator, it reveals that the physical joint does not move in a perfect circle as shown in **Figure 3.7**. This error is known as an eccentricity error. Eccentricity errors are typically modelled [41] using three translational parameters $L = (L_x, L_y, L_z)$, two rotational errors $(\varepsilon_x, \varepsilon_y)$ and one angular error ε_z which are illustrated in **Figure 3.8**. During the course of rotation the axis of the joint would translate by a vector $L(\theta)$ and rotate around axis i by $\varepsilon_i(\theta)$, the values of these parameters are not constant but vary with the angle of rotation θ. With the assumption of a smooth variation, it is possible to model the change in these six parameters using a polynomial or Fourier series as described in [41]. In this implementation a single polynomial was used for each eccentricity parameter, therefore six polynomials are used for each joint deemed to have sufficient eccentricity errors.

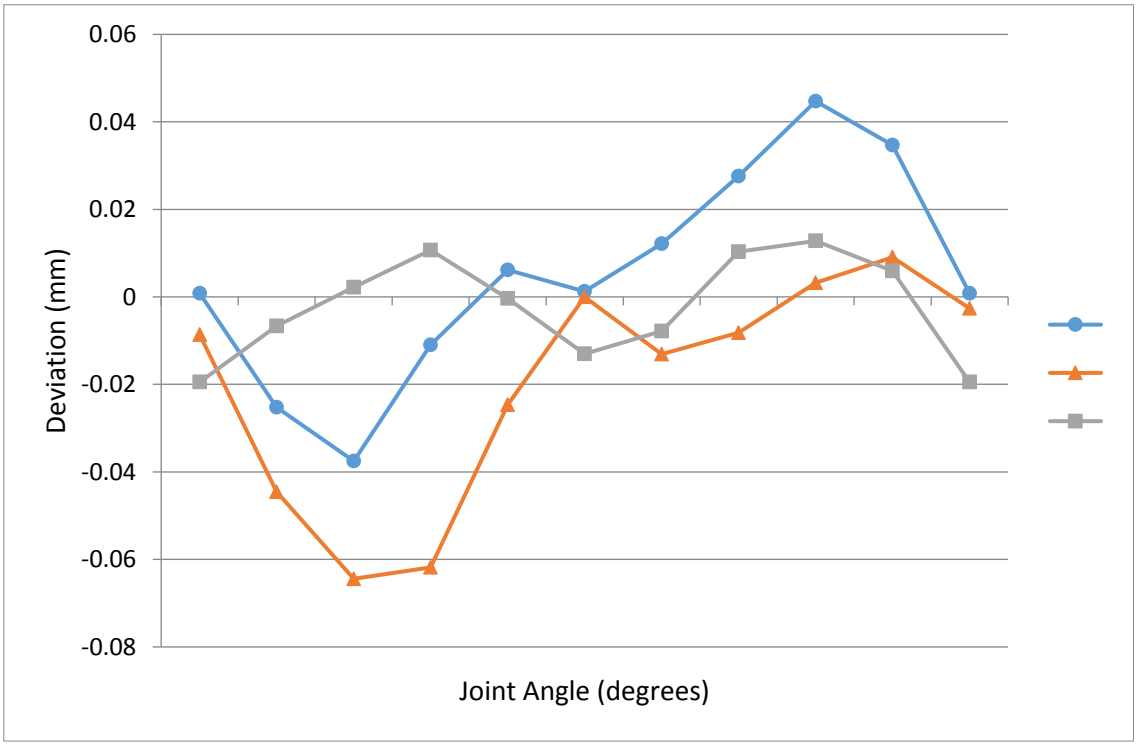

Figure 3.7: CPA back projection error of the second joint of the revolute manipulator. The deviations δx, δy and δz are computed in the coordinate system of the measuring device.

The order of the polynomials was selected empirically and the coefficients of the polynomials were determined using a non-linear minimization technique [41].

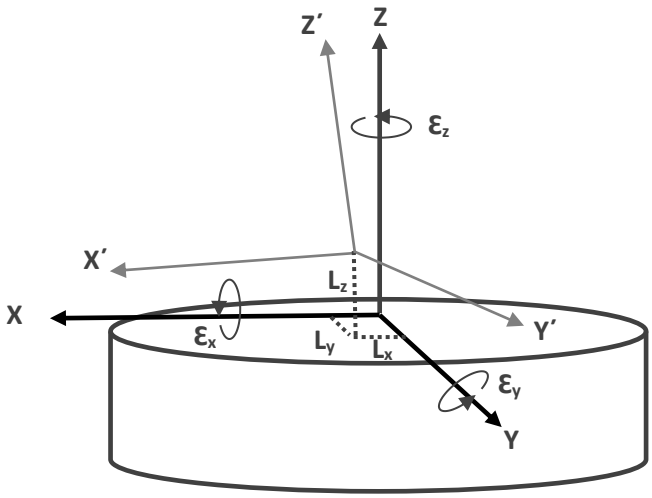

Figure 3.8: Eccentricity error of a revolute joint. The original axis **XYZ** becomes **X'Y'Z'** when the joint is rotating, the position and orientation of **X'Y'Z'** is determined by the eccentricity parameters $[L_x, L_y, L_z, \varepsilon_x, \varepsilon_y, \varepsilon_z]$ which vary with joint angle.

Incorrect Motor Offset

The back projection error for the positioning table model showed that each stage moved with offsets that varied from that requested. These offsets were found to be repeatable irrespective of the direction in which the measurements were taken. **Figure 3.9** shows the deviations of the Y-Axis for three different calibration attempts. The deviations for the X-Axis and the Z-Axis can be seen in **Appendix A**.

Figure 3.9: Deviation between commanded offset and measured offset for the Y-Axis of the positioning table.

These errors were due to a combination of incorrect motor calibration and the straightness of the axis of travel. A simple model for this error was created by assuming that the error between measured points is uniformly distributed within each offset. Correction vectors were created by considering each interval in the equally spaced CPA measurements. Errors for each interval were calculated as the difference between the measured and expected changes in position between consecutive points. The errors for each interval were stored in a lookup table enabling the correction of any position on the axis to be calculated as the sum of the errors in the lookup table from the zero position to the commanded position. The intermediate offsets are calculated by linear interpolation. Using a polynomial in place of the lookup table also performed comparably while providing a more compact representation. It should be noted that this error in particular would be present even if the user were to align the sample with another method like wall scanning and would probably have gone undetected if the positioning table had not been calibrated.

Sawtooth Errors

In the initial calibration of the positioning table published in [99], the comparison between the commanded angles of the rotation stage with measured angle, revealed errors with a perfect sawtooth profile. In a more recent calibration, the profile of the error deviated from perfect sawtooth pattern (**Figure 3.10**), probably due to repairs that had taken place between the two sets of calibrations. These errors were still repeatable, however the relationship between the commanded angle and the observed errors have not yet been determined. Although this error is important for a comprehensive system model it is insignificant in the context of strain measurement because, as described above, the gauge volume of the instrument is always located at the centre of rotation, so that the error manifests solely as a small discrepancy of sample orientation. For this reason tests of the XYZΩ kinematic model were made with the Ω stage set to zero so as to reflect the true positioning accuracy obtainable by this system in the context of stress measurement.

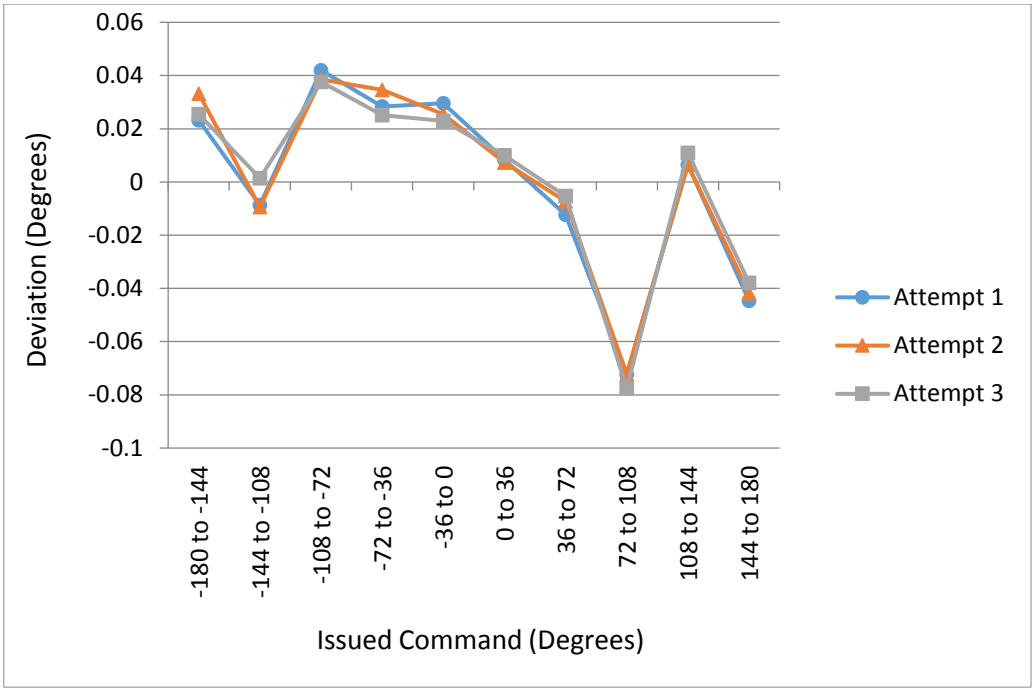

Figure 3.10: Deviation between commanded angle and measured angle of the rotation stage

3.3.7 Accuracy Evaluation of New Models

The models of the eccentricity and motor offset errors discussed above were included with the kinematic models, thereby further improving the manipulators' performance. Using the same test described in **Section 3.3.5**, the modified results are shown in the table below. The eccentricity correction resulted in an improvement of the accuracy in all attempts. Some error is expected in the eccentricity model since the polynomial would be an approximation of the actual error and the data itself contains errors from the measurement device. Since the eccentricity error is small, the model should only be applied to samples that would not significantly affect the eccentricity of the joints. For example a heavy sample might cause significant vibration in the joint that would act to increase or reduce the eccentricity errors. In such a case therefore either a modified eccentricity model should be developed or the kinematic model only should be used.

The correction of the motor offset error also led to a significant improvement in the average accuracy and standard deviation of the positioning table. Using linear interpolation to compute intermediate intervals of the motor offset error would suggest that there must be a linear variation from one error point to another. This assumption was used to reduce the number of points taken for the calibration process. It might be thought that increasing the number of calibration points would better allow us to characterise the motor offset errors and improve the accuracy. This was tested by recalibrating the positioning table with twice the initial number of points (22); the resulting accuracy improvements were minimal with an average of 0.0611mm, standard deviation of 0.0278mm, and a

maximum deviation of 0.1385mm. Further understanding of the positioning table could be achieved by an extensive mapping of each axis but due to time limitations this is left for further work.

Manipulator		1st Attempt	2nd Attempt	3rd Attempt
Revolute manipulator + Eccentricity model	**SPA (mm)**	0.05153	0.04570	0.04600
	Std. dev. (mm)	0.02542	0.02345	0.02426
	Maximum (mm)	0.11131	0.09642	0.10298
XYZΩ Table + motor offset model (No rotation)	**SPA (mm)**	0.06432	0.06238	0.06677
	Std. dev. (mm)	0.02829	0.02931	0.03008
	Maximum (mm)	0.14574	0.15667	0.17354

Table 3.7: Accuracy of the revolute manipulator and positioning table models with eccentricity and motor offset error models.

3.4 Case Study II: Huber Eulerian Cradle

In this section, another manipulator was calibrated to demonstrate the versatility of the calibration procedure. The manipulator is a Eulerian cradle designed by HUBER Diffraktionstechnik GmbH (**Figure 3.11**). The Huber Eulerian Cradle 511 consists of full circle cradle (known as the Chi Circle) and an inner joint (known as the Phi Circle). The Phi and Chi Circle planes are at right angles to one another both joints are designed to have an unrestricted 360° rotation around their axes. On the model available at ISIS, the Chi-circle has a limit switch which limits the travel range of the joint to 356°. Due to time limitation, the repeatability of the cradle was not evaluated but should be evaluated before the kinematic models are applied to a user experiment.

3.4.1 Description of Calibration

The calibration of the Eulerian cradle was performed outside the ENGIN-X instrument hutch using the laser tracker. A magnetic SMR holder was attached to the end effector of the cradle using super glue although this is not the most robust means of mounting the holder it proved rigid enough for the calibration. The holder was also mounted away from the centre of rotation of the last joint (as with the Positioning table) to ensure that the circular motion of the last joint is measurable. With every new manipulator, it may be necessary to evaluate the best placement of the SMR holder to ensure that a large part of the circle or line is measured without obstruction but this only needs to be done once if the holder is placed in the same position for subsequent calibration.

After setting up the measurement system, the calibration procedure proceeds as usual with each joint actuated individually and the measured data was used to generate calibrated models of the manipulator. As with the revolute manipulator, the Eulerian cradle breaks the DH notation requiring the modified DH notation instead of the standard notation.

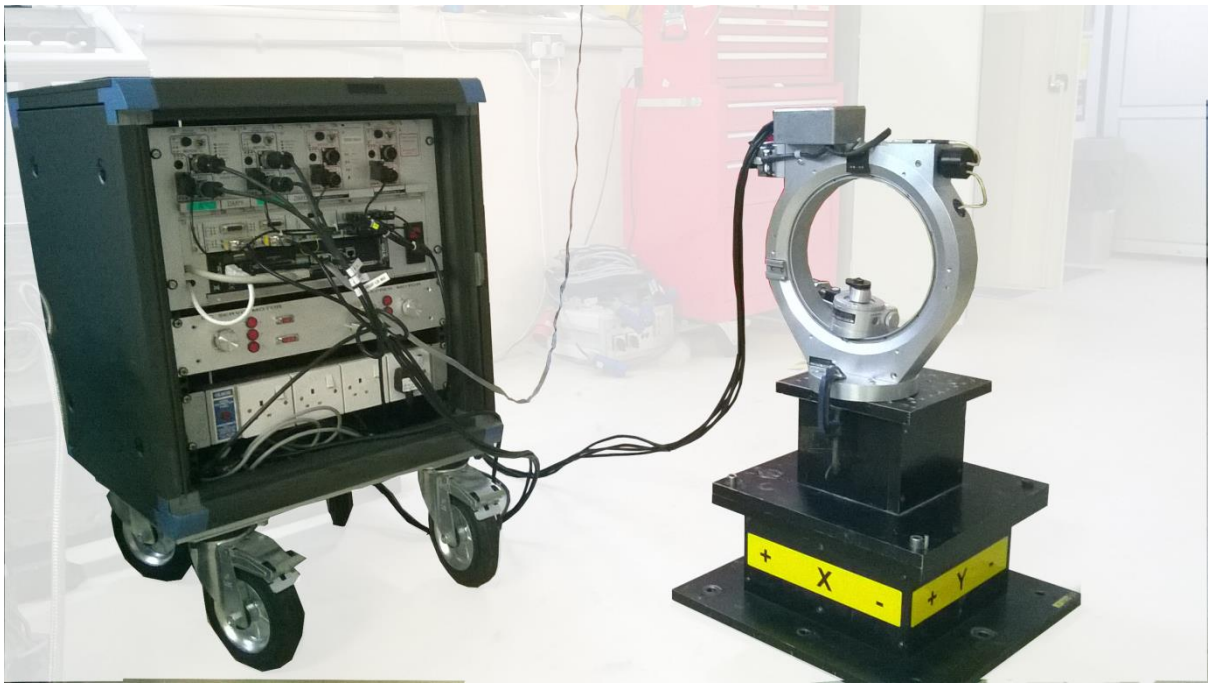

Figure 3.11: Huber Eulerian Cradle and Galil control box installed outside the ENGIN-X instrument hutch.

3.4.2 Accuracy Evaluation of Kinematic parameters

The Eulerian cradle model was tested using the method described in **Section 3.3.5**. The calibration was only performed once due to time limitations but the result nonetheless serve to demonstrate that the proposed methods are not limited to conventional robotic system but can also be applied to system with more complex designs. The cradle was tested using 52 randomly generated joint configurations and the end effector positions were measured. An average of 0.0578mm, a standard deviation of 0.0275mm, and a maximum deviation of 0.10792mm were achieved when the measured positions were compared with the computed positions from the kinematic model. The accuracy achieved from the Eulerian cradle is comparable to the accuracy achieved from the revolute manipulator after eccentricity correction has been applied. No non-linear corrections were applied to the cradle as further measurements would be needed to uncover such errors.

3.4.3 Discussion

Kinematically, the Eulerian cradle can be described by a serial chain with two links. The Eulerian cradle is designed so that the centre of rotation of joint 1 (see **Figure 3.12**) does not correspond with the physical location of the joint. This design minimizes the possibility of collisions since the workspace of the manipulator is centred on joint 1. The difference between the calibrated model and the physical robot clearly illustrate the simplicity of kinematic modelling and why kinematic modelling is insufficient for collision detection

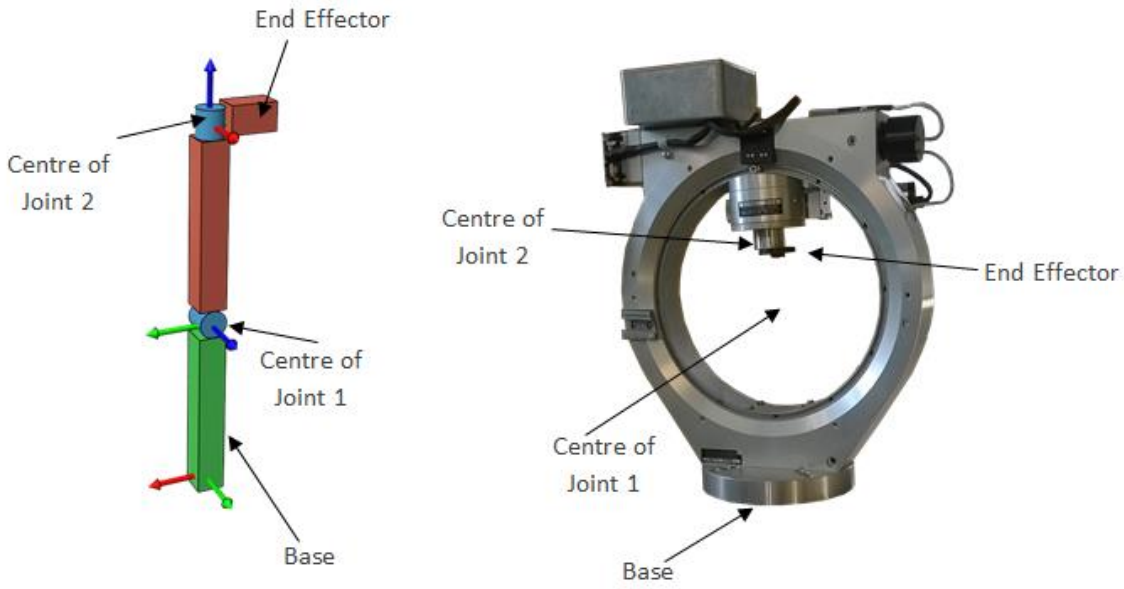

Figure 3.12: The Huber circle (Right) and its corresponding kinematic structure (Left)

During calibration, the location at which the measuring tool is mounted will affect the location of the circles which are measured and could in turn generate a slightly different set of DH parameters for the same manipulator. This needs to be accounted for when the DH parameters are also used for anything other than sample alignment. As an example, **Figure 3.13** shows the results from the calibration of the revolute manipulator with two different measuring tools denoted as Tool 1 and Tool 2. Tool 2 is longer than Tool 1 hence the circles measured by this tool are further away from the manipulator than those measured with the other tool. Irrespective of the lengths of these tools, the axes perpendicular to the measured circles should remain unchanged; however the centre of the circles would be translated differently along their respective axes. This translation would lead to different link lengths, r1 for Tool 1 and r2 for Tool 2, for the same manipulator. Theoretically, the DH parameters extracted from both tools should perform equally well when the resulting model is used for sample alignment but could fail if used for another operation such as collision prediction.

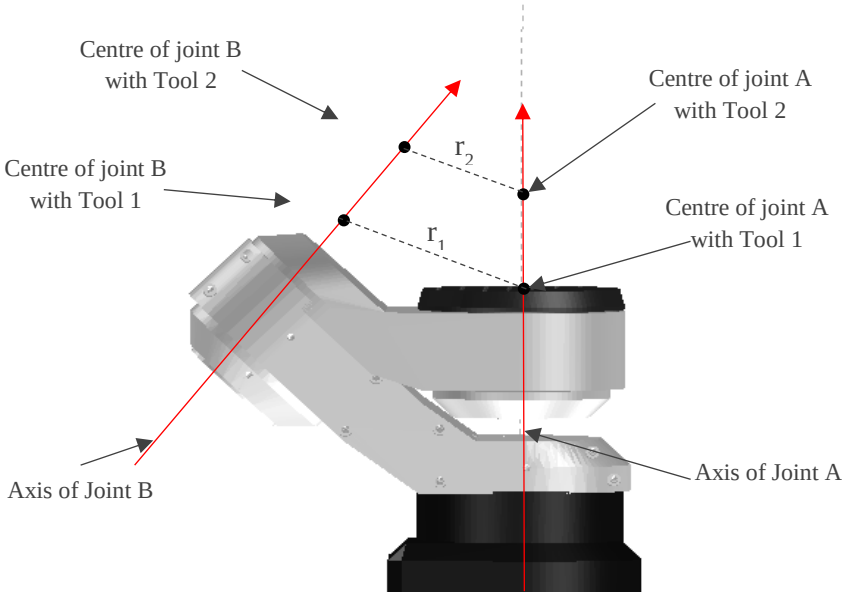

Figure 3.13: Illustration showing the effect of tool length on the extracted DH parameters.

When planning an experiment the estimated accuracy of the kinematic models should be considered. For example, if the generated kinematic model for two manipulators averaged 60mircons and 200micons respectively in the tests, with all other factors being equal the former manipulator should always be selected especially when accuracy is a priority. Both the Eulerian cradle and revolute manipulator produced similar level of accuracy in the tests therefore selecting which manipulator is used for an experiment would depend on other factors like the size and dimensions of the sample, collision avoidance, potential shadowing of the neutron beam by the hardware and required orientations as there are orientations that cannot be achieved automatically with the cradle.

3.5 Combining multiple kinematic models

As previously stated, the revolute manipulator and the Eulerian cradle are portable systems which are setup on the positioning table when required. When one of these systems, is in use it is necessary to combine its model with the model of the positioning table. The combination of both models can be seen as a problem of finding a matrix $\boldsymbol{H_{link}}$ which is the transformation from the end effector coordinate frame of the positioning table model to the coordinate frame of the first link in the portable manipulator model. Every time the portable manipulator is physically removed and re-mounted the position and orientation of the manipulator, and hence the $\boldsymbol{H_{link}}$ matrix, can potentially change.

Given a sample, with at least three fiducial points, mounted on the end effector of the portable manipulator (which is, in turn, mounted on the positioning table); the position of the fiducial points in the instrument coordinate system can be calculated, for any configuration Q, using

$$\boldsymbol{P(Q)} = {}^{\boldsymbol{W}}\boldsymbol{H}_{\boldsymbol{C_n}}.\underbrace{{}^{\boldsymbol{W}}\boldsymbol{H}_{\boldsymbol{C_n}}(\boldsymbol{0})^{\boldsymbol{I}}.{}^{\boldsymbol{W}}\boldsymbol{H}_{\boldsymbol{G_0}}}_{\boldsymbol{H_{link}}}.{}^{\boldsymbol{G_0}}\boldsymbol{H}_{\boldsymbol{G_n}}.{}^{\boldsymbol{G_n}}\boldsymbol{H}_{\boldsymbol{S}}.\boldsymbol{P(0)} \quad 3.5$$

where $\boldsymbol{P(Q)}$ and $\boldsymbol{P(0)}$ are matrices whose columns are the homogeneous coordinates $(x, y, z, 1)^{\boldsymbol{T}}$, of the calculated fiducial point positions, for an arbitrary configuration '*Q*' and the zero configuration (all joint variables set to zero) respectively. ${}^{\boldsymbol{j}}\boldsymbol{H}_{\boldsymbol{k}}$ is the homogeneous matrix transformation from coordinate frame j to coordinate frame k, $\boldsymbol{W}$ denotes the world or instrument coordinate system and $\boldsymbol{C_n}$ denotes the end effector coordinate frame of the positioning table model. $\boldsymbol{G_0}$ and $\boldsymbol{G_n}$ are the coordinate frames of the first and last links of the portable manipulator model respectively, $\boldsymbol{S}$ is the coordinate frame at the centroid of the sample fiducial points (which is also known as the tool frame) and ${}^{\boldsymbol{W}}\boldsymbol{H}_{\boldsymbol{C_n}}(\boldsymbol{0})^{\boldsymbol{I}}$ is the inverse of the transformation from the world coordinate frame to the end effector frame of the positioning table when it is in the zero configuration. ${}^{\boldsymbol{W}}\boldsymbol{H}_{\boldsymbol{C_n}}$ and ${}^{\boldsymbol{G_0}}\boldsymbol{H}_{\boldsymbol{G_n}}$ are known from the models of the positioning table and portable manipulator respectively but ${}^{\boldsymbol{W}}\boldsymbol{H}_{\boldsymbol{G_0}}$ and ${}^{\boldsymbol{G_n}}\boldsymbol{H}_{\boldsymbol{S}}$ (the base and tool matrices of the portable manipulator) are unknown. When the positioning table is in the zero configuration **Equation 3.5** may be written as

$$\boldsymbol{P(Q)} = {}^{\boldsymbol{W}}\boldsymbol{H}_{\boldsymbol{G_0}}.{}^{\boldsymbol{G_0}}\boldsymbol{H}_{\boldsymbol{G_n}}.{}^{\boldsymbol{G_n}}\boldsymbol{H}_{\boldsymbol{S}}.\boldsymbol{P(0)} \quad 3.6$$

Determining the base and tool matrices in **Equation 3.6** would allow us to compute the position and orientation of the sample when using the portable manipulator or the combined manipulator. If the portable manipulator is moved to N_Q joint configurations (where $N_Q \geq 3$) and the fiducial points are measured at each configuration, the base and tool matrix can be determined using non-linear minimization to reduce the error between the measured fiducial point positions $\boldsymbol{M}$ and those calculated using **Equation 3.6**, as shown in **Equation 3.7**. If the rotation part of the base and tool matrices were parameterized using a 3D representation e.g. Euler angles or Exponential maps, [110] then each transformation matrix could be represented with six parameters. However attempts, based on simulation, to directly minimize the cost function given by **Equation 3.7** by finding the 12 – dimensional vector v (containing the 6D representation of the base and tool matrix), were found to frequently fail to converge.

$$\min_{\boldsymbol{v}} \sum_{\boldsymbol{i=1}}^{\boldsymbol{N}} \|\boldsymbol{P_i} - \boldsymbol{M_i}\| \quad 3.7$$

Convergence was improved after consideration of the nature of the manipulator as a rigid body, i.e. if ${}^{W}H_{G_0}$ is set to the identity matrix in **Equation 3.6** then, once the correct tool matrix is known, the actual base matrix will be that rigid transform that maps the set of predicted fiducial point positions

onto the corresponding set of measured fiducial point positions. Hence the problem is reduced to that of finding the tool matrix only. This approach was applied via the following algorithm:

Let P be a set of fiducial points $\{P_i\}, \left(0 \leq i \leq N_p\right)$ attached to the sample and Q a set of robotic configurations $\{Q_i\}, \left(0 \leq i \leq N_Q\right)$. Both N_p and N_Q should be greater or equal to 3.

1. Measure the position, in the world coordinate system, of $1 < n < N_p$ fiducial points for each configuration and form the matrix *M* whose columns M_i are the (homogeneous) coordinates $(x_i, y_i, z_i, 1)^T$
2. Generate a trial tool matrix and calculate the corresponding fiducial point positions using the forward kinematics (**Equation 3.6**) with ${}^{W}H_{G_0} = I$. Form a matrix P of predicted positions corresponding to M
3. Find the homogeneous rigid transformation matrix R that provides the least square best fit mapping of P onto M using, (for example) the method proposed by Arun et al [111]
4. Calculate the cost function;

$$\mathrm{F} = \sum_i \|RP_i - M_i\|_E$$

   Where the Euclidean norm, $||P_i - M_i||_E$ is the distance between the predicted and measured positions of the fiducial point occupying the i^{th} column of the P and M matrices.
5. Repeat steps 2-4, using a suitable minimisation method to generate trial matrices
6. On convergence the trial matrix is the required tool matrix ${}^{G_n}H_S$ and R is the required base matrix ${}^{W}H_{G_0}$

In using this procedure the selected joint configurations or poses must not move the sample in a plane as planar movement does not provide enough information to uniquely determine the required base and tool matrices. A minimum of one fiducial point should be measured at each configuration, but measuring a greater number of points has been found to minimise the effect of noise and improve convergence. The algorithm does not require that the same fiducial points or even the same number of points be measured at each configuration. This flexibility allows the experimenter to measure the most convenient points close to the measuring device. As with other minimization problems, the search can be trapped in a local minimum, therefore a good guess of the starting parameter is likely to assist convergence. The accuracy of this method relies mainly on the accuracy of the calibrated model and the accuracy of the measured positions. It should be noted that the base matrix would only change when the portable manipulator has been physically moved but the tool matrix changes whenever the sample is changed in which case the new tool matrix can be recalculated using a minimum of three points measured in a single configuration. An algorithm for tool matrix re-calculation is presented in **Appendix C**.

The method presented above is one solution to the tool/flange and robot/world calibration problem in the field of robotics. Several solutions have been proposed to this problem; a proper literature review can be found in [112]. The solutions proposed can be classified as closed form or iterative. Closed form techniques tend to be faster while iterative solutions tend to give better accuracies. Closed-form solutions are typically used to initialise iterative solutions in order to provide the best possible results. Most solutions require position and orientation data while a few techniques exist that work with position data only [113]. The new technique proposed in this thesis uses multiple measurements of position data per configuration, which is a more robust approach than using a single measurement. When a single point is measured per configuration, more configurations could be required to reduce the effect of noise.

3.6 Testing the combined models and Error corrections

A practical test of the accuracy of the model of the combined revolute manipulator, positioning table and sample was performed. Six magnetic SMR holders were attached to a sample weighing approximately 4kg as shown in **Figure 3.14**. These holders serve as fiducial points on the sample and their initial positions were measured by using a laser tracker with an SMR placed in each holder. Finally the sample was rigidly mounted on the revolute manipulator and the base and tool matrices determined as described above and added to the model.

Figure 3.14: The 4kg Sample used to evaluate the accuracy of the combined model of the revolute manipulator and the positioning table. Magnetic SMR holders have been attached to serve as fiducial points

A set of 12 joint configurations were generated spanning some of the instrument workspace. Both the combined model and the physical robots were moved to each of these configurations. At each configuration, the SMR is placed on all target holders that were visible (in the line of sight of the

tracker) and those points were measured as shown in **Figure 3.15**. We compared these measured points with the points calculated by the model and the results are presented in **Table 4.1** below.

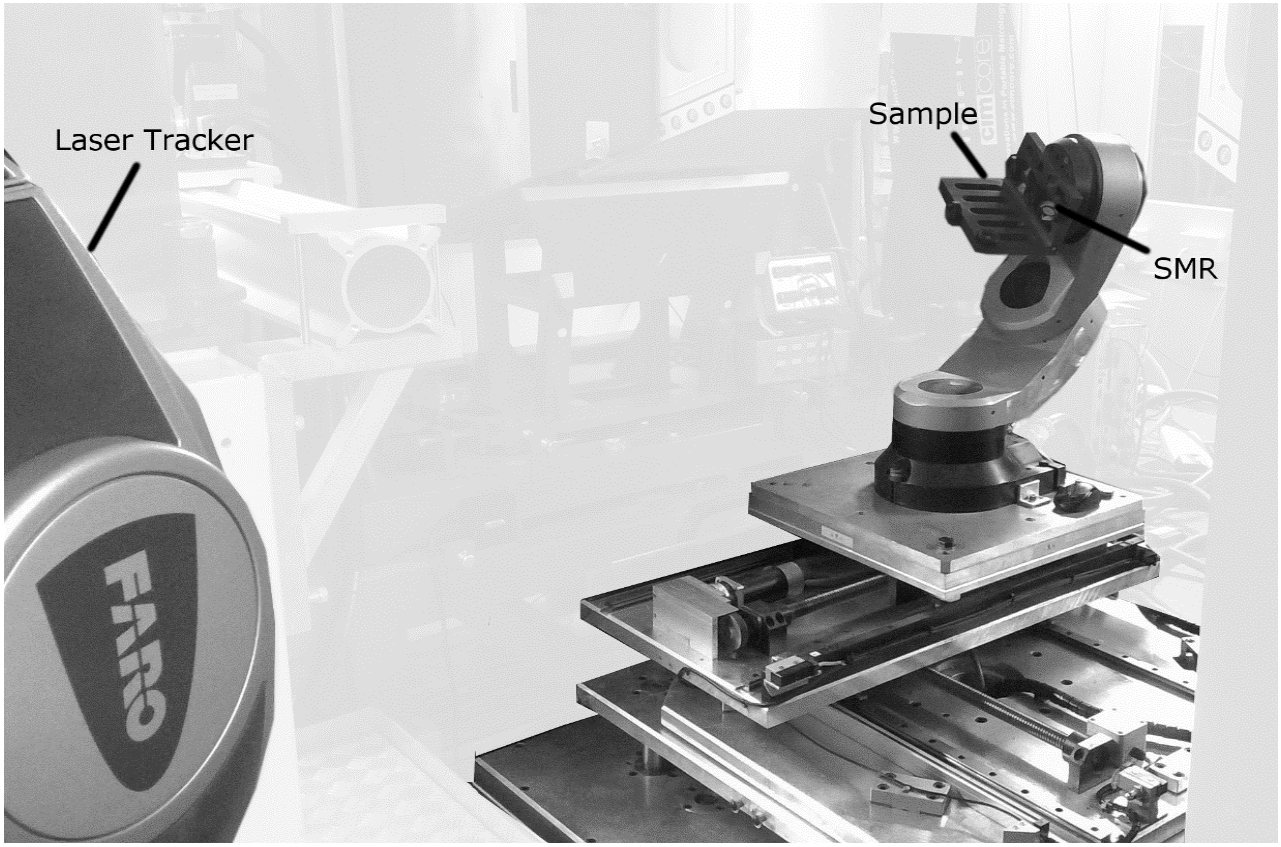

Figure 3.15: The setup used to evaluate the accuracy of the combined model. A laser tracker is partially shown on the left and the sample is mounted on the revolute manipulator.

We note that the combined system accuracy is somewhat better than the sum of the accuracies of the initial models. The mechanism whereby this occurs is under investigation but may be due to cancelation between errors in the two components of the positioning. The errors are normally distributed with the same mean and standard deviation shown in **Table 4.1**.

ID	Joint Configurations						No of visible points	Average Error (mm)	Standard Deviation (mm)	Maximum Deviation (mm)
	Z (mm)	Y (mm)	X (mm)	C (deg)	B (deg)	A (deg)				
1	10	-10	10	30	40	90	4	0.06163	0.01537	0.07544
2	30	50	-100	10	90	-40	5	0.09798	0.01875	0.11834
3	200	30	50	10	10	10	5	0.05725	0.01393	0.07643
4	250	-120	100	-10	90	180	3	0.07505	0.01696	0.09166
5	50	90	-150	25	60	18	5	0.04777	0.02245	0.07457
6	41	-60	-20	-25	18	60	5	0.09453	0.01105	0.10974
7	170	-89	70	-30	-20	-70	3	0.08401	0.01711	0.10335
8	90	-45	-136	45	-50	-30	5	0.07712	0.03106	0.12870
9	62	170	112	32	-80	-20	5	0.07413	0.05226	0.15810
10	242	143	-77	-18	50	80	3	0.10186	0.01567	0.11971
11	400	-136	95	60	180	-90	4	0.13290	0.01561	0.14621
12	300	37	-65	60	180	-90	5	0.15501	0.01928	0.18092
							All Points	**0.08807**	**0.03798**	**0.18092**

Table 3.8: Accuracy of the combination of the revolute manipulator and positioning table models with eccentricity and incorrect motor offset models

3.7 Deployment

In this section we discuss the important considerations for the deployment of the proposed system in a neutron diffractometer.

How often should I calibrate?

A complete calibration[14] of the ENGIN-X positioning table takes approximately two hours. The reader is reminded that the calibration of the rotation stage could not be automated due to the absence of a motorized SMR. Full automation of the measurements would only slightly reduce the time taken since currently only the rotation stage needs to be done manually. Calibration without test measurements would reduce the duration of calibration to about 40 minutes, but it is not recommended to perform a calibration without proper testing. The duration of the calibration procedure suggests that a complete calibration should not be performed at the start of a user experiment.

[14] A complete calibration includes the 100 random test measurements used to evaluate the quality of the calibration.

The kinematic structure of any rigid positioning system is not expected to change frequently except when some modification has been made to the system. The system should be recalibrated after any hardware damage is repaired or after any maintenance where the system is deconstructed. Damage to external controllers should not warrant the recalibration of the whole positioning system unless the system is deconstructed also. The constant usage of the positioning system would lead to wear and tear which could require recalibration even in the absence of any damage or maintenance. Such routine calibration could be performed at the beginning of a measurement cycle or on a yearly basis depending on the age of the system. The non-kinematic calibration for errors such as the motor offset errors found in the ENGIN-X positioning system would require more consideration as the source of the errors was not completely structural. Some modifications to the controller software were found to re-arrange the measured motor offsets. Dynamic errors are typically affected by the mass of sample so a significantly large sample could cause the errors to change although this was not tested. Recalibration for the dynamic error should be determined on an experiment basis, a simple one joint test could reveal if a new calibration is necessary.

Who should do the calibration?

In the best case scenario, the calibration process should be completely autonomous and the observer could intervene if necessary. In the absence of full automation, the selection of personnel for the calibration would depend mainly on the measurement device, if significant training is required before using the measurement device, to get the best accuracy it might be better for a trained person such as an instrument scientist to perform the calibration. Other practical considerations like safety of the instrument should also be examined, for example if collimators are mounted during the calibration process, an untrained personnel could cause a collision while trying to follow the calibration instructions.

4 Monitoring the Instrument

After planning an experiment, it is still possible that the planned motion can deviate from the actual motion during the experiment. Failure of the positioning system could lead to a misalignment of the sample. This could lead to wasted beam time if the misalignment is discovered or erroneous results if not discovered. For example, during a user cycle at ENGIN-X, it was reported by some users that the ENGIN-X positioning table would rotate the sample when not commanded; such types of failures could slip by a non-observant user and end up as published results. Positioner failures could be present irrespective of the alignment technique (wall scans or simulations). Some other failures are unique to model based alignment techniques, for example, kinematic models might deviate from the actual hardware when the system is repaired or when parts are replaced, so an experiment planned completely offline could be incorrect when applied in the real world. With these problems in mind, the question addressed in this chapter is to find out how the position of the sample, and potentially, any other hardware items can be monitored so as to ensure correspondence to the experiment plan.

4.1 Methodology

In this chapter, a fiducial based metrology system is proposed. Fiducial markers are placed on positions on the sample, jaws or any other part of the instrument. These fiducial markers would be monitored throughout the experiment and the feedback from the metrology system could be used to confirm that the instrument including the sample behaved as expected. The feedback system could also be used to correct the sample if it is found to be in the wrong position or just notify the user of the situation.

4.2 Proposed Metrology System

The next section discusses some of the important considerations for the development of a metrology system for a neutron diffractometer.

4.2.1 Medium of Interaction

As discussed in **Section 2.5.1**, several mediums of interaction are used by 3D measuring devices, some of which are not conducive for use during a neutron diffraction experiment. We will now discuss the various possibilities and select the best for the neutron diffractometer.

1. Mechanical systems: These systems measure the position of an object by having a mechanical linkage or fixture attached to the sample. The major challenge with mechanical linkage is the possibility that they might interfere with the experiment. If the linkages are made of a material

that diffracts neutrons the system could contribute error to the measurements. Mechanical systems have the potential to be the most accurate but would require essential and probably expensive redesign to be used on a diffractometer.

2. Acoustic systems: The challenge with acoustic systems is that they are susceptible to external noise hence they are mostly used underwater or for short range measurements. Some neutron diffractometer environments contain noise generating equipment from fans to UPS systems some of which emit noise in the ultrasound range. Therefore to have a more reliable system, acoustic systems should be avoided.
3. Magnetic systems: These systems are capable of providing reasonable accuracy at excellent range but they have the disadvantage of being distorted by metallic objects in their workspace. Magnetic systems are robust to occlusions i.e. they do not require line of sight to the target but the previously mentioned limitation overshadows the benefit of magnetic systems.
4. Inertia Systems: Although not discussed in the literature review, inertia systems are not popular for high accuracy metrology because they tend to drift over a period of time. Inertia systems typically provide accuracies in the millimetre range which would be insufficient for this project.
5. Optical System: Optical systems are popular in motion capture and robotics research. They provide excellent accuracy and a myriad of commercial products are available. They have the disadvantage of requiring a line of sight to the object being measured. Although these systems might require markers mounted on the sample, they are otherwise unobtrusive and do not interfere with the experiment. They could be grouped into laser-based systems and camera-based systems.

From the discussion above, it can be seen that the best option for monitoring experiment on a neutron diffractometer with minimal interference would be achieved using an optical system. The decision between a laser-based system and camera-based system is open to choice. In this project, a camera-based system is developed for the reasons presented in the next section

Laser Vs Camera

Both laser-based systems and camera-based systems could provide sufficient accuracy for neutron diffraction monitoring. Several commercial systems in both categories exist which promise accuracies of 0.1mm or better. Other considerations that affect the choice of system are:

1. Cost: laser-based systems are typically more expensive than camera-based systems. Monitoring using for example a laser tracker would require the purchase of multiple SMR targets which could cost around £1000 each, and still require the purchase of target holders. The cost of markers for a camera system would be significantly cheaper.

2. Speed: Camera based systems can measure several targets at the same time and do not need to wait for stability of the medium of interaction. Laser systems would typically measure a single target at a time and need to wait for stability of the laser before each measurement. Speed is beneficial to ensure that the system does not interfere with the time required for the experiment.

4.2.2 Static Metrology or Dynamic Tracking?

The metrology system could be designed to make static measurement only or to dynamically track the sample as it moves from one pose to the next. During stress measurements on a neutron diffractometer, the whole instrument is typically kept stable. Stress measurements are typically not concerned with the path that the sample takes between measurements except in instances when the system is being used to check that paths are collision-free. Therefore in this work, the focus is on static metrology. The extension to dynamic tracking should be relatively straightforward once the static system is developed

4.3 Camera based Metrology System

The proposed system is similar to those used in the motion capture industry. These systems use a set of cameras to monitor the positions of fiducial markers placed on the object. Several types of markers have been proposed for such systems [114]. In this project, retroreflective markers will be used because these markers can be detected easily using an external light source. Retroreflective markers are typically designed in one of two forms: flat circular or spherical targets. Spherical targets have the benefit that their 3D location can be verified using a non-camera based metrology device such as a touch probe. When multiple retroreflective markers are attached to the object being monitored as shown in **Figure 4.1** then each marker or cluster of markers can be monitored independently.

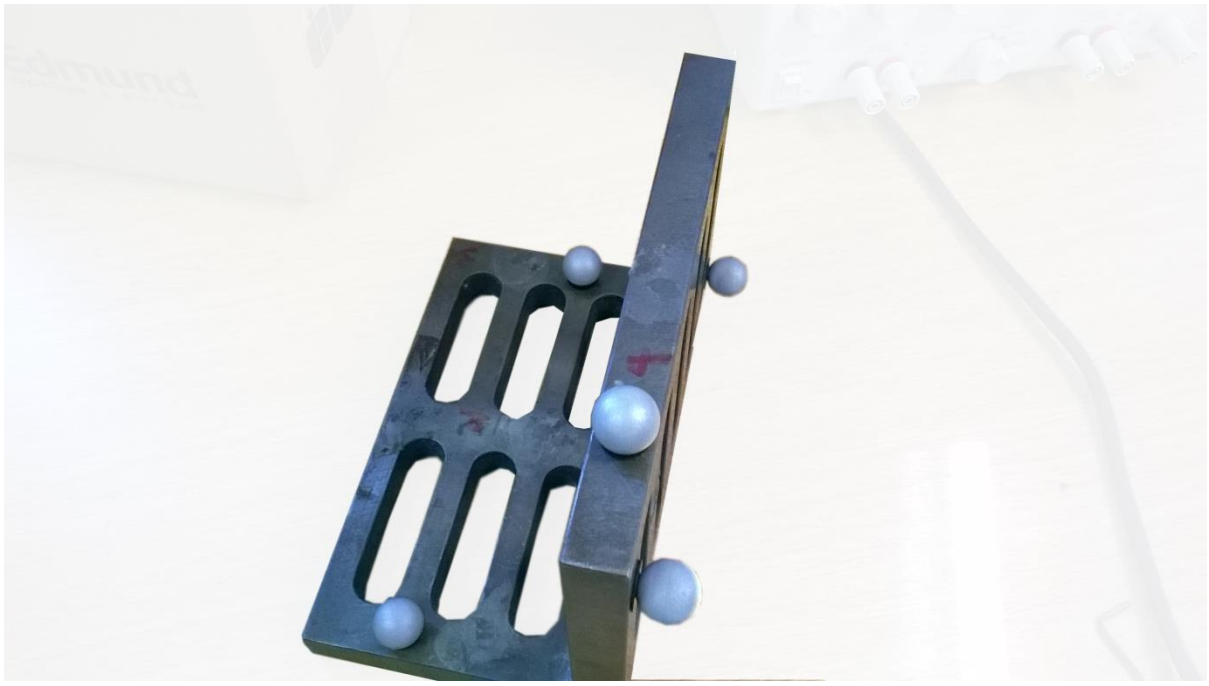

Figure 4.1: Multiple retroreflective spherical markers attached to a sample

Although commercial camera metrology systems are available from a variety of manufacturers; the system proposed in this project would be a custom built system. A custom built system has the following advantages:

- The system can be optimised for the specific instrument, for example, the field of view of the system could be optimised to cover as much of the instrument as desired, the measurement range of the device could be optimised to suit the instruments, and control software could be integrated into the instrument software etc.
- The cost of the camera system can be reduced when most of the system is built in house.

The essential question that needs to be answered is that of achievable accuracy. The accuracy of camera metrology systems is mainly dependent on the quality of the camera, lens and proper calibration. The calibration of the developed system is discussed in **Section 4.4**. After calibration, the proposed system follows the pipeline presented in **Figure 4.2** each stage of the pipeline is discussed in details in the following sections

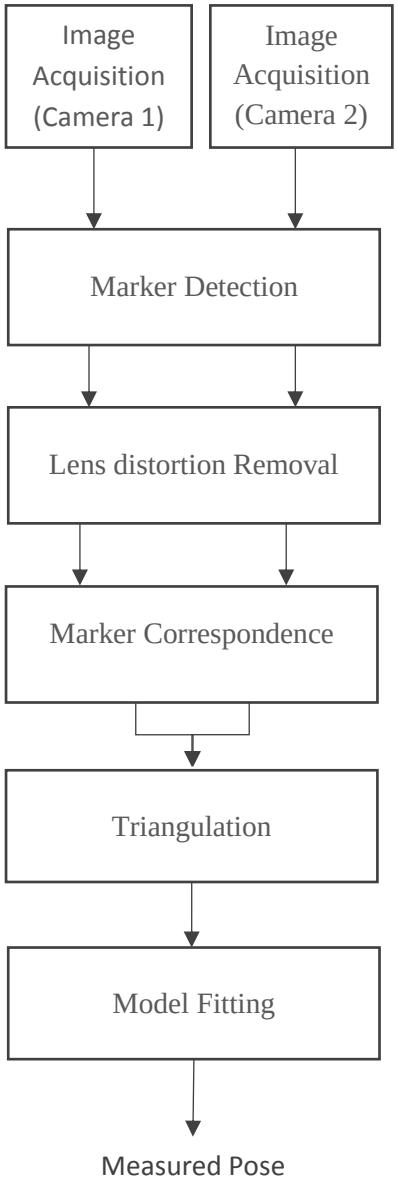

Figure 4.2: The pipeline for the proposed camera based metrology system

4.3.1 Image Acquisition

The image acquisition system evolved through several iterations before arriving at the current system. The first iteration was the use of the CCTV cameras (**Figure 4.3a**) which had been mounted in the instrument hutch to capture video and pictures of the sample environment for the users. The system provided a compact package with an inbuilt infrared mode and also a C++ SDK. The infrared mode could only be triggered by a light sensor, so the light sensor had to be covered with tape in order to switch on the infrared lights. These cameras process the raw images and output a compressed JPEG file; no means of accessing the raw images was found. The proposed camera based metrology system was developed ignoring these limitations of the CCTV cameras. The test of

the CCTV system showed that reasonable accuracy is achievable from such a system. The CCTV system initially performed poorly which was possibly due to sensor noise and the on-board image processing. Also a plastic dome protecting the CCTV camera was found to be distorting the images. After removing the plastic dome, the system typically achieved an average accuracy of 1.239mm, with a standard deviation of 2.040mm, and maximum error was 8.140mm when tested over 150 fiducial marker positions. With manual outlier removal, the best accuracy achieved for the CCTV system was an average of 0.093mm, a standard deviation of 0.053mm, and maximum error of 0.254mm over 118 fiducial marker positions. Since manual outlier removal would not be convenient for the proposed system, it was necessary to find a camera with less noise and no inbuilt image processing. These requirements led to the purchase of a pair of Basler Ace machine vision cameras, see **Appendix B** for specification (**Figure 4.3b**) which allowed access to the raw images and contained less noise. Both cameras were fitted with near infrared (850nm wavelength) ring lights which were acquired as CCTV replacement parts (**Figure 4.3c**) and connected to a variable power supply. Several lenses were tested during the development of the camera system:

- 4mm CCTV lens: These were inexpensive lenses which provided a good field of view of the instrument and reasonable image quality (see **Figure 4.3e**), however they caused a flaring effect on the image of the retroreflector which made them unusable for this system. The flaring effect was considered to be due to poor anti-glare coatings on the lenses.
- 12mm-24mm varifocal lens: These lenses are usually used for Digital Image Correlation (DIC) techniques on the instrument. These lenses provide excellent image quality with little distortion but only a small field of view at the distances available within the instrument hutch (see **Figure 4.3d**).
- 3.5mm Navitar lens: These are wide angle, 3.5mm fixed focal length lenses with large field of view that covered most of instrument at the distances available (see **Figure 4.3c**). These lenses had more distortion than the DIC lenses but still provided good image quality.

The current image acquisition system is composed of two Basler Ace cameras equipped with Navitar lenses described above. The infrared ring lights were replaced with a pair of white LED ring lights (Figure 4.3g) which performed better than the former in all tests. The image capture is performed via the Basler Pylon SDK. The SDK allows several camera settings such as the exposure time to be managed from code. The SDK is available in .net, C and C++ programming languages. The C++ SDK was chosen as the language for this work. Typically the sample and the instrument are static prior to any neutron measurements therefore no attention has been paid to the synchronization of the two cameras. Synchronization of the cameras needs to be addressed if the system is to be used for dynamic tracking of samples.

(a) **(b)**

(c) **(d)**

(e) **(f)** **(g)**

Figure 4.3: The components that were tested in the camera metrology system **(a)** CCTV camera system **(b)** Basler Ace acA1920-25um **(c)** CCTV replacement infrared ring light **(d)** 12mm-24mm varifocal lens **(e)** CCTV replacement 4mm fixed focal length lens **(f)** 3.5mm Navitar fixed focal length lens **(g)** Neewer 48 Marco LED Ring Light

A camera mounting rig was fabricated[15] using an 825mm long aluminium rail with two camera stands for the cameras. The aluminium rail allowed the baseline between the cameras to be adjusted when necessary and a locking screw is available to rigidly hold each stand. The camera stands were designed with a ball-socket joint so that the camera could be panned or tilted to the appropriate orientation. A locking screw is also present on the camera stand to rigidly hold the orientation of the camera. The whole rig was mounted above the ENGIN-X beam guide using adhesives as shown in **Figure 4.4**. The current stereo camera system hardware cost about £1000 and more cameras could be added to improve accuracy and ensure robustness.

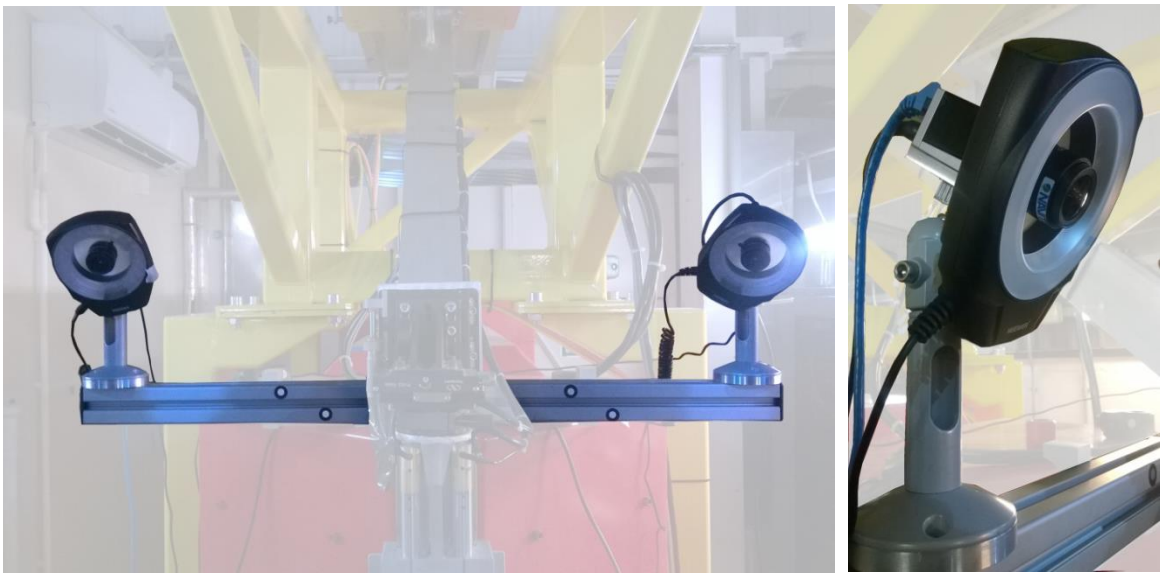

Figure 4.4: The current design of the camera metrology system and mounting rig (left) with a closer view of a single camera stand (right). The rig is mounted on the ENGIN-X beam stop behind the jaws.

4.3.2 Marker Detection

Marker detection is crucial to the accuracy of the monitoring system. The spherical marker must be segmented from the image accurately prior to the centre of the sphere being determined. For easy segmentation, the markers should appear as bright regions (blobs) surrounded by a near black background. The segmentation of the markers is simplified by the retroreflective nature of the markers since they reflect light back in the direction of the light source, thus increasing the contrast between marker and background. Better contrast of the markers can be achieved by modifying one of the following:

- **Brightness of the ring lights**: increasing the brightness of the ring lights, increases the brightness of the retroreflective markers in the image.

[15] The design and fabrication of the mounting rig was done by the ISIS mechanical support group

- **Exposure count time**: Decreasing the count time for each image exposure decreases the brightness of the image. Larger count times are typically used to improve the signal to noise ratio therefore decreasing the count time could have the unintended effect of increasing the noise.
- **Aperture Size**: Decreasing the aperture of the lens, increases the depth of field of the camera while simultaneously reducing the amount of the light in the image. Decreasing the aperture size could cause diffraction of the light when the size is below a certain limit which can be calculated using the wavelength of the light used and the diameter of the aperture.

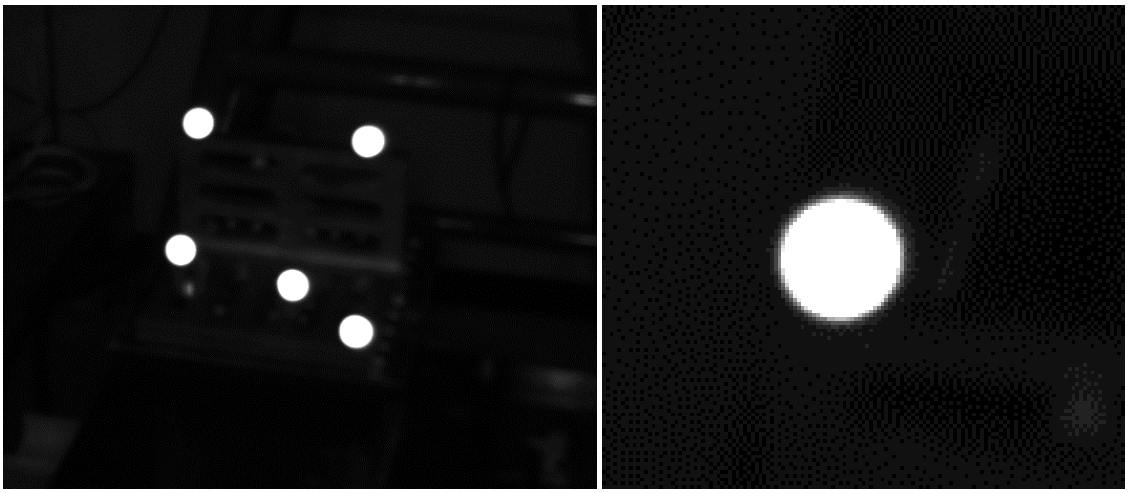

(a) **(b)**

Figure 4.5: An image from the camera system of a set of fiducial markers mounted on a sample **(a)** crop of the whole sample **(b)** crop of a single fiducial marker.

Essentially the parameters above must be optimised to get the best accuracy for the available hardware. Achieving the right contrast should produce an image of blobs such as shown in **Figure 4.5**. Such images may also contain outliers so an appropriate blob detection technique is required. On the proposed system, the best accuracy was achieved when the aperture was fully opened (which corresponds to an f-number[16] of 1.4) and the exposure time was set to 15000 microseconds which is about half the default time. The brightness of the ring light could not be controlled.

Blob detection

Blob detection consists of three stages in the first stage potential markers candidates are segmented using thresholding. The threshold value for each camera is selected empirically.

$$segmented\ Image = \begin{cases} F(i,j) & if\ F(i,j)\ > threshold \\ 0 & otherwise \end{cases} \quad 4.1$$

[16]The f-number is the ratio of the lens's focal length to the diameter of the aperture.

The output from the thresholding stage is an image containing the marker candidates against a black background. The marker candidates are extracted from the image by locating all the clusters of non-background pixels (non-black pixel). The extracted marker candidates are validated to remove outliers and noisy markers. The validation is done by checking the circularity, aspect ratio and area of the extracted marker candidates, if a marker candidate falls outside the pre-selected range for any of the above properties it is discarded.

The circularity property of the blob checks how close the segmented region is to a circle i.e. a perfect circle would have a circularity of 1. The correct markers would not be a perfect circle but an ellipse [115] due to perspective projection and lens distortion. With a low distortion lens, it is possible to achieve circularity close to 1. The formula used for computing the circularity of a blob is given below where A is the area of the blob and P is the perimeter.

$$Circularity = \frac{4\pi A}{P^2} \tag{4.2}$$

The aspect ratio property basically evaluates the ratio between the major axis and the minor axis of the blob while the area property checks the number of pixels in the blob, this value would vary as the blob moves away from the camera but should be selected so that the unrealistically small or large blob candidates are discarded. All marker candidates that pass all the property tests are assumed to be valid markers. The next step is to determine the projected centre of the markers with sub-pixel accuracy.

Sphere Centre Detection

Several methods have been proposed for centre determination [89]. Both the ellipse fitting and the grayscale centroiding method were implemented in this work with the latter outperforming the former in all tests.

- **Grayscale centroiding**: is a simple centroid operation in which the grayscale values are used as weights as shown in **Equation 4.3** where $(\bar{u}, \bar{v})$ is the centroid point, $F(i,j)$ is the grayscale value of the pixel at location (i,j), m is the image width, and n is the image height. When using this method, it is assumed that the brightest spot on the marker should be the centre of the sphere as surface normal at that point should be perpendicular to the camera (and the light source).

$$\bar{u} = \frac{\sum_{j=1}^{n}\sum_{i=1}^{m} iF(i,j)}{\sum_{j=1}^{n}\sum_{i=1}^{m} F(i,j)} \qquad \bar{v} = \frac{\sum_{j=1}^{n}\sum_{i=1}^{m} jF(i,j)}{\sum_{j=1}^{n}\sum_{i=1}^{m} F(i,j)} \tag{4.3}$$

  Grayscale centroiding is sensitive to non-uniform illumination, dirt or any sort of noise that affects the grayscale values. Further weighting of the centroid operation so that contribution of the brighter pixels in the equation above is increased has been found to improve the accuracy of the centre detection [116]. This extra weighting is achieved by using the square of the grayscale

values. Both the grayscale centroiding and the squared grayscale centroiding were tested and the squared grayscale centroiding performed better in the accuracy tests.

- **Ellipse fitting**: In this method, the contour of the blob is extracted and an ellipse is fitted to the extracted contour. The centre of the fitted ellipse is the projected centre of the sphere. Since the contour of the marker is discretized into integer-valued locations or pixels, the extracted contour has been found to not provide sufficient accuracy. One way of achieving better accuracy is to determine the contour to floating-point or sub-pixel accuracy then fit the ellipse to the sub-pixel contour. Several sub-pixel edge detection algorithms have been developed; this work used an open source implementation [117] based on Steger's algorithm [118]. Contour based methods are sensitive to noise due to incomplete contours or extra pixels in the contour therefore to avoid using poorly segmented or incomplete markers, the error for the ellipse fit was computed and any marker above a selected threshold discarded.

After locating the markers from the two camera images, the next step is to remove lens distortion from the segmented markers.

4.3.3 Lens Distortion Removal

Before the correspondence between markers can be found, it is essential that the distortion introduced by the lens be removed. The removal of the lens distortion could also be done before the marker detection stage. The major benefit of performing the lens distortion after the marker detection stage is speed, since the distortion removal would then only need to be performed on a small number of points (the calculated centres) as opposed to it being performed on every pixel in the image.

The standard models for lens distortion (**Section 2.6.2**) are not invertible therefore the distortion is typically removed using a minimization technique or an approximation of the inverse. In this work, the undistort function in OpenCV Library [119] was used.

4.3.4 Marker Correspondence

The marker correspondence problem is to find the corresponding points from the point sets from both cameras. The problem is complicated by the homogeneity of the markers used in the system i.e. markers cannot be visually differentiated from each other. There could also exist points that have no correspondence either due to occlusion or because such points are outliers, therefore a robust algorithm is required for determining marker correspondence.

Several methods have been proposed for matching points in multiple cameras. The most common is the Epipolar line method. In **Section 2.6.4**, the Fundamental matrix is used to locate the line in the

second camera on which to search for correspondences, as shown in **Figure 2.19**. Chen et al [120] proposed the 3D space intersection method which is analogous to the Epipolar line method but uses the camera triangulation error instead. Both methods would perform similarly as they both have similar uncertainty [120].

Epipolar line method

The Epipolar constraint between the corresponding 2D points $\boldsymbol{m_1}$ and $\boldsymbol{m_2}$ is given in **Equation 2.35**. In practice, the result from that equation would not be zero but would be within some tolerance as shown in **Equation 4.4**. This equation returns the distance between point $\boldsymbol{m_2}$ and the epipolar line corresponding to $\boldsymbol{m_1}$. This relationship can be exploited to find the correspondences between two point sets.

$$\|\boldsymbol{m}_2 F \boldsymbol{m}_1{}^T\| < tolerance \tag{4.4}$$

Given a set of m 2D points from the first camera and a set of n 2D points from the second camera; a cost matrix $\boldsymbol{C}$ with m rows and n columns can be created. Each element $\boldsymbol{C}_{ij}$ of the cost matrix would be the result from the left-hand side of **Equation 4.4** for the i^{th} point from the first camera and the j^{th} point from the second camera. The cost matrix contains a pair-wise comparison between points in the first and second camera. With this matrix, the problem of finding the correspondence becomes an assignment problem which is to find the correspondences that result in the minimum total cost. A popular method of solving the assignment method is to use the Hungarian algorithm [121] which is used in this thesis.

The correspondence algorithm should perform correctly when the assignments are unique and there are no outliers in both point sets. In a situation where a point with no correspondence exists, an outlier could be assigned to such a point irrespective of the magnitude of the distance between the point and the outlier. Therefore it is important to check that the cost for each assignment does not exceed the pre-selected tolerance, any assignment that exceeds the tolerance should be discarded as an outlier or a wrongly assigned point.

With the epipolar line method, an ambiguity exists when multiple points in the second camera have the same distance to the epipolar line corresponding to a point in the first camera. In this case, it becomes non-trivial to find a proper match. The simplest and fastest solution is to discard any row and column in the cost matrix where more than one cost value is below the selected tolerance then find the assignment for the remaining points. A minimum of three points are required to determine the pose of the sample when the minimum is not reached. Some heuristics could be used to find more correspondences, for example when both cameras are facing the same direction, the order of the point might be preserved i.e. the leftmost point in the first camera should typically correspond to the leftmost point in the second camera. It is also possible to use a third camera to resolve

ambiguities between the first and second camera. The epipolar method has been implemented for the camera system described above (see **Figure 4.6**).

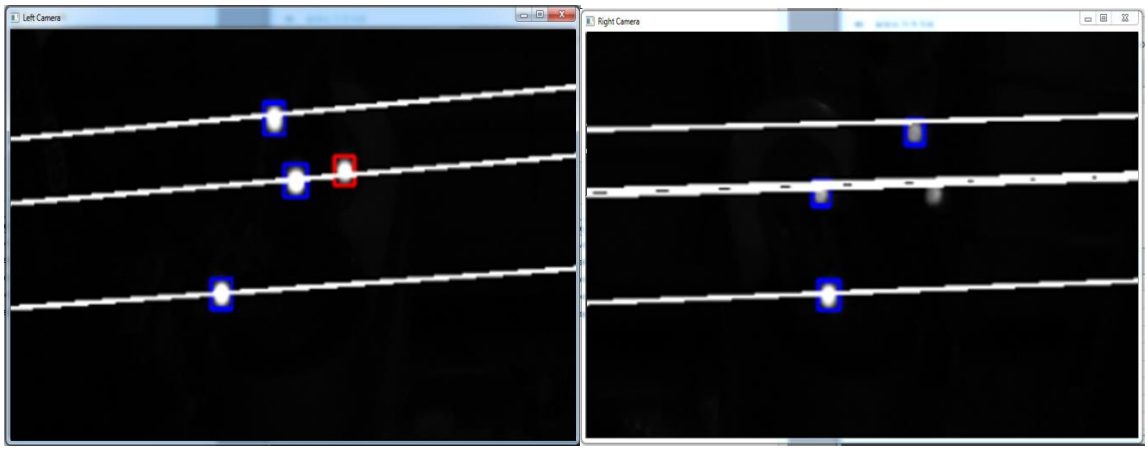

Figure 4.6: A screenshot of the GUI of the camera system showing the left and right camera images. The blue squares highlight fiducial markers whose corresponding marker in the second camera is found. The red squares highlight markers for which no correspondence is found. The white lines are the Epipolar lines.

Another interesting method of resolving the correspondence ambiguities (which is applicable when simulation software is used for the sample alignment) would be to use simulated position data to resolve the ambiguity. If the simulation software is used to estimate the positions of the fiducial markers on the sample, these estimated fiducial positions can be projected into a virtual camera image using the camera model for each camera. Although the virtual image would not be a perfect match with the real image; with calibrated kinematic models, the virtual image should be good enough to determine the correspondences in both cameras. This method simultaneously finds the correspondence between image points in the first and second camera and the correspondence between the fiducial points and the image points which usually has to be found via another method. It is hoped that this approach, which to the author's best knowledge is novel, will be tested in the future.

4.3.5 Triangulation

After marker correspondences are found from both cameras, the points are used to reconstruct the 3D points using the linear least square triangulation method discussed in **Section 2.6.5**. Several methods have been proposed to improve upon the linear least square triangulation method such as the optimal triangulation methods which attempt to adjust the image points from both cameras so as to minimise the error from **Equation 4.4** following which triangulation is performed with these

new points. The optimal triangulation technique proposed by Kanatani [122] was evaluated in the proposed system but provided no improvements to the system accuracy in all performed tests.

4.3.6 Model Fitting

Determining the pose of the sample, jaws or any other part of the instrument being monitored requires the correspondence between the known fiducial point set and the triangulated point set. Let P be a set of fiducial points $\{P_i\}, \left(0 \leq i \leq N_p\right)$ attached to the sample (or other parts of the instrument) and Q be the 3D points from the triangulation stage of pipeline described above. Both N_p and N_Q should be greater or equal to 3. N_Q would typically be smaller than N_P because all the points might not be visible to the cameras. Q could also contain some outliers therefore a robust algorithm is required to find the correspondence between P and Q

A common method for finding the correspondence between the two sets of 3D points is to compare the distances between points in both sets. If d_P^{ij} is the distance between point i and j in point set P and d_Q^{ij} is the distance between point i and j in point set Q. The magnitude of the difference between d_P^{ij} and d_Q^{ij} should be less than a pre-determined tolerance i.e. $\left\|d_P^{ij} - d_Q^{ij}\right\| < tolerance$, if the i^{th} and j^{th} points in P corresponds to the i^{th} and j^{th} points in Q. If the distances between the points in the model are unique, all the correspondences between P and Q can be determined by comparing the distances from both sets, otherwise some ambiguity would exist. If at least three correspondences are found, the pose is determined using the method proposed by Arun et al [111]. Any other ambiguity from this method can be resolved by evaluating the error from the pose computation.

4.4 Camera Calibration

The preceding sections described the pipeline used by the camera system to measure 3D position from images. The lens distortion removal, marker correspondence, and triangulation stages require a calibrated camera system if high accuracy is to be achieved. The pinhole model presented in **Section 2.6.1** was used in the developed camera system. Both radial and tangential distortions were modelled while thin prism distortion was found to be negligible therefore it was removed from the camera model. The 4th and 6th order radial distortion terms were also removed since their effect was also found to be negligible also. These simplifications reduced the distortion parameters that were required to be found to (k_1, p_1, p_2). The camera model used consists of 4 intrinsic and 6 extrinsic parameters with the skew set to zero.

After selecting the camera modelling parameters, typically a set of measurements would be made to determine the values of the model. As explained in **Section 2.6.3**, these measurements could be

made in a variety of ways. When developing the measurement procedure for the ENGIN-X camera system, the following were taken into consideration:

- Zhang [82] recommended that calibration be performed with a three dimensional apparatus when the highest accuracy is required.
- Some off-the-shelf systems require the user to place a calibration apparatus at pre-programmed locations which could be unreachable on the ENGIN-X instrument due to the small workspace of the instrument and possibility of collision.

With these in mind, the proposed measurement procedure utilises a three dimensional grid of fiducial markers which can be modified to cover the available workspace without a human operator thereby avoiding collisions or the possibility of someone stepping on the positioning system or otherwise interfering with the instrument hardware. In this procedure, the positioning table of the instrument is used to construct a three dimensional grid of fiducial sphere positions. The laser tracker described in **Section 3.2.2** was used to track the actual position of the table to avoid including positioning table errors in the camera calibration. The architecture presented in **Section 3.3.1** is used to facilitate communication between laser tracker and positioning system which means human intervention was avoided during the camera calibration. The calibration measurement procedure is as follows

- A single fiducial sphere is mounted rigidly on the positioning table. The positioning table is commanded to move in a grid pattern.
- At each position in the grid, the camera is commanded to capture the image of the fiducial targets and the laser tracker is commanded to measure the 3D location of the table.
- The 2D centre of the fiducial marker is extracted from the captured images using the techniques already discussed in **Section 4.3.2**.
- The laser tracker measurements are assumed to follow the same motion as the centre of the fiducial marker. However because the tracker follows an adjacent SMR rather than the fiducial sphere these measurements do not correspond to the actual centre of the fiducial sphere. However, these errors result in a translated camera coordinate frame.
- Finally, the centre of the fiducial sphere should be aligned with the centre of the instrument's gauge volume. The measurement made at this position can be used to fix the coordinate frame after calibration.

Using the positioning table to construct the positioning grid implies that the number of points can be increased to give better statistics or reduced when faster calibration is required. Testing is necessary to determine the best number of points that optimise the trade-off between speed and statistics. The shape of the grid could also be changed to account for obstructions or smaller workspaces but

best practices recommend that the grid cover as much of the camera field of view as possible. The disadvantage of using the positioning table is that the workspace of the positioning table becomes the workspace of the camera, so if the field of view of the camera extends beyond the reach of the table such areas would be uncalibrated. The accuracy of this method relies on the assumption that the target is rigidly mounted on the table if the target was vibrating errors would be introduced into the extracted camera model. It is also essential that the table is not rotated during the grid movements.

After the measurements, an estimation of the camera model can be performed using a number of methods (**Section 2.6.3**). In this project, the model parameters were estimated using the C++ port of Bouguet's camera calibration toolbox [123] which is available in the OpenCV Library.

4.4.1 Accuracy Evaluation

After calibration of the camera system, it is vital to evaluate the accuracy of the system and evaluate if the accuracy is sufficient to track moving items during an experiment. Several metrics [84] have been used to evaluate the accuracy of camera calibration. The following were used in this thesis:

1. **Accuracy of image points (or Re-projection Error)**: In this metric, the estimated camera model is used to project a set of 3D points into image points. Then the accuracy of calibration is estimated by comparing the real and estimated image points. Because this metric is a comparison between image points, the unit of the comparison is pixels. This metric is useful for spotting errors in the calibration of a single camera, as no information from the second camera is used, however the method may not give a realistic measure of accuracy when both cameras are combined.
2. **Accuracy of 3D points from triangulation (or 3D Error)**: In this method, two or more cameras are calibrated separately. The cameras are used to observe a single fiducial marker with a known 3D position. The 2D centres of the marker can be used along with the estimated camera models to estimate the 3D position of the marker via triangulation. The accuracy of the system can then be determined by comparing the estimated and the known 3D positions. This method is considered to give accuracies which are more realistic as it contains the error from all the cameras.

Single Marker Test

Three successive calibrations were performed using a single fiducial marker moved to 125 positions in a 5 x 5x 5 grid (100mm x 100mm x 400mm); each calibration file was stored. After the third calibration, the same fiducial marker was moved to 125 random positions in the calibrated

workspace also using the positioning system. The developed camera system was used to measure the positions of the fiducial marker at each random position and a laser tracker was used to measure the position of the positioning table as described above. At each random position, all of the three calibration files were used to measure the position of the fiducial markers so as to test the repeatability of the calibration procedure. The re-projection and 3D errors were calculated for each of the points and the results are presented in **Table 4.1** and **Table 4.2**

Re-projection Error		**1st Attempt**	**2nd Attempt**	**3rd Attempt**
Left Camera	**Mean (pixel)**	0.04397	0.03852	0.04544
	Std. dev. (pixel)	0.02169	0.02170	0.02136
	Maximum (pixel)	0.11533	0.11123	0.11285
Right Camera	**Mean(pixel)**	0.12104	0.07325	0.06855
	Std. dev. (pixel)	0.03056	0.02647	0.02846
	Maximum (pixel)	0.19737	0.15268	0.14769

Table 4.1: The results from the single marker accuracy tests on the camera system. The mean, standard deviation, and the largest deviation of the re-projection errors are presented.

3D Error	**1st Attempt**	**2nd Attempt**	**3rd Attempt**
Mean (mm)	0.06108	0.05119	0.04874
Std. dev. (mm)	0.02364	0.02386	0.02484
Maximum (mm)	0.12608	0.10517	0.10401

Table 4.2: The results from the single marker accuracy tests on the camera system. The mean, standard deviation, and the largest deviation of the 3D errors are presented.

A trend can be observed from the results in **Table 4.2**, the average error improves after each attempt. This is probable due to slight movement of the right camera which shows the same trend (see **Table 4.1**). The third attempt is always the most accurate because the third calibration immediately preceded the test measurement while the first calibration was done two hours earlier, in which time the camera might have shifted because of instrument vibrations.

Multiple Marker Test

In this test, three fiducial markers were mounted rigidly on the positioning system and the 3D positions of the centre of the fiducial markers were determined using a probing device. After calibration of the camera system using a set of 125 points in a grid, the positioning system was moved to 125 random positions in the calibrated workspace. At each position, the developed camera system was used to measure the 3D positions of the fiducial markers. The Euclidean distance between the markers were calculated and compared against the actual distance determined using the probing device. The result from the comparison is shown in the table below.

	Distance 1-2	**Distance 1-3**	**Distance 2-3**
Actual Distance (mm) (from touch probe)	133.585	203.650	165.018
Mean Distance (mm) (from camera)	133.380	203.673	165.260
Mean Error (mm)	0.20501	0.04877	0.24179
Std. dev. (mm)	0.04765	0.03054	0.03894
Maximum Error (mm)	0.34293	0.13295	0.33054

Table 4.3: The results from the multiple marker accuracy tests on the camera system. The mean distance, mean error, standard deviation, and the largest deviation are presented.

The multiple target tests revealed very large errors in between targets. The standard deviation and the maximum deviation in **Table 4.3** indicate that the distances measured even though erroneous were very repeatable. The high accuracy from the single marker test indicates that a repeatable point is being detected by the centre detection algorithm but the error from the multiple maker tests reveals that the detected point is not actually the centre of the target.

In the previous version of the camera system design in which infrared ring lights were used, the error in the distances between markers ranged between 0.4mm to 0.9mm. These were inexpensive lights and it was hypothesised that the error in the distances between markers was due an uneven distribution of light on the markers. In order to test this, the ring lights were replaced with a pair of white LED ring lights and following this change the errors were reduced as shown in **Table 4.3**. This improvement is considered to be due to a combination of the following:

- The new ring lights provide a more uniform illumination than the previous ones which had exposed LEDs.

- The current lenses have a 10%-20% higher transmission efficiency in the visible light range than with infrared. Transmission efficiency is the efficiency with which the light passes through the lens assembly (some light will be lost to reflection and refraction).
- The current camera sensors have 20%-40% better quantum efficiency with visible light than with infrared. Quantum efficiency is the efficiency with which the sensor converts photons of a certain wavelength into electrons in the sensor.

The mechanism by which the improvement occurs needs to be evaluated further in order to improve the accuracy of the centre detection.

Repeatability of Measurements

In this test, we evaluate the repeatability of measurements made using the camera system. Since most user experiments run for days, it is necessary to evaluate the effect of time on static measurements. A fiducial marker is mounted rigidly on the positioning table and the camera system is used to measure the position of the marker repeatedly at 20 minute intervals for 3 days which implies 72 measurements per day. The laser tracker was setup as a control device to ensure vibrations of the table and other errors that do not arise from the camera system would be detected. An SMR was placed beside the fiducial marker on the positioning table and the position of the SMR was measured during the 3 days. The positioning table was not commanded to move during the experiment but just served as a mounting surface. The magnitude of the deviation of each of the fiducial marker measurements from the average of the 3 days was calculated. The mean deviation, the standard deviation and maximum deviation for the fiducial measurements are presented in **Table 4.4**.

	Day 1	**Day 2**	**Day 3**
Mean (mm)	0.115862	0.137717	0.091589
Std. dev. (mm)	0.047349	0.056568	0.060318
Maximum (mm)	0.190733	0.282468	0.236896

Table 4.4: The results from the single marker repeatability tests on the camera system. The mean, standard deviation, and the largest deviation from the average are presented.

A look at the results in Table 4.4 shows that the position of the static fiducial marker varied by as much as 0.282mm which is not encouraging as the camera system is supposed to monitor experiments that require 0.1mm positioning accuracy. The calculated deviations (see **Figure 4.7a**) show a fairly repetitive pattern in all the components with the largest deviation coming from the z-

component of the measurements. When comparing the measurement from the camera and the measurement from the laser tracker (see **Figure 4.7b**), the same pattern can be observed; this would indicate that the source of the error is not the camera system but with the mounting surface.

It was thought that the observed oscillations were caused by thermal expansion so to evaluate this hypothesis; the same experiment was repeated for a 12 hours period and the measurements were taken at 10 minute intervals. A temperature and relative humidity sensor was placed on the positioning table and the sensor was configured to record the temperature and relative humidity at 2 minute intervals. The resulting reading (see **Figure 4.8**) showed no correlation with the measured position data which still contained the oscillations. The log files from the motion control team at ISIS confirmed that the motors of the positioning table did not move during the testing period. The laser target and the fiducial marker were then moved off of the positioning table and remounted near one of the instrument's collimators. The experiment was repeated in this new location, the results showed similar oscillations but with a smaller amplitude.

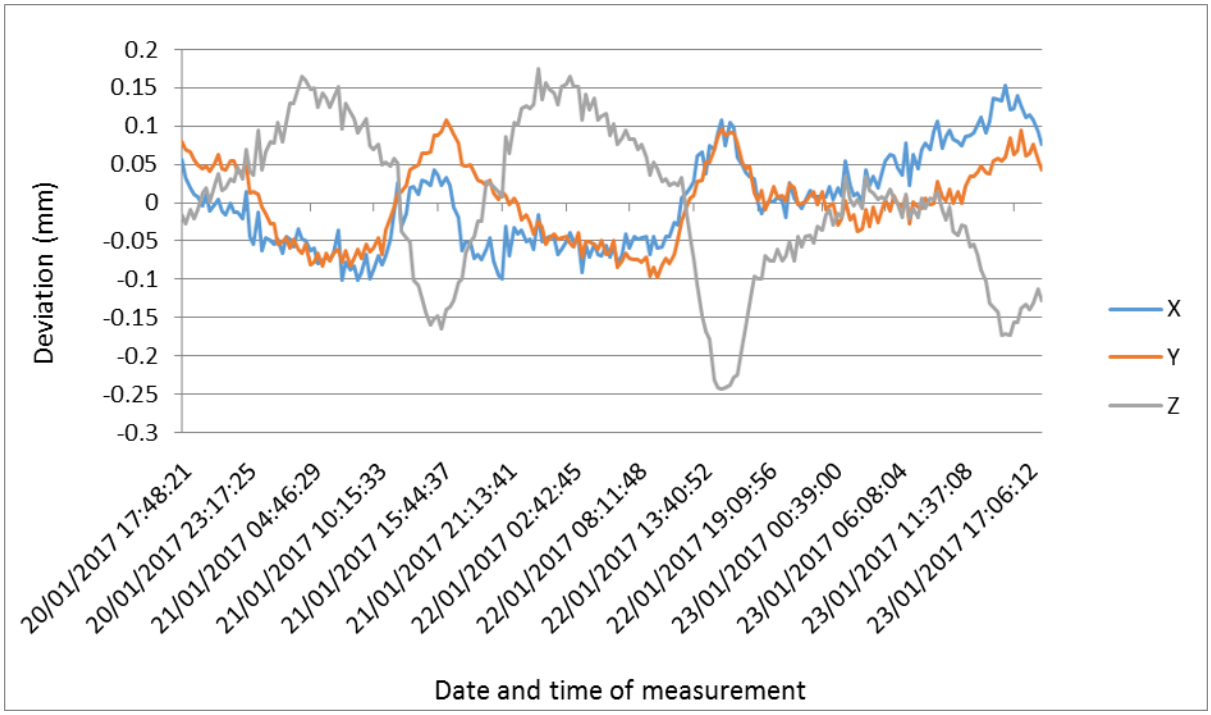

(a)

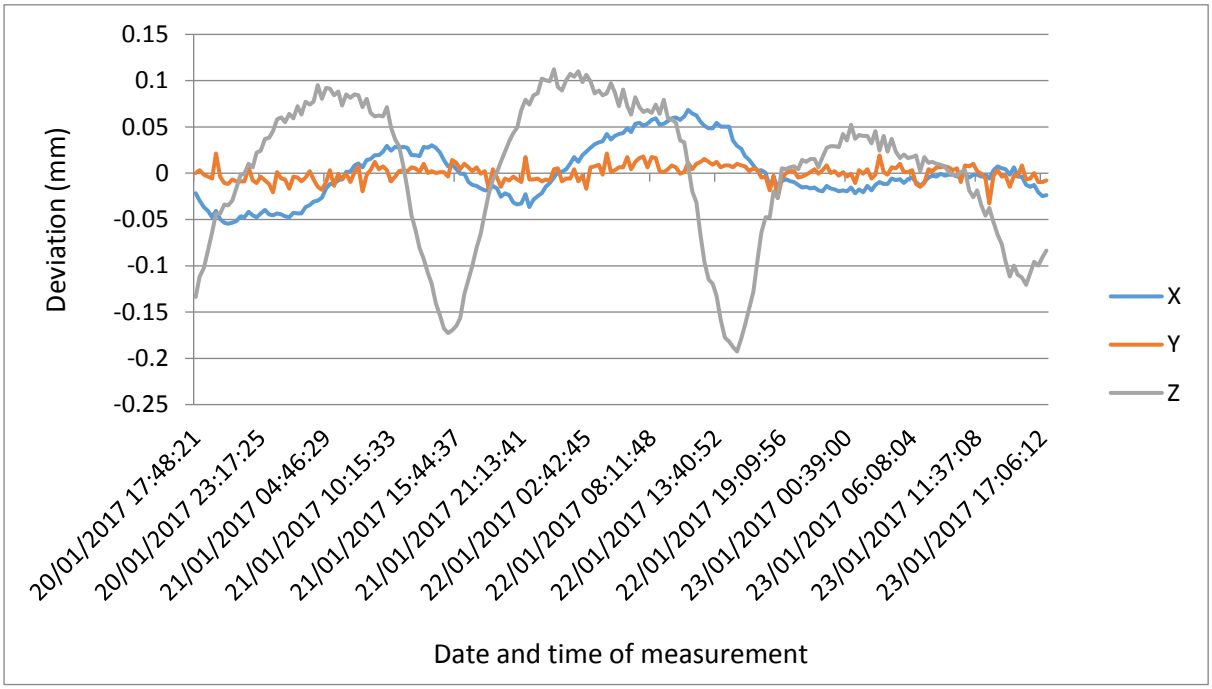

(b)

Figure 4.7: The errors from the repeatability tests conducted on the camera system. **(a)** shows the measurements from the camera system and, **(b)** shows the control measurements from the laser tracker

Vibrations have been noted on the ENGIN-X instrument for some time but measurements have never been made to validate the nature of these vibration. It is probable that the error observed are

caused by the vibration of the instrument therefore the repeatability of the camera system could not be properly quantified in the instrument hutch. A controlled lab is required to properly evaluate the repeatability and accuracy of the camera system indicating that a more rigid mounting rig is necessary if the system is to perform optimally in a real experiment.

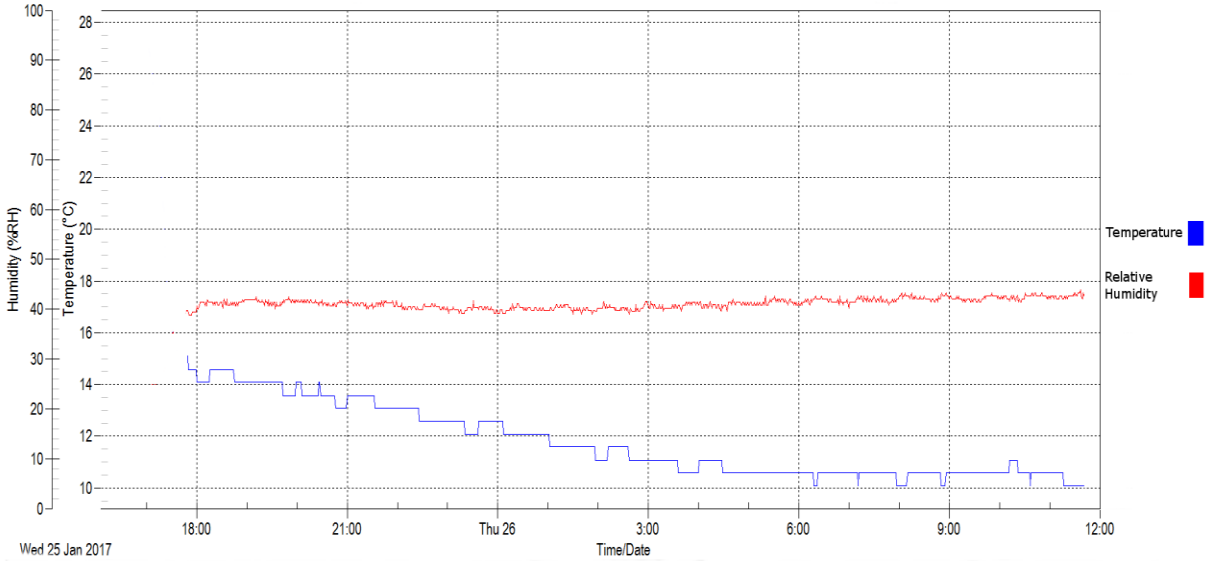

Figure 4.8: Temperature and relative humidity measured during the repeatability test performed on the camera system.

Comparison of Calibration Algorithms

In this test, the selected calibration algorithm is compared against the other established algorithms to ensure that no bias or errors exist in the current implementation. This test could also indicate whether other algorithms outperform the selected one. The camera system was re-calibrated using the original MATLAB version of the Bouguet's toolbox with the (k_1, k_2, p_1, p_2) distortion parameters, Faugeras [124] algorithm which only accounts for the first order radial distortion (k_1) and Weng et al algorithm [86] which accounts for thin prism distortion alongside the (k_1, p_1, p_2) distortion parameters. The data used is the same from the third attempt of the single marker tests.

	Bouguet [OpenCV C++]	Bouguet [Matlab]	Faugeras [Matlab]	Weng [Matlab]
u_0	971.111	931.115	971.328	805.997
v_0	520.671	496.175	523.842	525.911
sf	1662.194	1659.722	-1664.016	1660.474
f	1661.058	1658.978	1663.120	1663.667
k_1	-0.35172	-0.35000	0.38531	0.37356
k_2	0.00000	-0.10176	0.00000	0.0000
p_1	0.00022	0.00026	0.00000	-0.03771
p_2	0.00080	-0.00001	0.00000	0.00149
s_1	0.00000	0.00000	0.00000	0.02487
s_2	0.00000	0.00000	0.00000	-0.00164

Table 4.5: Comparison of different calibration algorithms using a single marker. The resulting intrinsic parameters from each algorithm are presented. The unit of the intrinsic parameters (u_0, v_0, f, sf) is pixels while the distortion parameters $(k_1, k_2, p_1, p_2, \mathrm{s}_1, \mathrm{s}_2)$ are dimensionless

The results from the table above show that the tested algorithms and implementations have a reasonable correspondence for many of the parameters. It can be seen that the principal point (u_0, v_0) is very close to the centre of the sensor which has a dimension of 1920 by 1080 pixels. This is crucial for the convergence of some of the algorithms which used the centre of the sensor as a starting guess for the principal point. The principal point of the Weng algorithm deviates the most from the sensor centre which is probably due to the extra distortion parameters in the calibration procedure. The scale factor (s) is close to 1 since the values of f and sf are nearly identical which confirms that the pixels are actually square. The distortion parameters are similar even though and Faugeras and Weng use an inverse distortion model hence the positive distortion value for k_1. The accuracy results in **Table 4.6** also show good correspondence from which it can be deduced that the thin prism distortion (s_1, s_2) provide no significant accuracy improvement when used in the model.

	Bouguet [OpenCV]	Bouguet [Matlab]	Faugeras [Matlab]	Weng [Matlab]
Mean (mm)	0.04874	0.04784	0.05091	0.04578
Std. dev. (mm)	0.02484	0.02450	0.02405	0.02491
Maximum (mm)	0.10401	0.107712	0.11188	0.11931

Table 4.6: Comparison of different calibration algorithms using a single marker. The mean, standard deviation and the largest deviation from the average (in mm) are presented.

4.5 Applications

It is anticipated that the proposed camera system could be used to solve a myriad of problems on neutron diffractometers, such as collision avoidance, instrument and sample monitoring, safety checks etc. In this dissertation, both sample monitoring and sample correction were implemented on the ENGIN-X instrument. It should be noted that the applications discussed below have been implemented in software and tested in simulation but have not be practically tested due to challenges with the camera system which have been mentioned in the previous section

4.5.1 Sample Monitoring

Given a sample with mounted retroreflective markers as in **Figure 4.1**, the sample is digitised using a scanning device, and the locations of the fiducial markers determined using a touch probe or by fitting point clouds using the same scanner. The known locations of the fiducial markers can be used to determine the pose of the sample during the experiment. The pose of the sample at each measured position can be stored alongside the neutron measurements. This data could allow the following

1. While analysing the neutron data, it might be very useful to remember how the sample was aligned during the measurement and the accuracy of the alignment. With this pose data, the user could replay all the measurements made during the experiments (in simulation software like SScanSS) and confirm visually that the measurement were made in the correct location.
2. If simulations were used to plan the experiment, the measured poses can be compared with the simulated poses in real-time and the user can be notified that the sample is not aligned in the desired location.

4.5.2 Sample position correction via visual servoing

In situations where the sample has been determined to be misaligned, it is possible to automatically correct the alignment of the sample using a technique known as visual servoing. In visual servoing, the camera system is used as a feedback system to correct the pose of the end effector of the robot (in this case, the sample).

The manipulator Jacobian is the first order derivative of the forward kinematic function with respect to Joint variables therefore the change in end effector position and orientation can be estimated as $\Delta X \approx J\Delta q$. This is the same Jacobian as used in the Jacobian measurement method and hence has been described in **Chapter 2** of this thesis. The Jacobian matrix is not invertible in the cases of over-constrained (< 6DOF) or redundant (> 6DOF) manipulators. One solution is to invert the matrix using the Moore-Penrose pseudoinverse $J^{\dagger} = J^{T}(JJ^{T})^{-1}$. The change in joint variables Δq is computed as $\Delta q = J^{\dagger}\vec{e}$.

$$q = q + \Delta q \tag{4.5}$$

The joint variables are updated iteratively using the equation above. The iteration would be stopped when sufficient accuracy is achieved or after a specific number of iterations have been reached. The Jacobian pseudoinverse is unstable when the manipulator is in or near a singular configuration. In a singular configuration, J is not of full row rank, which is still an issue with the Jacobian inverse kinematics methods.

The analysis of the Jacobian matrix of the ENGIN-X positioning table revealed that the matrix would always be full rank irrespective of the configuration selected. This is not the case with the revolute manipulator whose zero configuration is nearly singular because the axes of Joint A and Joint C are closely aligned (see **Figure 3.13**). In this configuration, the motion caused by actuating Joint A is similar to the motion cause by actuating Joint C. This implies that the Jacobian pseudoinverse could be unstable around the zero configuration of the revolute manipulator. The Jacobian pseudoinverse method worked well for the positioning table but performed poorly on the revolute manipulator due to singularity and local minima issues.

Several modifications to the Jacobian pseudoinverse have been proposed in literature to meet the various challenges of the method [125]. In this thesis, one such modification called the Damped Least squares method was implemented. This method which uses $J = J^{T}(JJ^{T} + \lambda^{2}I)^{-1}$ in place of the Moore-Penrose pseudoinverse above and the change in the joint variables is computed as above. The non-zero damping constant $\lambda > 0$ is included as a solution to some of the singularity problems present in the original method. When $\lambda = 0$, the method is equivalent to the Jacobian pseudoinverse method. The inclusion of this damping factor increased the performance of the method for the revolute manipulator.

5 Experimental validation and Applications

In this chapter, descriptions of user experiments are presented that demonstrate the advantage of the methods developed in this project

5.1 Copper Bolt Experiment

The calibrated kinematic models of the ENGIN-X positioning system were applied in a user experiment designed to measure spatially resolved texture in a number of large copper bolts which were used in the construction of 18th century British naval warships. Archaeological samples such as these cannot be destructively analysed because of the value of the samples hence non-destructive methods such as neutron diffraction are very suitable. The purpose of the experiment was to determine the method by which the bolts were produced whether rolling, drawing, or swaging etc.; and any other information about the service history of the bolts. Previously, an experiment had been conducted [126] on the same bolts without the calibrated revolute manipulator. In that experiment the samples required manual handling to acquire the necessary measurements. A comparison between that experiment and the experiment that used the combined model is presented in **Section 5.1.3**.

Texture measurements are typically made with several different rotations and tilts of the sample so as to determine the complete pole figure. The texture analysis method used in both experiments is based on splitting the ENGIN-X detector into smaller virtual detectors. This improves the angular resolution and increases the number of directions explored for a fixed orientation of the specimen [127]. A number of incomplete experimental pole figures are used to define the orientation distribution function (ODF) of the material. The best ODF is determined by solving a minimization problem, more information about the technique can be found in [127].

5.1.1 Description of Sample

The archaeological samples shown in **Figure 5.1** are copper bolts recovered from the shipwreck of two warships from the British Royal Navy. The characterization of the bolts from the identified shipwrecks, HMS Impregnable and HMS Pomone, would allow the archaeologist to acquire a better understanding of the construction and the history of the ships. A more complete description of the bolts and the historical context can be found in [126].

Figure 5.1: The Copper bolts for the texture measurement. The largest bolt is 956mm long and 35.5mm in diameter.

5.1.2 Experiment Description

Steel ball bearings were mounted on each sample to serve as fiducial markers. The fiducial markers were sprayed with white paint to minimise the specular reflections of the ball so as to ensure better visibility to the laser scanner (see **Figure 5.2**). After spraying, the samples and fiducial marker were scanned using a laser scanner; the locations of the fiducial markers were determined from the scanned sample model by fitting a sphere to the scanned data. At the start of the experiment, the ENGIN-X revolute manipulator was mounted on the positioning table and the first bolt (the largest) was mounted on the manipulator. The revolute manipulator was moved to four different configurations and at each pose the positions of the accessible fiducial balls were measured. The algorithm detailed in **Section 3.5** was used to calculate the base and tool matrices for the revolute manipulator. As mentioned in **Chapter 3**, the calibrated kinematic models were incorporated in the SScanSS software and the addition of the base and tool matrices described above completed the combined model of the positioning system and mounted sample. It should be noted that the base matrix would only be determined once during the entire experiment, unless the revolute manipulator is physically removed from the positioning system. With the known base matrix, the tool matrix can simply be recomputed using the algorithm in **Appendix C** whenever the sample is re-mounted or changed.

Figure 5.2: One of the copper bolts with attached fiducial markers; the markers were sprayed white to reduce specular reflection to the laser scanner.

The laser captured virtual sample model was loaded into SScanSS and the experiment plan was generated. In order to test the accuracy of the model the numerical inverse kinematics implementation in SScanSS was used to generate a motor script that would bring each fiducial ball to the centre of the gauge volume. A few of the fiducial balls were then moved into the gauge volume, their positions were validated using the theodolite in the hutch. The accuracy of the sample positioning could not be validated using other measuring devices due the limited time given for the setup. The generated motor scripts were used to automate the instrument control for the entire experiment. An example of the experimental setup and corresponding SScanSS virtual model are shown in **Figure 5.3**.

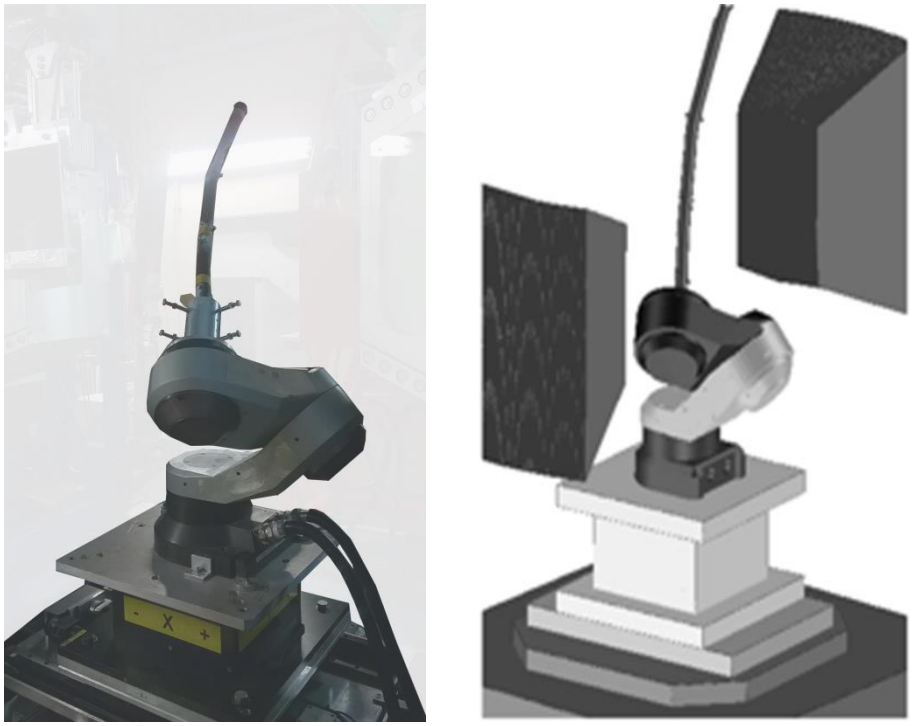

(a) **(b)**

Figure 5.3: User experiment to measure spatially resolved texture in copper bolts **(a)** Photographic record of the experiment. **(b)** Screen capture of corresponding SScanSS simulation, including calibrated sample positioning system, laser scanned sample model and ENGIN-X detector banks

Using this model-based approach individual measurement points were automatically brought to the gauge volume and rotated, as required, around three axes of rotation. The construction of the ODF also requires knowledge of the path lengths travelled by the neutrons to each virtual detector element and these were output automatically by the SScanSS software for each orientation (this development was not part of this project).

5.1.3 Contributions

Measuring spatially resolved texture in this manner, while providing a useful first test of the calibrated positioning system, is not a typical use of ENGIN-X and an example of the application of these techniques to the more usual strain scanning experiment will be reported in the next section. The contributions of the techniques proposed in **Chapter 3** of this thesis to the copper bolt experiment are the following:

Flexibitity

As previously mentioned an experiment had been conducted on the same bolts before the calibration of the positioning system. The nominal models of the three axis manipulator although

available lacked the accuracy and reliability necessary for that user experiment. Hence the samples were mounted as shown in **Figure 5.4a** using fabricated wood pieces. Using this arrangement, the sample could only be rotated automatically around a single axis (the axis of the rotation stage). When other orientations were required the sample had to be detached and remounted in that orientation. This limited the number of measurements made and prevented the researchers from making measurements in certain orientations because of the difficulty of alignment.

(a) **(b)**

Figure 5.4: The alignment of the HMS Pomone copper bolt for texture measurement showing **(a)** the previous experiment without the calibrated positioner model **(b)** the experiment with the calibrated model.

In the second experiment, the calibrated positioning system was used to align all the samples, and a fabricated aluminium holder was used to attach the sample to the positioner (**Figure 5.4b**). The alignment technique allowed for large degree of flexibility and the researchers were able to make measurement at several orientations without manual reorientation or physical intervention. Without model based alignment, it would be non-trivial to find the joint configurations of the three axis manipulator that positions the measurement points in the gauge volume. Only model based techniques can determine the orientation of the sample and this property is very desirable for texture experiments.

Maximized Beam-time

The first day of the experiment was spent setting up and validating the calibrated positioning system model. Since this experiment was the first in which the calibrated positioning system model would be used, the setup took the whole day but subsequent experiments should benefit from a significant improvement in setup time. The proposed alignment technique increased the throughput of the experiment by allowing non-stop measurements. These measurements allowed the researchers to

further enhance the texture measurement method. Without the proposed method, almost every measurement would have required the user to stop and realign the sample but with the method, the time spent realigning the sample and verifying the alignment with theodolites was spent making useful measurements on the sample.

5.2 Stress Measurement on Creep specimen

This experiment was designed to measure the complete stress tensor of creep specimens by measuring the strain at different orientations [128]. Although the methods developed in this thesis were demonstrated with the user's samples, the methods were not used for the actual neutron measurements due to problems that will be discussed in this section.

In many stress measurement experiments, assumption are made that minimize the number of required measurement orientations to three principal directions however in this experiment measurement were made in more than three arbitrary orientations. Multiple measurements of strain in different directions leads to a system of linear equations [128]. In the case where there are six or more measurements (from non-coplanar orientations) the complete strain tensor may be solved

5.2.1 Description of Sample

Six 316H stainless steel samples were measured in this experiment. The samples were attached to an aluminmum specimen holder and the speciman holder was attached to the standard VAMAS mounting plate. The Unstrained lattice parameter specimens (or d-zeros) were attached to one of the six samples as shown in **Figure 5.5**.

5.2.2 Experiment Description

At the start of the experiment, the 3mm collimators were mounted on the instrument and aligned. In this experiment, the traditional fiducial marker system which used ball bearing and a touch probe was replaced with a more accurate and time saving alternative. A total of six laser target holders were mounted on the sample assembly with three holders been mounted on the specimen holder while the others were placed on the mounting plate as shown in **Figure 5.5**. The whole sample assembly was scanned using a FARO Edge measuring arm with an attached laser line scanner. The centre of each fiducial marker was determined by placing an SMR on the target holder and probing the SMR with the FARO Edge which is designed to perform the laser scanning and probing operations in the same coordinate frame. By using the FARO Edge, the need to spray paint the fiducial markers for scanning is eliminated.

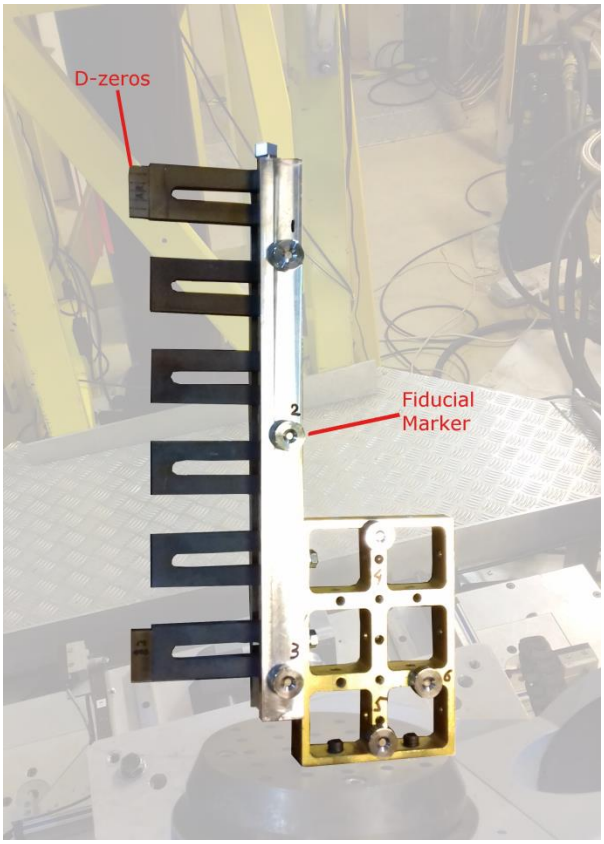

Figure 5.5: The sample assembly for the creep stress experiment.

The revolute manipulator was mounted on the positioning table and the sample assembly was mounted on the manipulator. The revolute manipulator was moved to four different configurations (see **Figure 5.6**) and at each position the visible fiducial points were measured. The algorithm detailed in **Section 3.5** was used to calculate the base and tool matrices for the revolute manipulator. The computed matrices were inputted into the SScanSS package. A few measurements were made to ensure that the system would perform accurately enough for the experiment but the test measurements showed that the achieved accuracy was not sufficient for the experiment. The reason for the inaccuracy was later found but because the error source could not be corrected without consuming time, the actual experiment was performed without the revolute manipulator model. Even though the calibrated model was not used for the experiment, subsequent analysis of the errors observed provides a valuable insight into errors that might be present in other experiments that attempt to use automatic positioning. The cause of the inaccuracy would now be discussed in the next section

5.2.3 Discussion

Using the 10% rule, a gauge volume of 3mm would signify the desired positioning accuracy should be better than 0.3mm. Good accuracy was also necessary to avoid collisions with other parts of the

instrument as some of the measurement orientations required movements in close proximity to the hardware. The base and tool matrices were determined using the configurations 1-4 detailed in **Table 5.1**. After these matrices were determined, measurements were made in two other configurations (5 and 6) also listed in **Table 5.1.**

Figure 5.6: The sample assembly mounted on the revolute manipulator oriented in one of the four configurations used to determine the base and tool matrices.

The model achieved an average of 0.14168mm with a standard deviation of 0.08841mm and a maximum error of 0.37377mm on the 11 points measured in the two test configurations.

The maximum error exceeded both the recommended accuracy for the experiment and the anticipated error which, based on previous tests, was expected to be approximately 0.1mm. Recall, that six points were mounted on the specimen holder with three mounted on the mounting plate. The worst point in both configurations was always fiducial point 1 (see **Figure 5.5**) which was the highest point on the sample assembly. This sort of error could be due to vibrations of the sample or small angular errors of the goniometer joint being amplified along the length of the sample

Configurations	A (Deg)	B (Deg)	C (Deg)	No of visible points
1	0.00	0.00	0.00	6
2	90.00	-90.00	50.00	4
3	-90.00	90.00	-50.00	6
4	90.00	180.00	90.00	6
Test Configurations				
5	-180.00	-5.00	150.00	6
6	-100.00	-170.00	-100.00	5

Table 5.1: Joint configurations used for the base and tool calculation and the two configurations used to test the calculated base and tool matrices.

Investigating the rigid transformation between the points measured at each configuration and the points measured when the sample was scanned, a trend was observed; (see **Figure 5.7**) with the fiducial markers mounted on the specimen holder (numbers 1-3) have larger error[17] than those mounted on the VAMAS mounting plate. This could indicate that the specimen holder had moved slightly from its original position. This shift would contribute to errors in the base and tool matrix calculation which might explain the larger than expected errors. It should be noted that fiducial point 3 consistently produced worse errors than points 4, 5, and 6 even though point 3 had closer or similar distance to the mounting plate than those points. This observation could exclude vibration as a source of the errors as vibrations would be amplified when the point is further from the mounting plate.

[17] The rigid transformation error is the calculated by transforming the measured point into the same coordinate frame as the scanned points then the Euclidean distance between the transformed and scanned point calculated

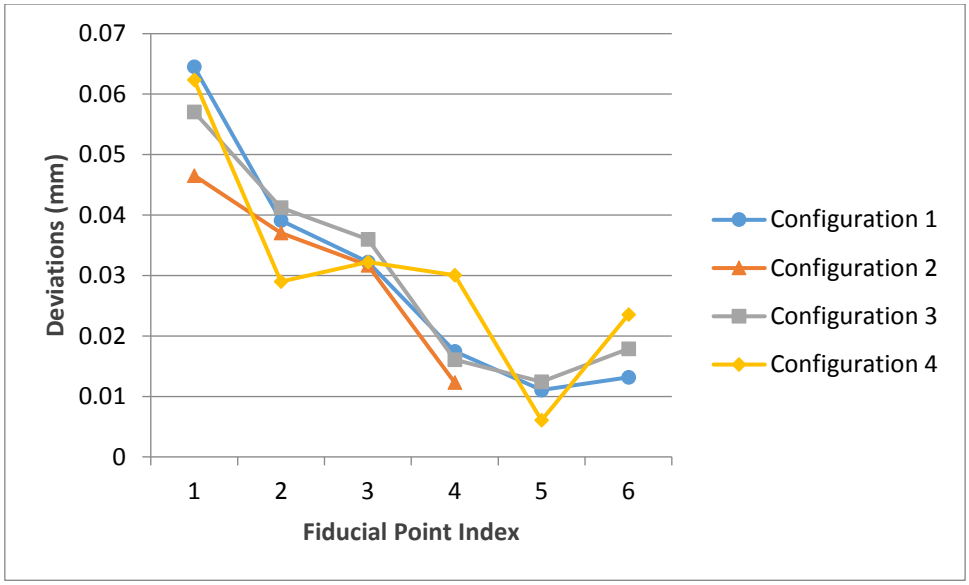

Figure 5.7: The rigid transformation error for all the fiducial point measured in four different configurations.

To test the hypothesis that the specimen holder had shifted, the rigid transformation analysis was repeated using only the fiducial points on the VAMAS mounting plate (numbers 4-6). The result (**Figure 5.8**) showed improved accuracy of the rigid transformation for 3 of the 4 configurations, the rigid transformation for configuration 2 could not be calculated as only one fiducial marker on the mounting plate was visible in that configuration. Finally, the base and tool matrices were recomputed using only the fiducial points on the mounting plate and the model was re-tested using the same test configurations. The model achieved an average of 0.12367mm, standard deviation of 0.05482mm and the maximum error of 0.23301mm on the same 11 points previously measured which is a considerable improvement over the previous model.

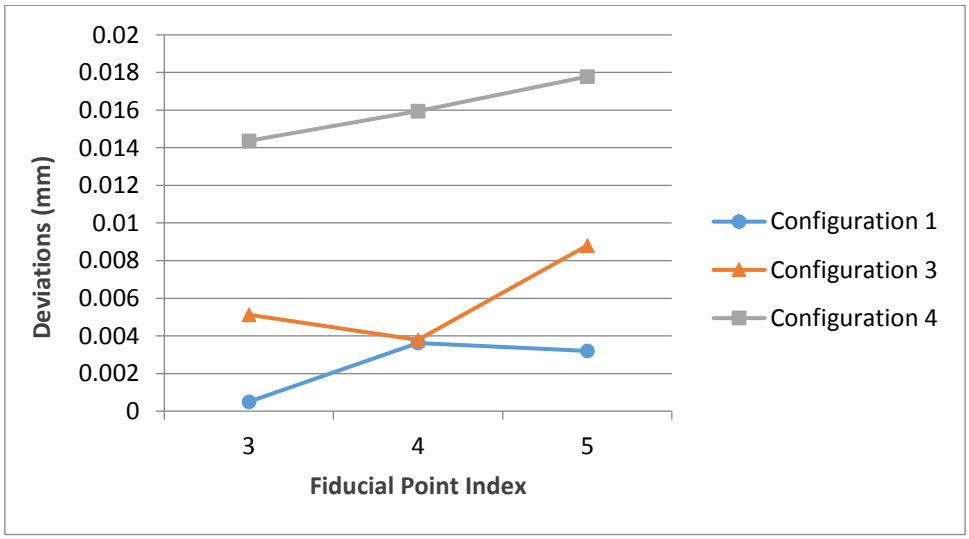

Figure 5.8: The rigid transformation error for the fiducial point attached to the VAMAS mounting plate measured in three different configurations.

Due to time limitations inherent in a user experiment, it was not possible to fully evaluate the source of the shifts which could have been due to erroneous scanning, thermal expansion or non-rigid mounting. In the absence of a complete understanding of the error source, it was decided that the experiment should proceed with a semi-manual alignment.

6 Conclusion

6.1 Summary & Conclusions

Accurate sample alignment is essential for stress measurement on neutron diffractometers. Model based alignment is frequently used for aligning samples at many neutron instruments. In this thesis, the modelling of positioning systems and the monitoring of the instrument is proposed as solutions to some of the challenges of the model based alignment technique.

6.1.1 Modelling of Positioning Systems

One major challenge facing model based alignment is the discrepancy between simulated and real motion due to inaccurate modelling of positioning systems. In this thesis, robotic calibration is demonstrated as an effective tool for accurately determining the kinematic parameters of both custom and off shelf serial positioning systems used by neutron diffractometers, irrespective of whether these systems are used to align detectors, samples, jaws or cameras. It has been shown how additional, non-geometric error sources such as eccentricity may be identified and modelled to further improve model accuracy. The resulting calibrated hardware can be used to perform rapid, accurate sample alignment and so further improve the scientific output and quality assurance of beam line experiments.

The SScanSS software was modified to allow updated model kinematic parameters to be read from a simple text file after manipulator calibration. The potential of the calibration technique is demonstrated in two user experiments which used SScanSS for experimental planning and control.

It is recognised that kinematic calibration alone might not be sufficient for experiments such as near surface measurements where even more accurate positioning of the sample in relation to the beam is required. It is anticipated that such positioning requirements may be met by some combination of the following options:

- Develop a more complex model that takes into account the dynamics rather than just the kinematics of the positioning system.
- Use a measuring device to perform visual servoing on the instrument.
- Use the neutron beam to check and automatically modify the alignment of the sample.

6.1.2 Monitoring the Instrument

Another challenge of model based alignment techniques is the inability to detect positioning failure. A very accurate model of the instrument could fail if physical repairs have been carried out on the positioning system or following a collision. In such a situation, offline simulation would be incorrect

and lead to wrong results. In this thesis, a stereo camera system was developed to monitor the sample and other moving parts of the neutron diffractometer. The camera system is designed to measure the positions of retroreflective markers attached to any object that is being monitored. A fully automated camera calibration procedure was developed with an emphasis on accuracy. The system was tested and showed the potential for highly accurate measurements. Average accuracies of about 50microns were achieved when tracking a single marker. Issues with the sphere centre detection and instrument vibration still limit the potential of this device.

It is anticipated that the camera system would be used to correct the positioning system when the error is minimal or notify the user of the error when it is significant.

6.2 Contributions of the thesis

1. First author of paper titled “Modelling and control of neutron and synchrotron beamline positioning systems” [99].
2. Co-author of a paper titled “Spatially resolved texture analysis of Napoleonic War Era Copper bolts” [129].
3. Robot calibration code written in IDL which has partly been included into the SScanSS package.
4. A new algorithm for solving the robotic base and tool calibration problem.
5. A new algorithm for extracting Hayati D-H parameters from a point and axis.
6. Development of a camera metrology system for ENGIN-X.
7. Extensive repeatability and accuracy analysis of the ENGIN-X positioners

6.3 Further Work

1. **Publish Papers**: Some of the novel contributions of this work are yet to be published due to time required to write and find the appropriate journals. The base and tool calibration technique presented in **Chapter 3** used a new non-linear method to determine the tool and the base matrix of the positioner. Also the method used to extract Hayati D-H parameters from the measured centre points and joint axes also presented in **Chapter 3** used a novel vector analysis method. Attempts would be made to publish both techniques if time permits.
2. **Complete the monitoring system:** As discussed in **Chapter 4**, a few challenges limited the potential of the developed camera system. If the system must achieve the accuracy shown in the single marker test, the sphere centre detection and vibration problems must be overcome. The sphere centre detection might be improved further by optimisation of the ring lighting but this has to be tested. The vibration detected on the instrument could be addressed by using a more rigid mounting system.

3. **Visual Servoing on ENGIN-X:** An important application of the developed feedback system in **Chapter 4** is the ability to correct the sample if it is found to be aligned with insufficient accuracy. This would be valuable for experiments requiring higher accuracy than that which the positioning system can provide on its own. A possible challenge with visual servoing around a neutron diffractometer is the high risk of colliding with parts of the instrument. One way of minimising this is to limit the amount of error that the visual servoing system attempts to correct if the error exceeds the specified limit; the user is notified of errors that cannot be corrected. Another way of avoiding this is to impose virtual bounding boxes around the sample, jaws and the collimators and check the boundaries of these boxes for collisions during every movement of the positioner.
4. **Automation**: A major hindrance to the uptake of model-based alignment techniques is that they require some extra work on the users' part which could be seen as time consuming when limited beam time is available. Tasks such as measuring the location of sample fiducial marker on the instrument, aligning the coordinate frame of the measurement devices, calibration of the positioning systems etc. should be fully automated so that the users are content to use model based alignment since it costs them no extra effort. This automation would require software and hardware integration with the instrument, further testing would be vital to ensure that the accuracy of the automated system is not less than the manual counterparts. Also safety checks must be in place to prevent collisions during the automatic runs of any of these systems.
5. **Self-learning instruments**: The data collected from the monitoring system can be used to create smart instruments which are able to diagnose problems and make suggestions for improvements. For example, if measurements repeatedly showed more errors in positioning along a particular axis such a system could suggest recalibration of that axis, cleaning of the stage, or replacement depending on its analysis. Machine learning could be used to analyse other factors that lead to better performance of the instrument and also provide suggestion for optimization of a single experiment or the instrument as a whole.
6. **Another Instrument:** The methods presented in this thesis have been applied to the ENGIN-X instrument. It is anticipated that these techniques will be applied to the IMAT instrument which is a combined neutron imaging and diffraction instrument at the ISIS facility. It is expected that the virtual model of the IMAT instrument would be included into the SScanSS package, in which case all the methods presented would be directly applicable with minimal modification.

References

[1] P. J. Withers and H. K. D. H. Bhadeshia, “Residual Stress Part 1 - Measurement Techniques,” *Materials Science and Technology,* vol. 17, pp. 355-365, 2001.

[2] IAEA, “Measurement of residual stressin materials using neutrons,” IAEA, Vienna, 2003.

[3] J. R. Santisteban, M. R. Daymond, J. A. James and L. Edwards, “ENGIN-X: a third-generation neutron strain scanner,” *Applied Crystallography,* vol. 39, no. 6, pp. 812-825, 2006.

[4] N. Ratel, D. J. Hughes, A. King, B. Malard, Z. Chen, P. Busby and P. J. Webster, “Direct sample positioning and alignment methodology for strain measurement by diffraction,” *Review of Scientific Instruments,* vol. 76, no. 5, 2005.

[5] M. Johnson, L. Edwards and P. Withers, “ENGIN — A new instrument for engineers,” *Physica B: Condensed Matter,* vol. 234–236, pp. 1141-1143, 1997.

[6] P. Brand, “The Alignment and Positioning of Specimens for Stress Measurements by means of Neutron Diffraction,” in *Measuremnt of Residual and Applied Stress Using Neutron Diffraction*, Netherlands, Kluwer Academic Publishers, 1992, pp. 335-346.

[7] J. A. James, J. R. Santisteban, L. Edwards and M. R. Daymond, “A virtual laboratory for neutron and synchrotron strain scanning,” *Physica B: Condensed Matter,* vol. 350, no. 1-3, p. 743–746, 2004.

[8] J. James, E. Oliver, A. Paradowska, C. Hubbard, J. Schmidlin and L. Edwards, “Robotics methods for beam line instrument simulation and control,” in *NoBugs*, Sydney, 2008.

[9] R. Wimpory and M. Boin, “Looking Towards the Future of Strain Scanning Using Neutron Diffraction,” *Advanced Materials Research,* vol. 996, pp. 187-191, 2014.

[10] J. Altenkirch, A. Steuwer, P. J. Withers, T. Buslaps and U. Berger, “Robotic sample manipulation for stress and texture determination on neutron and synchrotron X-ray diffractometers,” *Nuclear Instruments and Methods in Physics Research A,* vol. 584, pp. 428-435, 2008.

[11] H. G. Brokmeier, C. Randaua, W. Tekouo, M. Hofmann, W. M. Gan, M. Mueller, A. Schreyer and W. Petry, “The Robot Concept at STRESS-SPEC for the Characterisation or Semi-Finished Products,” *Materials Science Forum,* vol. 652, pp. 197-201, 2010.

[12] G. A. Webster and R. W. Wimpory, “ISO/TTA 3:2001 Polycrystalline Materials - Determination of Residual Stresses by Neutron Diffraction,” 2001.

[13] C. Randau, H. G. Brokmeier, W. M. Gan, M. Hofmann, M. Voeller, W. Tekouo, N. Al-

hamdany, G. Seidl and A. Schreyer, “Improved sample manipulation at the STRESS-SPEC neutron diffractometer using an industrial 6-axis robot for texture and strain analyses,” *Nuclear Instruments and Methods in Physics Research Section A,* vol. 794, no. 11, pp. 67-75, 2015 .

[14] J. James and L. Edwards, “Application of robot kinematics methods to the simulation and control of neutron beam line position positioning systems,” *Nuclear Instruments and Methods in Physics Reaseach A,* vol. 571, pp. 709-718, 2007.

[15] J. Merlet, Parallel Robots, Second Edition ed., Springer, 2006.

[16] S. Briot and I. A. Bonev, “Are parallel robots more accurate than serial robots?,” *Trans. CSME,* vol. 31, no. 4, pp. 445-456, 2007.

[17] Wikipedia, “Stewart platform,” [Online]. Available: https://en.wikipedia.org/wiki/Stewart_platform. [Accessed 10 September 2017].

[18] Epson America, Inc., “Epson C4 Compact 6-Axis Robts,” [Online]. Available: http://robots.epson.com/product-detail/145. [Accessed 10 September 2017].

[19] T. Pirlinga, G. Brunoa and P. J. Withers, “SALSA—A new instrument for strain imaging in engineering materials and components,” *Materials Science and Engineering: A,* vol. 437, no. 1, p. 139–144, 2006.

[20] J. Craig, Introduction to Robotics: Mechanics and Control, 3rd ed., Boston, MA, USA: Addison-Wesley Longman Publishing Co., 1989.

[21] J. Funda, R. Taylor and R. Paul, “On homogeneous transforms, quaternions, and computational efficiency,” *Robotics and Automation, IEEE Transactions on,* vol. 6, no. 3, pp. 382-388, June 1990.

[22] H. ElMaraghy, “Kinematic and Geometric Modelling and Animation of Robots,” in *Proc. of Graphics Interface '86 Conference*, Vancouver, May 1986.

[23] P. Corke, Robotics, Vision and Control: Fundamental Algorithms in MATLAB, Springer, 2011.

[24] M. Spong, S. Hutchinson and M. Vidyasagar, Robot Modeling and Control, John Wiley and Sons, Inc, 2005.

[25] H. Lipkin, “A note on Denavit-Hartenberg notation in robotics,” in *Proc. ASME IDETC/CIE*, Long Beach, California, Sept 2005.

[26] L.-W. Tsai, Robot analysis: the mechanics of serial and parallel manipulators, John Wiley and Sons, Inc, 1999.

[27] D. G. A. Tolani and N. Badler, “Real-Time Inverse Kinematics Techniques for

Anthropomorphic Limbs," *Graphical Models,* no. 62, p. 353–388, 2000.

[28] O. Ivlev and A. Graser, "An analytical method for the inverse kinematics of redundant robots," in *Proc. 3rd ECPD Int. Conf. on Advanced Robots, Intelligent Automation and Active Systems*, Bremen, 1997.

[29] A. Aristidou and J. Lasenby, "Inverse Kinematics: a review of existing techniques and introduction of a new fast iterative solver," Department of Information Engineering at University of Cambridge, Cambridge, September 2009.

[30] B. W. Mooring, Z. S. Roth and M. R. Driels, Fundamentals of manipulator calibration, New York: Wiley Interscience, 1991.

[31] Z. Roth, B. Mooring and B. Ravani, "An Overview of Robot Calibration," *Robotics and Automation, IEEE Journal of,* vol. 3, no. 5, pp. 377 - 385, 1987.

[32] B. W. Mooring and T. J. Pack, "Aspects of robot repeatability," *Robotica,* vol. 5, no. 3, pp. 223-230, July 1987.

[33] M. Slamani, I. Bonev and A. Nubiola, "Assessment of the positioning performance of an industrial robot," *Industrial Robot,* vol. 39, no. 1, pp. 57-68, January 2012.

[34] L. Everett, M. Driels and B. Mooring, "Kinematic modelling for robot calibration," in *Robotics and Automation. Proceedings. 1987 IEEE International Conference on*, 1987.

[35] L. J. Everett and T. Hsu, "The theory of kinematic parameter identification for industrial robot," *Journal of dynamic systems, measurement, and control,* vol. 110, no. 1, pp. 96-100, 1988.

[36] J. Denavit and R. S. Hartenberg, "A Kinematic Notation for Lower-Pair Mechanisms Based on Matrices," *Trans. ASME, J. Appl. Mech.,* vol. 22, no. 2, pp. 215 - 221., 1965.

[37] S. Hayati and M. Mirmirani, "Improving the Absolute Positioning Accuracy of Robot Manipulators," *Journal of robot System,* vol. 2, no. 4, pp. 397-413, 1985.

[38] W. Newman, C. Birkhimer, R. Horning and A. Wilkey, "Calibration of a Motoman P8 Robot Based on Laser Trackeing," in *Robotics and Automation, 2000. Proceedings. ICRA '00. IEEE International Conference on*, San Francisco, 2000.

[39] M. Perez Rueda, A. Lara Feria, J. Fraile Marinero, J. Delgado Urrecho and J. Gonzalez Sanchez, "Manipulator Kinematic Error Model In a Calibration Process Through Quaternion-Vector Pairs," in *Robotics and Automation, 2002. Proceedings. ICRA '02. IEEE International Conference on*, 2002.

[40] H. Stone, A. Sanderson and C. Neuman, "Arm signature identification," in *Robotics and Automation. Proceedings. 1986 IEEE International Conference on*, 1986.

[41] J. Santolaria, J. Conte, M. Pueo and C. Javierre, “Rotation Error modelling and Identification for Robot Kinematic Calibration By Circle Point Analysis,” *Metrology and Measurement Systems,* vol. 21, no. 1, pp. 85-98, 2014.

[42] W. Veitschegger and C. Wu, “Robot Accuracy Analysis Based on Kinematics,” *Robotics and Automation, IEEE Journal of,* vol. 2, no. 3, pp. 171-179, 1986.

[43] J. Chen and L. Chao, “Positioning error analysis for robot manipulators with all rotary joints,” *Robotics and Automation, IEEE Journal of,* vol. 3, no. 6, pp. 539-545, 1987.

[44] R. Judd and A. Knasinski, “A technique to calibrate industrial robots with experimental verification,” *Robotics and Automation, IEEE Transactions on,* vol. 6, no. 1, pp. 20-30, 1990.

[45] M. Driels and U. Pathre, “Vision-based automatic theodolite for robot calibration,” *Robotics and Automation, IEEE Transactions on ,* vol. 7, no. 3, pp. 351-360, 1991.

[46] M. Švaco, B. Šekoranja, F. Šuligoj and B. Jerbić, “Calibration of an Industrial Robot using a Stereo Vision System,” *Procedia Engineering,* vol. 69, pp. 459-463, 2014.

[47] G. Canepa, J. Hollerbach and A. Boelen, “Kinematic calibration by means of a triaxial accelerometer,” in *Robotics and Automation, 1994. Proceedings., 1994 IEEE International Conference on*, San Diego, CA, 1994.

[48] D. Bennett and J. Hollerbach, “Identifying the kinematics of robots and their tasks,” in *Robotics and Automation, 1989. Proceedings., 1989 IEEE International Conference on*, Scottsdale, Arizona, May 1989.

[49] N. Juneja, “Kinematic Calibration of a Reconfigurable Robot (Robo Twin),” National Library of Canada, Ottawa, 1996.

[50] M. Driels and U. Pathre, “Significance of observation strategy on the design of robot calibration experiments,” *Journal of Robotic Systems,* vol. 7, no. 2, pp. 197-223, 1990.

[51] Y. Sun and J. Hollerbach, “Observability Index Selection for Robot Calibration,” in *2008 IEEE International Conference on Robotics and Automation*, Pasadena, CA, USA, 2008.

[52] J. Hollerbach and C. Wampler, “The Calibration Index and Taxonomy for Robot Kinematic Calibration Methods,” *The International Journal of Robotics Research,* vol. 15, no. 6, pp. 573-591, 1996.

[53] M. Sklar, “Geometric calibration of industrial manipulators by circle point analysis,” in *Proc., 2nd Conf. on Recent Advances in Robotics*, FAU, Boca raton, May 1989.

[54] D. Bennett, J. Hollerbach and P. Henri, “Kinematic calibration by direct estimation of the Jacobian matrix,” in *Robotics and Automation, 1992. Proceedings., 1992 IEEE International Conference on*, Nice, France, May 1992.

[55] J. Hollerbach, L. Giugovaz, M. Buehler and Y. Xu, “Screw Axis Measurement for Kinematic Calibration of the Sarcos Dextrous Arm,” in *Proceedings of the 1993 IEEE/RSJ International Conference on Intelligent Robots and Systems*, Yokohama, Japan, July 1993.

[56] W. Boehler and A. Marbs, “3D Scanning instruments,” in *Proc. of the CIPA WG6 Int. Workshop on scanning for cultural heritage recording*, Corfu, Greece, 2002.

[57] UTCT, University of Texas, “About High-resolution X-ray CT,” [Online]. Available: http://www.ctlab.geo.utexas.edu/overview/. [Accessed 18 Feburary 2014].

[58] Professional Surveyor Magazine, “High Definition Surveying & 3D Laser Scanning: Understanding Laser Scanning Terminology,” 2005. [Online]. Available: http://www.profsurv.com/magazine/article.aspx?i=1377. [Accessed 18 Feburary 2014].

[59] T. Várady, R. R. Martin and J. Cox, “Reverse engineering of geometric models—an introduction,” *Computer-Aided Design,* vol. 29, no. 4, pp. 255-268, 1997.

[60] G. Pavlidis, A. Koutsoudis, F. Arnaoutoglou, V. Tsioukas and C. Chamzas, “Methods for 3D digitization of cultural heritage,” *Journal of Cultural Heritage,* vol. 8, no. 1, pp. 93-98, 2007.

[61] F. Blais, “Review of 20 Years of Range Sensor Development,” *Journal of Electronic Imaging,* vol. 13, no. 1, pp. 231-240, 2004.

[62] D. Sniderman, “3D Scanning Options: How to choose digitizing technologies,” *Destop Enginnering,* pp. 20-23, Jan 2011.

[63] Hexagon Metrology, “All-round upgrade for DEA DELTA SLANT gantry coordinate measuring machines,” 22 March 2010. [Online]. Available: http://www.hexagonmetrology.com.br/press_86.htm?id=2311. [Accessed 10 March 2014].

[64] FARO Technologies Inc., “Measuring arm FaroArm,” [Online]. Available: http://www.faro.com/products/metrology/faroarm-measuring-arm/overview. [Accessed 10 March 2014].

[65] R. Jain, R. Kasturi and B. Schunck, “Chapter 11: Depth,” in *Machine Vision*, McGraw-Hill, Inc., 1995, pp. 289-308.

[66] Z. Bi and L. Wang, “Advances in 3D data acquisition and processing for industrial applications,” *Robotics and Computer-Integrated Manufacturing,* vol. 26, no. 5, pp. 403-413, 2010.

[67] H. Haynes and W. M. Holmes, “The emerging use of Magnetic Resonance Imaging (MRI) for 3D analysis of sediment structures and internal flow processes,” in *Geomorphological Techniques (Online Edition)*, British Society for Geomorphology, 2013.

[68] D. Lane, J. Bell and E. Dura, “Automatic 3D Reconstruction of Mine Geometries Using

Multiple Sidescan Sonar Images," La Spezia, 2001.

[69] H. Moravec and A. Elfes, "High resolution maps from wide angle sonar," *Robotics and Automation. Proceedings. 1985 IEEE International Conference on ,* vol. 2, pp. 116 - 121, 1985.

[70] A. Fenster, D. Downey and H. N. Cardinal, "Three-dimensional ultrasound imaging," *Physics in Medicine And Biology,* vol. 46, p. R67–R99, 2001.

[71] P. Kuchment and L. Kunyansky, "A Survey in Mathematics for Industry: Mathematics of thermoacoustic tomography," *Euro. Jnl of Applied Mathematics,* vol. 19, pp. 191-224, 2008.

[72] A. C. Kak and M. Slaney, Principles of Computerized Tomographic Imaging, IEEE Engineering in Medicine and Biology Society, 1988.

[73] Siemens Medical, "Computed Tomography," [Online]. Available: http://www.medical.siemens.com/siemens/zh_CN/gg_ct_FBAs/files/brochures/CT_History_and_Technology.pdf. [Accessed 18 Feburary 2014].

[74] I. Ihrke, K. Kutulakos, H. Lensch, M. Magnor and W. Heidrich, "Transparent and Specular Object Reconstruction," *Computer Graphics Forum,* vol. 29, no. 8, p. 2400–2426, 2010.

[75] S. Yamazaki, A. Nukada and M. Mochimaru, "Hamming Color Code for Dense and Robust One-shot 3D Scanning," in *In Proc. British Machine Vision Conference*, Dundee, 2011.

[76] W. Boehler, M. B. Vicent and A. Marbs, "Investigating Laser Scanner Accuracy," in *Proc. CIPA XIXth Int. Symposium*, Antalya, Turkey, 2003.

[77] FARO Technologies Inc., "Understanding Laser Tracker Targets," FARO, 2012.

[78] J. Levine, "Laser Distance Measuring Techniques," *Ann. Rev. Earth Planet Sci.,* vol. 5, pp. 357-69, 1977.

[79] FARO Technologies Inc., "Laser Trackers – IFM vs ADM Technology," 2009. [Online]. Available: http://farotechnologies.blogspot.co.uk/2009/09/laser-trackers-ifm-vs-adm-technology.html. [Accessed 10 Feburary 2014].

[80] Hexagon Metrology, "Leica absolute interferometer: A New Approach to Laser Tracker Absolute Distance Meters," December 2012. [Online]. Available: http://metrology.leica-geosystems.com/downloads123/m1/metrology/general/white-tech-paper/Leica%20Absolute%20Interferometer_white%20paper_en.pdf. [Accessed 10 Feburary 2014].

[81] A. Golubev, "Absolute Laser Interferometric Distance Measurement," *Survey Review,* vol. 32, no. 248, pp. 109-117, 1993.

[82] Z. Zhang, “Camera Calibration,” in *Emerging Topics in Computer Vision*, Prentice Hall Professional Technical Reference, 2004, pp. 4-43.

[83] G. Q. Wei and S. D. Ma, “A Complete Two-plane Camera Calibration Method and Experimental Comparisons,” in *Computer Vision, 1993. Proceedings., Fourth International Conference on*, Berlin, 1993.

[84] J. Salvi, X. Armangue and J. Batlle, “A comparative review of camera calibrating methods with accuracy evaluation,” *Pattern Recognition,* vol. 35, p. 617–1635, 2002.

[85] C. Ricolfe-Viala and A.-J. Sanchez-Salmeron, “Lens distortion models evaluation,” *Applied Optics,* vol. 49, no. 30, pp. 5914-28, 2010.

[86] J. Weng, P. Cohen and M. Herniou, “Camera calibration with distortion models and accuracy evaluation,” *IEEE Transactions on Pattern Analysis and Machine Intelligence,* vol. 14, no. 10, pp. 965-980, 1992.

[87] D. Brown, “Close-Range Camera Calibration,” *Photogrammetric Engineering,* vol. 37, no. 8, pp. 855-866, 1971.

[88] A. W. Fitzgibbon, “Simultaneous linear estimation of multiple view geometry and lens distortion,” in *in Computer Vision and Pattern Recognition, 2001. CVPR 2001. Proceedings of the 2001 IEEE Computer Society Conference on*, 2001.

[89] T. Clarke and X. Wang, “Extracting high precision information from CCD images,” in *In IMECHE conference transactions*, 1998.

[90] E. L. Hall, J. B. K. Tio, C. A. McPherson and F. A. Sadjadi, “Measuring curved surfaces for robot vision,” *Computer,* vol. 15, no. 12, pp. 42-54, 1982.

[91] R. Y. Tsai, “A versatile camera calibration technique for high-accuracy 3D machine vision metrology using off-the-shelf TV cameras and lenses,” *Robotics and Automation, IEEE Journal of ,* vol. 3, no. 4, pp. 323-344, 1987.

[92] R. K. Lenz and R. Y. Tsai, “Techniques for Calibration of the Scale Factor and Image Center for High Accuracy 3-D Machine Vision Metrology,” in *Robotics and Automation. Proceedings. 1987 IEEE International Conference on* , Raleigh, NC, 1987.

[93] J. Mitchelson and A. Hilton, “Wand-based Multiple Camera Studio Calibration,” CVSSP, University of Surrey, Guildford, UK, 2003.

[94] B. Caprile and V. Torre, “Using vanishing points for camera calibration,” *International Journal of Computer Vision,* vol. 4, no. 2, pp. 127-139, 1990.

[95] L. Quang-Tuan and O. Faugeras, “The fundamental matrix: theory, algorithms, and stability analysis,” *The International Journal of Computer Vision,* vol. 17, no. 1, pp. 43-76, 1995.

[96] H. C. Longuet-Higgins, “A Computer Algorithm for Reconstructing a Scene from Two Projections,” *Nature,* vol. 293, no. 5828, pp. 133-135, 1981.

[97] X. Armangue and J. Salvi, “Overall View Regarding Fundamental Matrix Estimation,” *Image and Vision Computing,* vol. 21, no. 2, pp. 205-220, 2003.

[98] R. I. Hartley and A. Zisserman, “Structure Computation,” in *Multiple View Geometry in Computer Vision*, Cambridge University Press, 2004, pp. 310-323.

[99] S. O. Nneji, S. Y. Zhang, S. Kabra, R. J. Moat and J. A. James, “Modelling and control of neutron and synchrotron beamline positioning systems,” *Nuclear Instruments and Methods in Physics Research Section A,* vol. 813, pp. 123-131, 2016.

[100] FARO Technologies Inc., “Laser Tracker Best Practices,” 03 November 2016. [Online]. Available: ftp://ftp.faro.com/FastFaxes/06REF177%20-%20Tracker%20FastFaxes/06REF177-148%20-%20Laser%20Tracker%20Best%20Practices.DOC. [Accessed 06 02 2017].

[101] C. Moreton-Smith, S. Johnston and F. Akeroyd, “Open-GENIE, a generic, multi-platform program for the analysis of neutron scattering data,” *Journal of Neutron Research,* vol. 4, no. 1-4, pp. 41-47, 1996.

[102] F. Pukelsheim, “The Three Sigma Rule,” *American Statistician,* vol. 48, pp. 88-91, 1994.

[103] S. S. Shapiro and M. B. Wilk, “An analysis of variance test for normality (complete samples),” *Biometrika ,* vol. 52, no. 3-4, p. 591–611, 1965.

[104] M. B. Wilk and R. Gnanadesikan, “Probability Plotting Methods for the Analysis of Data,” *Biometrika,* vol. 55, p. 1–17, 1968.

[105] Exelis VIS, “IDL Software - Data Visualization Software,” [Online]. Available: http://www.exelisvis.com/ProductsServices/IDL.aspx. [Accessed 13 August 2015].

[106] L. K. Barker, “Vector-algebra approach to extract Denavit-Hartenberg parameters of assembled robot arms,” NASA, Virginia, United States, 1983.

[107] C. Rajeevlochana, S. K. Saha and S. Kumar, “Automatic Extraction of DH Parameters of Serial Manipulators using Line Geometry,” in *The 2nd Joint International Conference on Multibody System Dynamics*, Stuttgart, Germany, 2012.

[108] S. Melax , “The Shortest Arc Quaternion,” in *Game Programming Gems*, Charles River Media, 2000.

[109] ANSI/RIA R15.05-1-1990 (R1999) , “Evaluation of Point-to-Point and Static Performance Characteristics of Industrial Robots and Robot Systems,” ANSI, 1999.

[110] F. S. Grastin, “Practical parameterization of rotations using the exponential map,” *Journal of*

Graphics Tools, vol. 3, no. 3, pp. 29-48, 1998.

[111] K. Arun, T. Huang and S. Blostein, "Least-Squares Fitting of Two 3-D Point Sets," *Pattern Analysis and Machine Intelligence, IEEE Transactions on,* vol. 9, no. 5, pp. 698-700, 1987.

[112] M. Shah, R. D. Eastmam and T. Hong, "An overview of robot-sensor calibration methods for evaluation of perception systems," in *Proceedings of the Workshop on Performance Metrics for Intelligent Systems*, New York, 2012.

[113] F. Ernst, L. Richter, L. Matthäus, V. Martens, R. Bruder, A. Schlaefer and A. Schweikard, "Non-orthogonal tool/flange and robot/world calibration," *Int J Med Robotics Comput Assist Surg,* vol. 8, no. 4, pp. 407-420, 2012.

[114] T. Clarke, "An analysis of the properties of targets used in digital close range photogrammetric measurement," in *Proc. SPIE 2350, Videometrics III*, Boston, 1994.

[115] T. Luhmann, "Eccentricity in images of circular and spherical targets and its impact to 3D object reconstruction," in *ISPRS Technical Commission V Symposium*, Riva del Garda, Italy, 2014.

[116] M. R. Shortis, T. A. Clarke and T. Short, "A comparison of some techniques for the subpixel location of discrete target images," in *Videometrics III*, Boston, 1994.

[117] songyuncen, "Sub-Pixel Edge Detection Using OpenCV," 25 December 2015. [Online]. Available: https://github.com/songyuncen/EdgesSubPix. [Accessed 12 February 2017].

[118] C. Steger, "An Unbiased Detector of Curvilinear Structures," Technische Universitat Munchen, Munchen, 1996.

[119] "OpenCV Library," [Online]. Available: http://opencv.org/.

[120] J. Chen, T. A. Clarke and S. Robson, "An alternative to the epipolar method for automatic target matching in multiple images for 3-D measurement.," in *Optical 3-D measurements techniques II*, Wichmann, Karlsruhe, 1993.

[121] H. Kuhn, "The Hungarian Method for the assignment problem," *Naval Research Logistics,* vol. 2, p. 83–97, 1955.

[122] K. Kanatani, Y. Sugaya and H. Niitsuma, "Triangulation from Two Views Revisited: Hartley-Sturm vs. Optimal Correction," in *proceedings for British Machine Vision Conference*, leeds, 2008.

[123] J. Y. Bouguet, "MATLAB calibration tool," [Online]. Available: http://www.vision.caltech.edu/bouguetj/calib_doc/.

[124] O. D. Faugeras, Three-Dimensional Computer Vision, The MIT Press: Cambridge, MA, 1993.

[125] S. Buss and K. and Jin-Su, “Selectively damped least squares for inverse kinematics,” *Journal of graphics, gpu, and game tools ,* vol. 10, no. 3, pp. 37-49, 2005.

[126] F. Malamud, S. Northover, J. James, P. Northover and J. Kelleher, “Texture analysis of Napoleonic War Era copper bolts,” *Applied Physics A: Materials Science & Processing,* vol. 122, no. 276, pp. 1-12, 2016.

[127] F. Malamud, J. R. Santisteban, M. A. V. Alvarez, R. Bolmaro, J. Kelleher, S. Kabra and W. Kockelmann, “Texture analysis with a time-of-flight neutron strain scanner,” *Journal of Applied Crystallography,* vol. 47, no. 4, pp. 1337-1354, 2014.

[128] H. E. Coules, L. D. Cozzolino, P. Colegrove, S. Ganguly, S. W. Wen and T. Pirling, “Neutron Diffraction Analysis of Complete Residual Stress Tensors in Conventional and Rolled Gas Metal Arc Welds,” *Experimental Mechanics,* vol. 53, pp. 195-204, 2013.

[129] F. Malamud, S. Northover, J. James, P. Northover, S. Nneji and J. Kelleher, “Spatially resolved texture analysis of Napoleonic War era copper bolts,” *Journal of Applied Crystallography,* vol. 50, no. 5, pp. 1359-1375, 2017.

Appendix A: Positioning Table

The knowledge of the joint limits is used in selecting configurations for the repeatability tests. The limits were found by manually jogging the positioner and recording the sensor positions at which the positioner stopped. The ENGIN-X positioning table which is calibrated as part of the thesis has the following joint limits.

Joint	Lower Limits	Upper Limits	Travel
X (mm)	-239.691	239.690	479.381
Y (mm)	-250.316	250.3155	500.631
Z (mm)	-295.950	295.950	591.900
Ω (deg)	-185.864	185.8635	371.727

Errors between the commanded and the measured angles/distances

The X, Y stages were commanded to move at intervals of 40mm from -200 to 200, the Z stage was commanded to move at intervals of 50mm from -250 to 250, and the W stage was commanded to move from -180 to 180 at intervals of 36°. The Euclidean distance between the measured points (for each stage) were computed and then subtracted from the commanded distance to compute the errors. Using the radius of rotation and the Euclidean distance of the W stage, the angle of rotation is computed; the difference between the computed angle and commanded angle is then representative of the error for the W stage. From these measurements, we observed the following:

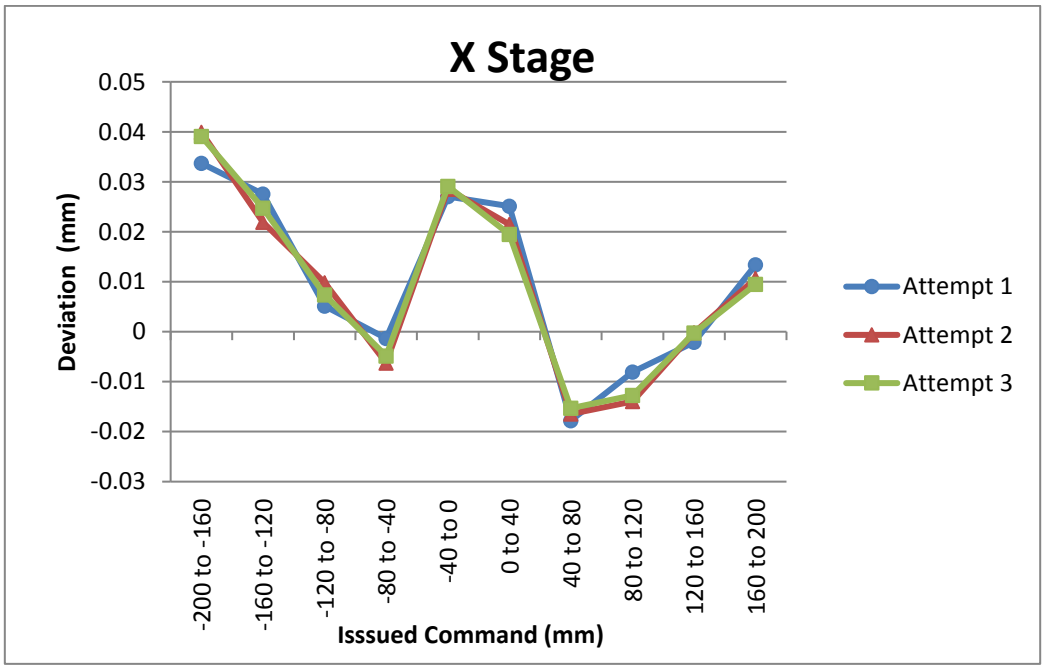

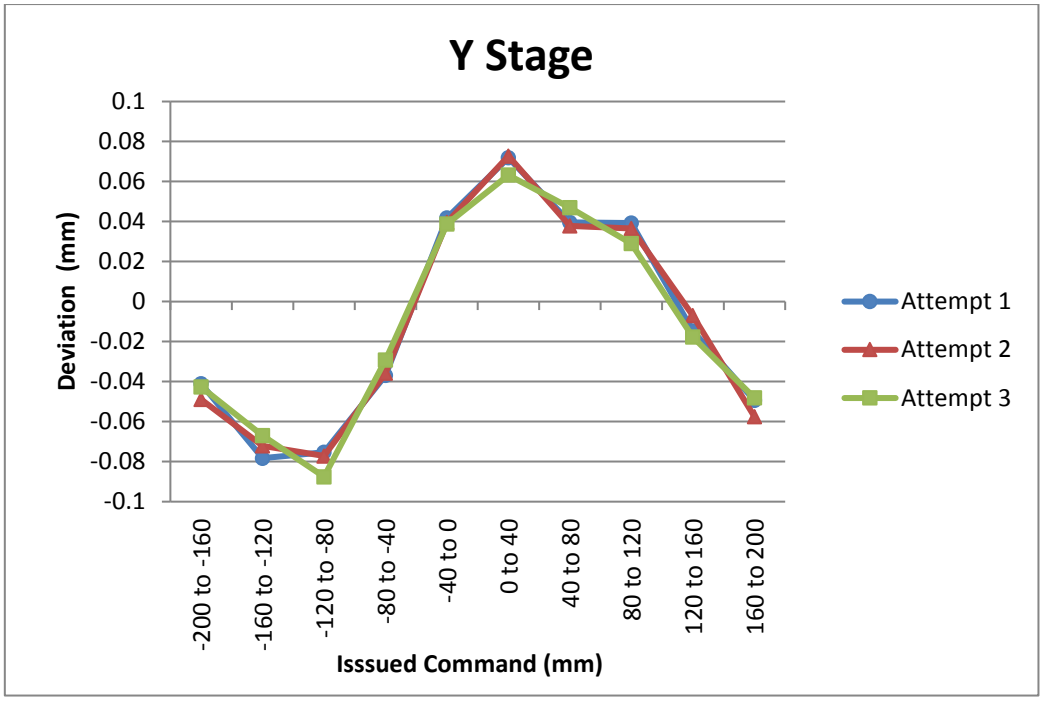
Y Stage
0.1
0.08
0.06
0.04
0.02
0
-0.02
-0.04
-0.06
-0.08
-0.1
Deviation (mm)
-200 to -160
-160 to -120
-120 to -80
-80 to -40
-40 to 0
0 to 40
40 to 80
80 to 120
120 to 160
160 to 200
Isssued Command (mm)
Attempt 1
Attempt 2
Attempt 3

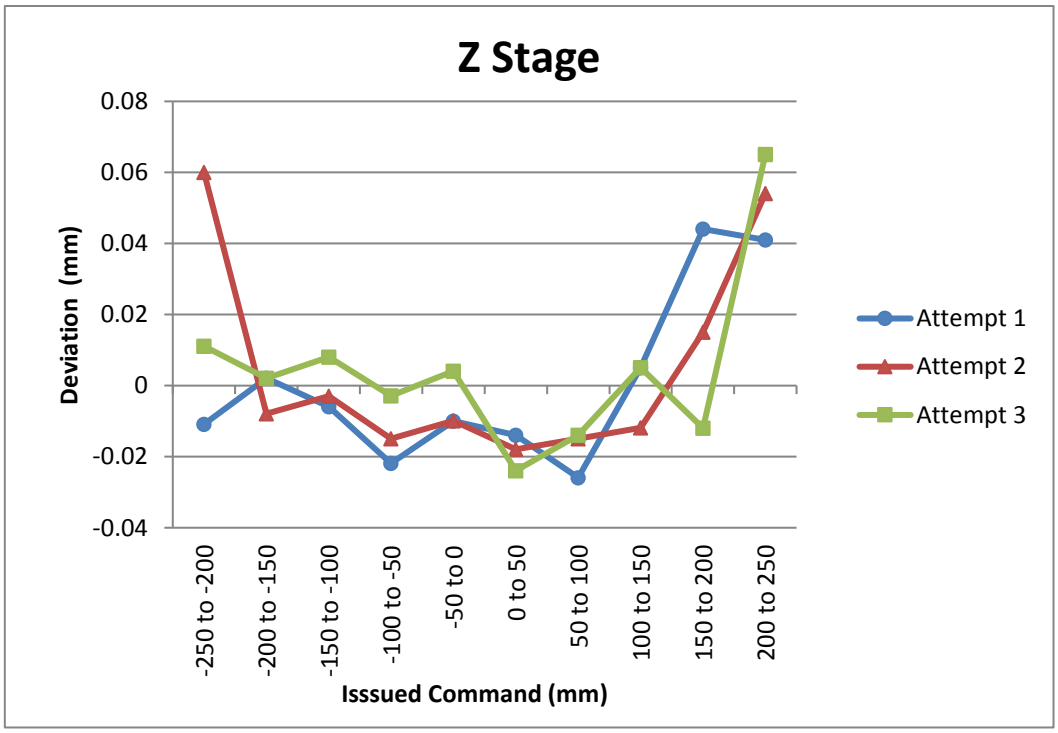
Z Stage
0.08
0.06
0.04
0.02
0
-0.02
-0.04
Deviation (mm)
-250 to -200
-200 to -150
-150 to -100
-100 to -50
-50 to 0
0 to 50
50 to 100
100 to 150
150 to 200
200 to 250
Isssued Command (mm)
Attempt 1
Attempt 2
Attempt 3

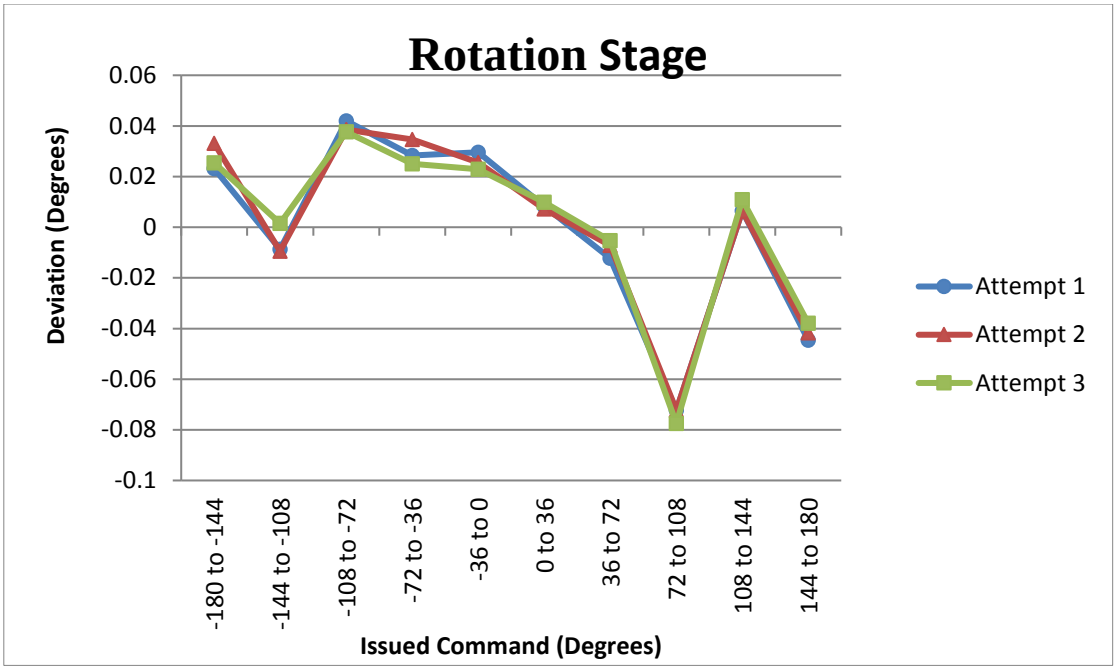
Rotation Stage
Deviation (Degrees)
0.06
0.04
0.02
0
-0.02
-0.04
-0.06
-0.08
-0.1
-180 to -144
-144 to -108
-108 to -72
-72 to -36
-36 to 0
0 to 36
36 to 72
72 to 108
108 to 144
144 to 180
Issued Command (Degrees)
Attempt 1
Attempt 2
Attempt 3

Appendix B: Camera Specification

The current design of the camera system designed in this thesis used the Basler Ace aca1920-25gm machine vision camera shown in the Figure below

The main specifications of the camera are presented in the Table below

Resolution (H x V)	1920px x 1080px
Pixel Size (H x V)	2.2 µm x 2.2 µm
Sensor Size (H x V)	4.22 mm x 2.38 mm
Efficiency (typical)	57,21 % (at 545 nm)
Saturation Capacity (typical)	6,7 ke
Dark Noise (typical)	6,4 e-
Sensor Vendor	Aptina
Sensor Name	MT9P031
Shutter	rolling shutter
Sensor Type	CMOS
Frame Rate	25 fps
Mon/Colour	Monochrome
Interface	GigE

The quantum efficiency of the camera is presented in the Figure below

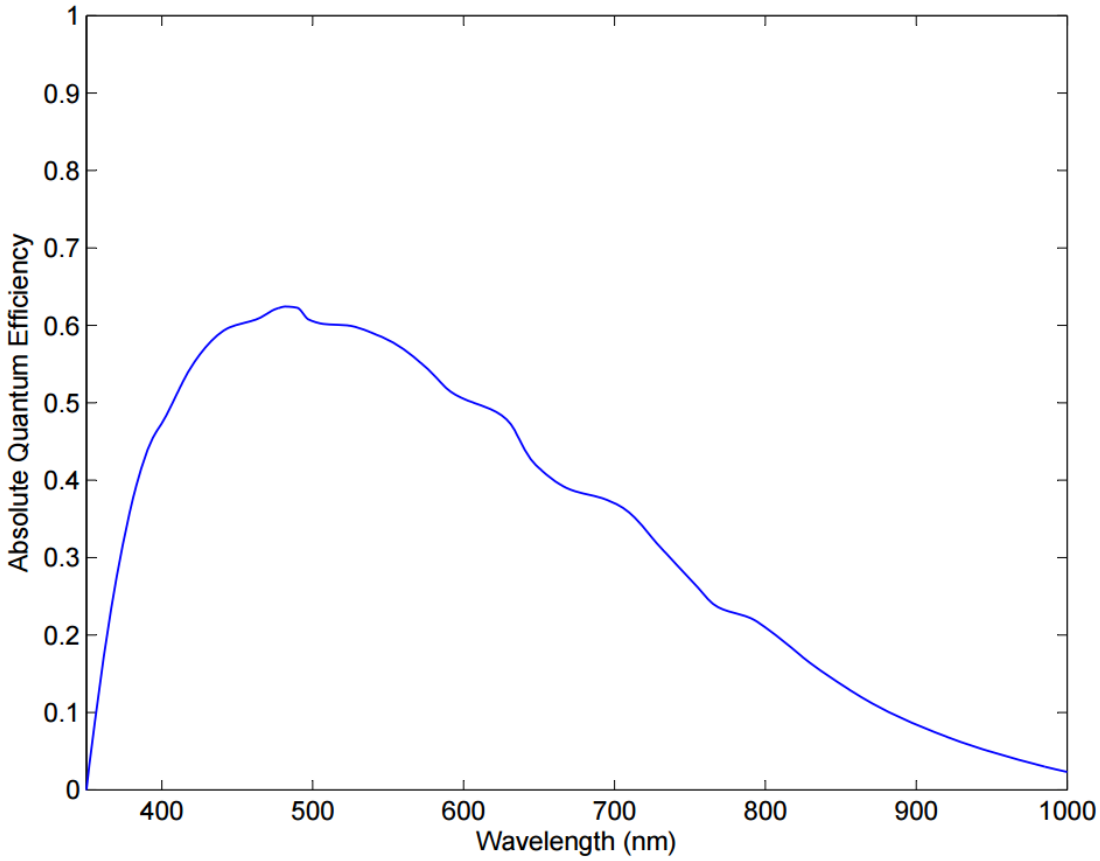

Appendix C: Tool Matrix Calculation

Recall, the forward kinematics gives the transformation from the base coordinate frame of the robot to the end effector ${}^{0}H_{n}$.

$$ {}^{0}H_{n} = f(x) $$

The tool transformation ${}^{n}H_{t}$ is a matrix that relates the end effector frame ${}^{0}H_{n}$ to the tool frame ${}^{0}H_{t}$ which in our case is in the sample. This is illustrated in the figure below:

$$ {}^{0}H_{t} = {}^{0}H_{n}\,{}^{n}H_{t} $$

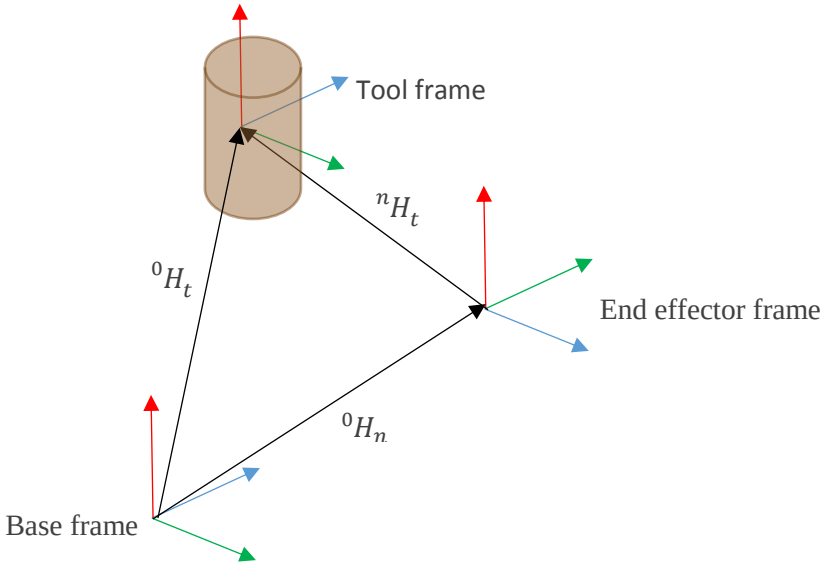

Given a set of fiducial points $\boldsymbol{P}$, measured in the instrument or base coordinate frame with the manipulator in its zero configuration. $\boldsymbol{P}$ is a $3 \times n$ matrix with each column containing a single point and n is the number of fiducial points. When the base of the robot is known, the tool can be calculated without any non-linear minimization.

1. Calculate the centre of mass (centroid) of the fiducial points ($\boldsymbol{P}$) by taking the sum of each row in $\boldsymbol{P}$ and dividing by the number of points n.
2. Since the sample is always measured in the instrument or base coordinate, the tool frame ${}^{0}H_{t}$ is a trivial matrix, the orientation part is an identity matrix ($\boldsymbol{I}$) and the translation part is the calculated centroid.

$$ {}^{0}H_{t} = \begin{bmatrix} \boldsymbol{I_{3\times3}} & Centroid \\ \boldsymbol{0_{1\times3}} & \boldsymbol{1} \end{bmatrix} $$

3. If ${}^{0}H_{n}$ is the homogeneous matrix from the forward kinematic model when all joint variables set to zero. The tool matrix is calculated as

$$ {}^{n}H_{t} = ({}^{0}H_{n})^{-1}\,{}^{0}H_{t} = {}^{n}H_{0}\,{}^{0}H_{t} $$